Title
Laser Assisted Nanomanufacturing with Solution Processed Nanoparticles for Low-cost Electronics and Photovoltaics

Author
Pan, Heng

Publication Date
2009

Peer reviewed|Thesis/dissertation

Laser Assisted Nanomanufacturing with Solution Processed Nanoparticles for Low-cost Electronics and Photovoltaics

by

Heng Pan

A dissertation submitted in partial satisfaction of the

requirements for the degree of

Doctor of Philosophy

in

Engineering-Mechanical Engineering

in the

GRADUATE DIVISION

of the

UNIVERSITY OF CALIFORNIA, BERKELEY

Committee in charge:

Professor Costas P. Grigoropoulos, Chair
Professor Xiang Zhang
Professor Tsu-Jae King Liu

Fall 2009

Laser Assisted Nanomanufacturing with Solution Processed Nanoparticles for Low-cost Electronics and Photovoltaics

By

Heng Pan

Abstract

Laser Assisted Nanomanufacturing with Solution Processed Nanoparticles for Low-cost Electronics and Photovoltaics

by

Heng Pan

Doctor of Philosophy in Engineering-Mechanical Engineering

University of California, Berkeley

Professor Costas P. Grigoropoulos, Chair

Nanomanufacturing is a term used to describe either the production of nanoscale materials, or to describe the manufacturing of parts 'bottom up' from nanoscale material or 'top down' in smallest steps for high precision. In recent years, nanomanufacturing is facing a new and broadened definition the essential themes lie on low cost, scalability, reliability and sustainability, besides the conventional requirements. The emphasis on this technology is towards realizing the low cost and large area manufacturing with control and benefits from nanoscale structures and nano enabled properties. The newly defined nanomanufacturing is expected to find extensive new applications in the large area electronics and renewable energy industries.

Nanomanufacturing based on solution processed nanoparticles is a promising approach towards this goal and is currently under intense research. This process significantly simplifies the manufacturing process and enables potential applications that are low temperature and extremely low cost. The solution deposition eliminates the need of multiple steps and vacuum deposition. It is capable of being integrated into the simple process, i.e. roll-to-roll manufacturing, to increase yield and process area. The suppressed melting temperature of nanoparticles also eliminates the need of high temperature processing. In solution processing, in general, nanoparticles prepared chemically with controlled stability and compositions are deposited in solution phase (e.g. printing) followed by annealing and/or nanopatterning steps for achieving the required spatial resolution and reasonable electrical and optical properties.

Laser processing, including annealing/sintering and ablation, of solution deposited nanoparticles is a new and interesting process that has barely been explored. Not only this process can take advantage of laser processing for low cost, low temperature device fabrication, but also a large amount of physics can be explored including laser-nanomaterial interaction, nanoscale heat/mass transport, defects / grain boundaries evolution, semiconductor device physics and photonics, etc. The present study examined various components in the low cost nanomanufacturing process, including laser annealing of semiconductor and metallic nanoparticles, optical characterization of sintering process and scalable nanopatterning techniques. The emphasis is on both demonstration of novel processes and working devices as

well as fundamental experimental and numerical studies of transport phenomena involved in laser induced solid state and melt-mediated nanoparticle coalescence.

Firstly, to provide insight into the transport phenomena involved in laser induced non-melt and melt-mediated nanoparticle coalescence, experimental and numerical studies were performed. The Molecular Dynamics simulation was adopted to study the solid-state nanoparticle sintering by laser heating. The comparison between MD and macroscopic model reveals the unique mechanisms in sub-10nm nanoparticles sintering suggesting enhanced neck growth rate can be expected for nanoparticle with size below 10nm. The melt-mediated nanoparticle coalescence induced by *ns* laser is probed in-situ by a pump-and-probe technique. The probing results reveal several important characteristic times during laser annealing that will determine the morphology and crystalline structures of the laser processed film: characteristic coalescence time, cooling and resolidification times. The coalescence time compares favorably with MD simulation.

Secondly, the laser annealing of metal oxide nanoparticles for electronics and photovoltaics are demonstrated. Solution deposited ZnO nanoparticles can be transformed into active channel layer of thin film transistors (TFTs) by Excimer laser annealing (ELA). The device shows mobility ~0.1 cm^2/V-s and current on/off ratios of more than 10^4. The properties of the laser annealed films were characterized by scanning electron microscopy, high-resolution TEM, DC conductance, and photoluminescence measurements. Furthermore, ELA is combined with spray deposition of TiO_2 nanoparticle to fabricate dye sensitized solar cells (DSSCs) on glass and plastic substrates. All-laser-annealed TiO_2 photoelectrodes achieve efficiency at ~3.8% with Ruthenium dyes.

Optical characterization of optical properties and film thickness by ellipsometry is also demonstrated for silver nanoparticle film sintering. The ellipsometric measurement is found to be robust in capturing the percolation transition, dielectric constant and film thickness evolutions. The non-contact optical measurement is also found to correlate well with DC measurement.

Finally, large-area optical near-field nanoprocessing, i.e. nanosintering and nanoablation, of solution deposited nanoparticle is demonstrated. The feature size down to ~150nm is obtained and annealing in furnace further reduces the feature size down to ~50nm. Nanoscale organic transistors are fabricated by nanosintered electrodes and solution deposited air-stable semiconductor polymer. Molecular Dynamics simulation is also employed to calculate the effective thermal conductivity of the nanoparticle film to facilitate thermal modeling of the nanoscale laser processing.

To my family

ACKNOWLEDGEMENTS

I would like to, first of all, express my most sincere gratitude to my research advisor, Professor Costas P. Grigoropoulos, for his guidance, encouraging advice, inspiring discussions, great patience and financial support. I wouldn't have reached this point without his support. I would also like to extend my thanks to Professor Seunghwan Ko at KAIST university, Seoul, Korea for being both my teacher and a coworker – for all the evaluable discussions and helps.

It has been my great pleasure to work together with former members as well as my fellow colleagues in Laser Thermal Lab. I would like to thank Dr. David J. Hwang, Dr. Anant Chimalgi, Dr. Li Xu, Dr. Hyung-gyu Park, Dr. Ming-Tsang Lee, Dr. Nipun Misra, Dr. Moosung Kim, Dr. Nico Hotz, Dr. Matthew Rogers, Sang-Gil Ryu, Hojeong Jeon, Jungbin In, Travis Owenz, Daeho Lee, Kyunghoon Kim and Sanghoon.Ahn, Eunpa Kim, Yann Chalopin and Kullmann Carmen. I would also like to extend my gratitude to Professor Oscar Dubon, Professor Eugene Haller, Nate Miller of the Department of MSE, and Professor J.M.J. Fréchet, Dr. Biwu Ma, and Tabitha A. Clem of School of Chemistry, University of California, Berkeley, and Professor Dentcho Genov at LSU for valuable discussions and supporting materials.

Finally, I am very grateful for my family for their love and understanding. I would like to thank my wife Weiya Fang for her understanding, encouragement and great patience, my parents for being always supportive and my daughter Bohan Pan. They always give me unconditional support and encouragement. I would like to dedicate my dissertation to them.

TABLE OF CONTENTS

LIST OF FIGURES

LIST OF TABLES

NOMENCLATURE

a: particle radius
A_V : the surface area of the neck
A : the amplitude
A_{cross} : the cross section area of the particle
b: the thickness of the region of enhanced diffusion at the grain boundary
c : the distance of the center of the particle to the symmetry plane
C : specific heat
C_0 : the initial concentration
C_{ox} : the capacitance
C : the thiol concentration
D_B : the diffusion coefficients for grain boundary
D_S : the diffusion coefficient for surface
D: particle diameter
E: photon energy
E_N : oscillator resonance energy
F_{mean}: mean force
F_{inc} : the incident laser fluence
F_A: ablation threshold
f : the volume fraction of the particle
ΔG : the Gibbs free energy of activation for the desorption reaction
h : the Planck's constant
I : laser intensity
j : the local current
J: heat flux
J_{GBD} : material flux by grain boundary diffusion
J_{SD}: material flux by surface diffusion
J_{sc} : short circuit current
k : the Boltzmann constant
k_B : the Boltzmann constant
L: channel length
N_{peak} : the near-field enhancement at the beam spot center
p_L : pressure inside the particle
P_N : the normal component of the pressure to the spherical surface
p_G : the gas pressure outside the particle
P_c : percolation threshold
r_{ij} : the distance between two atoms
R : the universal gas constant
R : nanoparticle radius
T : the temperature
t : time

$U(n_i)$: the energy associated with the coordination n_i of the atom i

V : potential energy of a MD simulation system

V_g: gate voltage

V_T : volume of the material that has moved into the neck

V_B : volume of overlap of the original sphere

V_S : volume of material arriving from the sphere surface

V_{oc}: open circuit voltage

V_P : particle volume

W: channel width

x : neck radius

Greek Letters

α : the surface tension

α : grain boundary groove angle

δ : the extent of the overlapping of the two spheres

ε : the well depth was chosen to be 0.1eV to simulate moderate adhesion interaction

$\varepsilon(E)$: the effective dielectric function

ε_∞ : real part of dielectric function at large photon energies

ε_{eff} : effective dielectric function

ε : dielectric function of the particle

ε_M : dielectric function of the matrix

ε_b : the contribution due to the interband transitions

κ : the absorption efficiency

κ : thermal conductivity

σ : 0.27nm was kept constant

η : the viscosity

τ : coalescence time

Γ : the dissipative broadening

ρ : the radius of the neck surface

ψ and Δ : ellipsometric parameters

$\phi(r_{ij})$: a standard two body potential

$\phi_{MF}(r)$: potential of mean force

ω_p : the plasma frequency

ω_τ : the relaxation rate

Ω : the molar volume

γ : the surface tension

CHAPTER 1

INTRODUCTION

1.1 Flexible, Large-area, Low-cost Electronics and Energy Harvesting Devices

Flexible electronics refers to the electric devices built on flexible substrates, for example plastic, fabric, paper and metal foil. Besides its flexibility, lightweight and durability, the most attractive advantage is its adaptability in ultra low-cost and large area manufacturing, e.g. roll-to-roll processing. The flexibility means that the electronics do not need to be confined to a hard substrate or housing but offer the ability to conform, bend or roll into any shape. Essentially, electronics can be printed directly on flexible substrates that are cheap and can be made into any size and any length while large size glass or silicon substrates. This direct addictive manufacturing alleviates the limitation on the high capital equipment investigation and processing area on the conventional clean room fabrication tools. Some of the most popular examples are a flexible display [Universal Display Corporation] and a wearable computer [MIT media lab] (Fig. 1.1).

The fabrication of flexible electronics will find its niche market in today's energy harvesting industry. Solar energy represents the ultimate in green and renewable power. With solar cells build on flexible substrates, one could imagine a backpack that charges electronic devices while walking to work or a briefcase that powers cell phones, or an umbrella enabling to stay productive off the grid – while enjoying a day at the beach [*Konarka Inc.*]. Furthermore, the reduction of the cost by printing high performance solar cells on flexible substrate would enable the strong and continual growth of the solar industry since the reduction of cost per power is the key for the success of solar energy industry.

1.2 Large Area and Low Cost Nanomanufacturing

Nanomanufacturing is a term used to describe either the production of nanoscale materials, or to describe the manufacturing of parts 'bottom up' from nanoscale material or 'top down' in smallest steps for high precision [http://en.wikipedia.org/wiki/nanomanufacturing]. Nanomanufacturing has been substantially developed along with the tremendous applications of nanotechnology in a number of areas, especially microelectronics, data storage and biological sensing. The focus of the nanomanufacturing is mostly on 1) acquiring control on the macroscopic properties with nanoscale building blocks and nanostructures, 2) on achieving high performance of each individual device with high device density by utilizing the nanoscale characteristics, 3) placing emphasis on both macroscopic and individual nanoscale performance. Towards the first goal, nanomanufacturing includes processes based upon various building blocks, e.g. nanotubes [http://en.wikipedia.org/wiki/Carbon_nanotube], nanowires/rods [Huynh *et al.* (2002), Law *et al.* (2005)], nanoparticles [Gratzel et al. (2000)], nanopillars [Fan *et al.* (2009)] as well as those by top-down approaches. Regarding the second objective, various nanopatterning processes are required and have emerged over the past few decades. Conventional lithography based processes, such as e-beam lithography, DUV lithography are subject to limitations, in that they are multi-step, involve high processing temperature, strong solvents and high cost of implementation. In order to alleviate these limitations, many alternative non-lithographic nanopatterning approaches to conventional processes have been introduced,

including both optical and non-optical methods. Optical nanopatterning would generally require near-field effect to overcome the theoretical diffraction limit [Chimmalgi *et al.* (2005), Hwang *et al.* (2006), Betzig *et al.* 1992]. Non-optical processes include nanoimprinting [Chou *et al.* (1996)], gravure printing [Kraus *et al.* (2007]], electrodynamic printing [Park *et al.* (2007)], dip-pen [Piner *et al.* (1999)], fluid assembly of nanowire [Li *et al.* (2008)] and self assembly with optical forces [Pauzauskie *et al.* (2006)], etc.

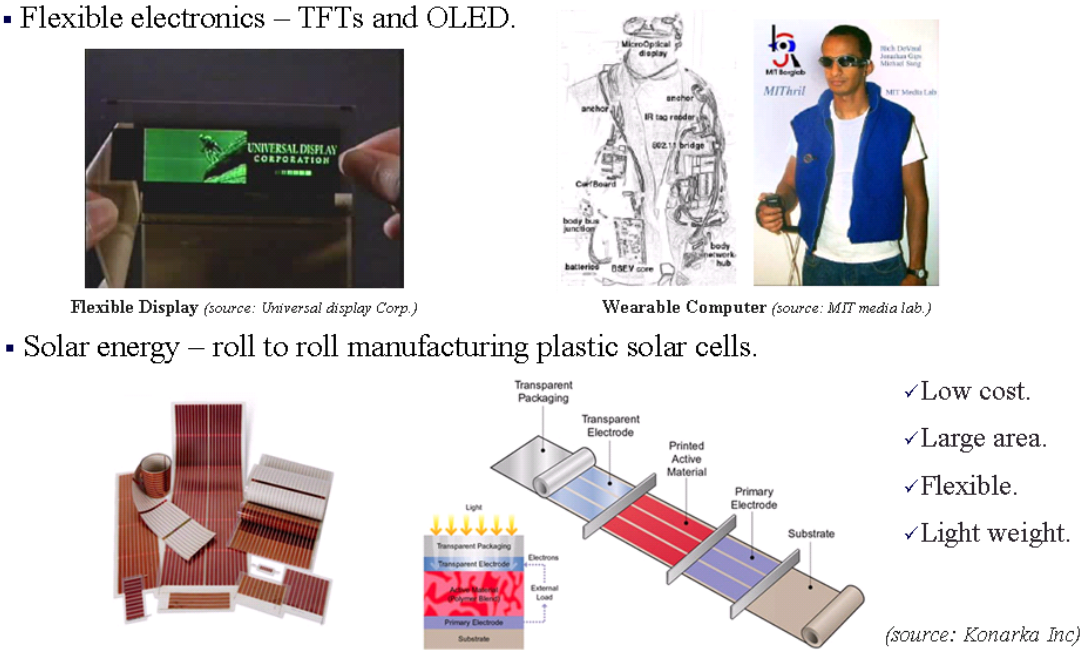

Fig. 1. 1 Flexible electronics and flexible solar cells.

In recent years, nanomanufacturing is facing a new, broadened definition and opportunity whose essential themes lie on low cost, scalability, reliability and sustainability, besides the conventional requirements. The emphasis on this technology is towards realizing the low cost and large area manufacturing with control and benefits from nanoscale structures and nano enabled properties. The newly defined nanomanufacturing is expected to find extensive new applications in the large area electronics and renewable energy industries, i.e. microelectronics such as sensors, smart cards, portable energy sources, window shades and integrated widow panels, smart shade structures, etc.

Nanomanufacturing based on solution processed nanoparticles is a promising approach towards this goal and is currently under intense research. This process significantly simplifies the manufacturing sequence and allows potential applications that are low temperature and potentially extremely low cost. The solution deposition eliminates the need of multiple steps and vacuum deposition. It is capable of being integrated into the simple process, i.e. roll-to-roll manufacturing, to increase yield and process area. The suppressed melting temperature of nanoparticles also eliminates the need of high temperature processing. In solution processing, in general, nanoparticles prepared chemically with controlled stability and composition are deposited in solution phase (e.g. printing) followed by nanopatterning and/or annealing steps for achieving superior spatial resolution and reasonable electrical and optical properties that are required to create functional devices. For example, *Nanosolar* developed a novel printable inks

consisting of CIGS (Cadmium Indium Gallium Selenide) nanoparticles. The CIGS nanoparticles are printed on stainless steel and annealed by rapid thermal annealing for large area solar cell fabrication. *Innovalight* synthesizes silicon nanoink and uses high precision inkjet manufacturing leading to a high efficiency, low cost and highly reliable silicon based solar modules.

The present study envisions that the new nanomanufacturing process would generally consist of several components as shown in Figure 1.2. A synthesis step is needed where various nanoparticles need to be synthesized and suspended in solution and form nanoinks. A deposition process, e.g. inkjet printing or screen printing, is then required to deposit nanoparicle ink on substrate. The deposition can directly generate patterns with the spatially resolution controlled by nozzle dimension or produce uniform nanoparicle films on large area. The latter deposition is often applied in solar cell panels or large area displays fabrication. After the deposition, a thermal annealing or laser annealing step is required to transform isolated nanoparticle into electrical conductive or optically smooth thin film. Online characterization to monitor the film properties is often necessary to guarantee desired film properties and thickness. An alternative step for nanopatterning the film is also suggested. The nanopatterning will generate nanostructures on a large area for enhancement of performance or device definition.

The present study examines each component involved in the nanoparticle based nanomanufacturing process (Fig.1.2), including laser annealing of nanoparticles, laser assisted nanopatterning as well as optical characterization techniques. The motivation and uniqueness of laser processing will be introduced in next section.

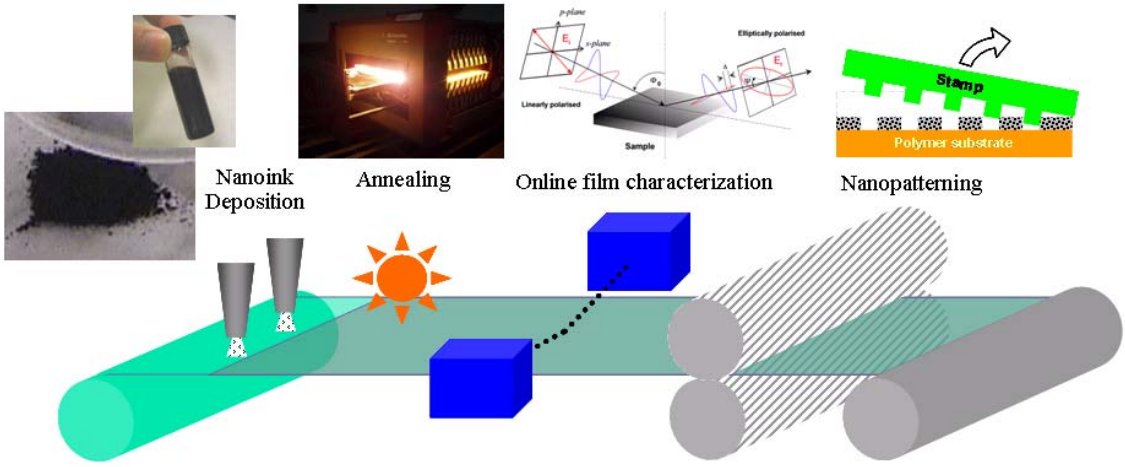

Fig. 1. 2 The schematic of large area and low cost nanomanufacturing.

1.3 Laser Processing Advantages

Laser processing of semiconductor has been developed for several decades. The advantages of using laser processing are summarized in Figure 1.3. Among various techniques, laser annealing of silicon for thin film transistors (TFTs) and photovoltaics deserves special attention. Both pulsed and continuous lasers have been applied to recrystallize amorphous silicon thin films for TFTs [Miyasaka *et al.* (1999)] and photovoltaics [Adikaari *et al.* (2007)]. Besides the advantages of achieving superior spatial resolution, laser processing represents a novel approach for low cost and large silicon device.

Despite the various applications in annealing and recrystallzation of amorphous materials, laser processing of semiconductor nanoparticles for electronics and photovoltaics has rarely been

explored. Converting isolated nanoparticle film into conductive film through non-melt or melt processes induced by laser irradiation entails an interesting study, not only taking advantage of all the uniqueness of laser processing of semiconductor for low temperature fabrication, but also significant physics can be explored including laser-nanomaterial interaction, nanoscale mass transport, nanoscale heat transport, semiconductor device physics, defect / grain boundaries evolution, etc. Our studies aim at shedding light on the above mentioned aspects: fabrication of working devices via laser annealing of nanoparticles will be demonstrated and fundamental studies of mass and heat transfer involved in laser induced solid state and melt-mediated nanoparticle coalescence will be performed.

Furthermore, laser assisted near-field nanopatterning is worth mentioning. As an optical nanopatterning method, laser nanopatterning is focused on reducing the cost and complexity of conventional processes. A number of laser nanopatterning methods have been developed [Chimmalgi *et al.* (2005), Hwang *et al.* (2006), Sun *et al.* (2006)], while most of them suffer from the inability of scaling up or limitation in applicable materials. We suggest a new scalable and large area nanopatterning method for application in solution processed nanoparticles.

To further illustrate potential applications of laser processing, an example of a typical solar cell is also shown in Figure 1.3. First, laser annealing/sintering and recrystallization of active semiconductor are clearly of value. Various semiconductor nanoparticles can be annealed to form networking structure with well controlled porosity and nano-crystallinity. Applying laser for transparent conductor oxide (TCO) layer annealing, e.g. ITO and ZnO, represents another potential application. Furthermore, replacing TCO with nanostructured metal grids is currently an active research area. The utilization of high-throughput laser near-field nanopatterning can find its potential for approaching this objective. Laser annealing is also known to reduce the contact resistance and alter the defect levels. Last but not least, laser scribing is another area deserving intensive study.

1.4 Scope of Dissertation

In chapter 2, Molecular Dynamics simulations were employed to investigate the mechanism and kinetics of solid-state sintering of two crystalline gold nanoparticles (4.4-10.0nm) induced by laser heating. The classical diffusion based neck growth model is modified to predict the time resolved neck growth during continuous heating with the diffusion coefficients and surface tension extracted from MD simulation. The diffusion model underestimates the neck growth rate for smaller particles (5.4nm) while satisfactory agreement is obtained for larger particles (10nm). The deviation is due to the ultra-fine size effect for particles below 10nm. Various possible mechanisms are identified and discussed.

In chapter 3, fundamental study of laser induced melt-mediated gold nanoparticle coalescence is performed. Gold nanoparticles supported on a quartz substrate are fabricated by e-beam lithography and subjected to nanosecond laser irradiation to induce coalescence. In combination with ex-situ scanning Electron Microscopy and optical extinction spectra, transmission is monitored in-situ to determine the characteristic coalescence time, the threshold fluence for the onset of coalescence and the produced particle morphology. Parallel Molecular Dynamics simulation is employed and shown to reasonably predict the coalescence time, explaining the experimental results.

In chapter 4, Excimer Laser Annealing (ELA) was employed to induce melting of solution-deposited ZnO nanoparticles and form electrically conductive porous films. The properties were characterized by scanning electron microscopy, high-resolution TEM, DC

conductance, and photoluminescence measurements. Thin-film field effect transistors have been

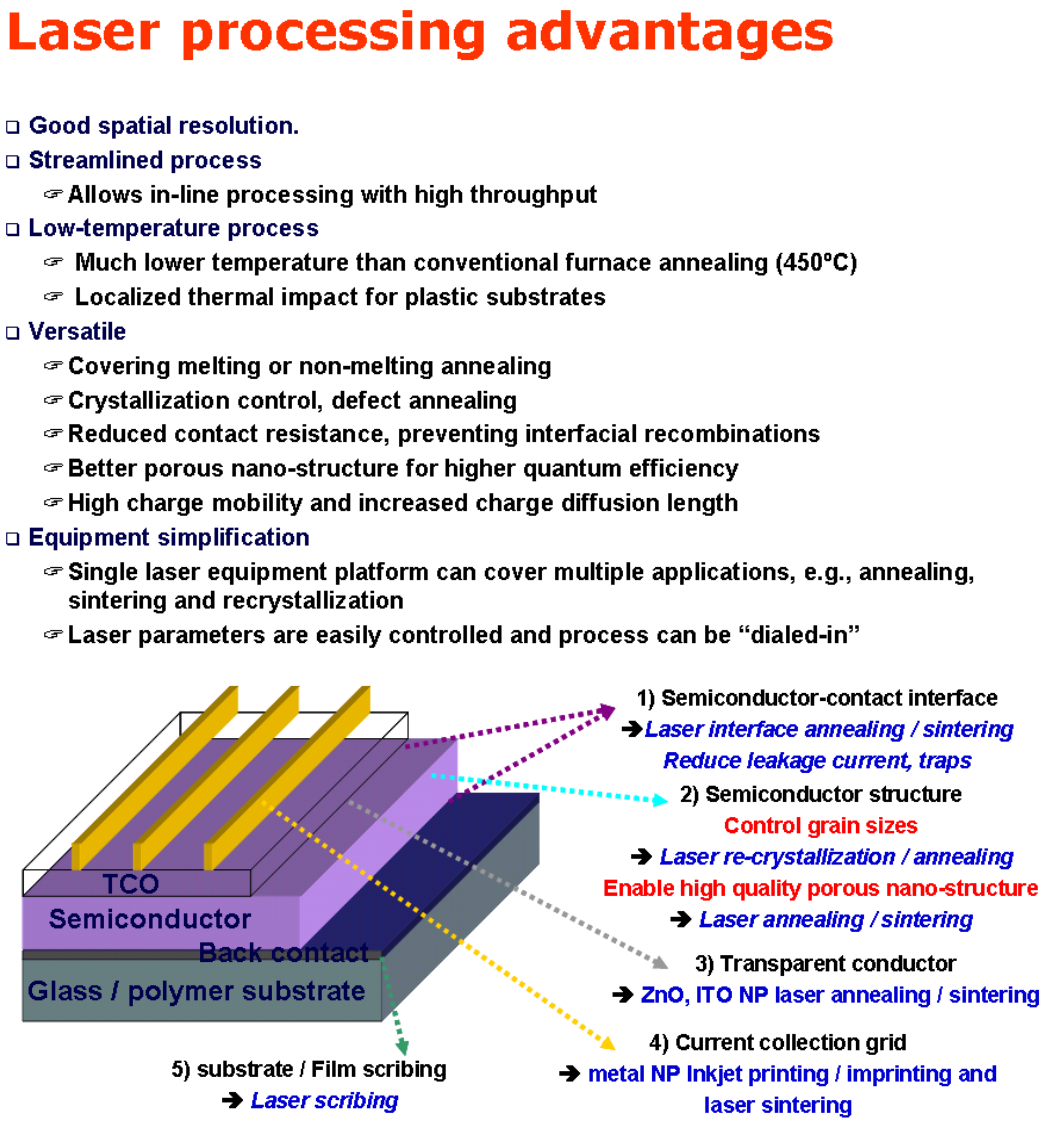

Fig. 1. 3 The advantages of laser processing and the example of applying laser processing in typical solar cells.

fabricated by ELA without the use of conventional vacuum or any high temperature thermal annealing processes.

In chapter 5, Dye-sensitized solar cells (DSSCs) on glass and plastics are fabricated by *in-tandem* spray deposition and laser annealing of TiO_2 nanoparticles. Laser annealed double-layered structure is demonstrated for both doctor-blade deposited and spray-deposited electrodes and performance enhancement can be observed.

In chapter 6, Spectroscopic ellipsometry (SE) in the spectral region of 0.75eV-3.5eV is employed to characterize the sintering process manifested by the evolution of film thickness, effective dielectric function and percolation transition. A two-oscillator model can be used to model the effective dielectric function through the dielectric-to-metallic transition. The oscillator energy shifts towards the lower end and correlates well with the increase of DC conductance as

demonstrated by both *in-situ* and *ex-situ* ellipsometric measurements. A simple model based upon 2D *R-L-C* impedance network was successfully adopted to explain experimental results quantitatively.

In chapter 7, the optical near-field nanoprocessing of nanoparticles for high-throughput nanomanufacturing is reported. The method unitizes fluidically assembled microspheres comprising near-field focusing lens array for laser assisted nano-sintering or nano-ablation of nanoparticles. Benefiting from low processing temperature and reduced thermal diffusion in the nanoparticle film, minimum feature size down to ~150nm can be realized. In addition, we observed that smaller features (50nm) can be obtained by furnace annealing laser-sintered nanodots at 400°C. Molecular dynamics simulation and thermal modeling are performed to predict nanoparticle film thermal conductivity and processing temperature. The electrical conductivity of sintered nanowires is studied. Using nanowire electrodes with submicron gap, we subsequently fabricate organic field effect transistors (FETs) with oxygen stable semiconducting polymer.

CHAPTER 2

FUNDAMENTAL STUDIES ON LASER INDUCED SOLID STATE SINTERING OF NANOPARTICLES

Molecular Dynamics simulations were employed to investigate the mechanism and kinetics of the solid-state sintering of two crystalline gold nanoparticles (4.4-10.0nm) induced by laser heating. At low temperature (300K), sintering can occur between two bare nanoparticles by elastic and plastic deformation driven by strong local potential gradients. This initial neck growth occurs very fast (<150ps), and is therefore essentially insensitive to laser irradiation. This work focuses on the subsequent longer time scale intermediate neck growth process induced by laser heating. The classical diffusion based neck growth model is modified to predict the time resolved neck growth during continuous heating with the diffusion coefficients and surface tension extracted from MD simulation. The diffusion model underestimates the neck growth rate for smaller particles (5.4nm) while satisfactory agreement is obtained for larger particles (10nm). The deviation is due to the ultra-fine size effect for particles below 10nm. Various possible mechanisms were identified and discussed.

2.1 Introduction to the Sintering Modeling

Recent interest in fabricating flexible electronics has spurred extensive research related to delivering and defining both active and passive materials in a cost effective and precise manner. The printing of nanoparticles followed by low temperature thermal treatment has shown substantial promise in ultra-low-cost electronic fabrication [Ko *et al.* (2007)]. Employing laser radiation to selectively sinter nanoparticles and define micron, even sub-micron features has demonstrated advantages in terms of meeting performance and cost requirements [Chung *et al.* (2004), Ko *et al.* (2007)]. Previous research efforts on laser patterning of nanoparticles in micro-fabrication as well as envisioned future research in nanoparticle based nano-fabrication have sparked great interest in understanding the associated fundamental phenomena, such as nanoscale phase change, sintering or coalescence transformation induced by laser irradiation, as needed for realizing low resistance ohmic nanocontacts [Kim *et al.* (2005)].

In this study, Molecular Dynamics is employed to study the fundamental physics involved in nanoparticle sintering by continuous laser heating. There are a variety of sintering or coalescence models, such as the conventional neck growth model, either based on diffusion [Kuczinski *et al.* (1949), Johnson *et al.* (1968), Nichols *et al.* (1965)] or viscous flow [Frenkel *et al.* (1945)] and the K-F type model [Koch *et al.* (1990), Friendlander *et al.* (1994)]. In the conventional model, the detailed necking profile is tracked and diffusion mechanisms need to be identified. In the K-F type model, which is widely used in the aerosol research community, a simple linear relation between excess surface area and neck growth rate is used [Friendlander *et al.* (1994)] instead of tracking the detailed necking profile. The K-F model can be applied to viscous flow or solid diffusion based process requiring no identification of the diffusion mechanisms is needed. Most of these models are applied to isothermal sintering process with a few exceptions [Lehtinen *et al.* (2002)] where temperature variation due to the heat exchange with the surrounding environment is considered.

Investigations have focused on the applicability of the macroscopic sintering model to the nano-scale phenomenon. New mechanisms emerge in nano-scale sintering, such as elastic/plastic deformation and dislocation [Zhu *et al.* (1996), Zeng *et al.* (1998)]. Existing facets could slow down the curvature driven diffusion [Combe *et al.* (2000)]. It is also argued that the linear relation for diffusion is no longer valid for nanoscale sintering since the thermodynamic driving force stemming from chemical potential gradients is very large for particles below 100nm [Pan *et al.* (2004)]. Moreover, in nanoscale sintering, inter-atomic attraction becomes very important, inducing accelerated necking growth. This 'force-driven' diffusion needs to be distinguished from standard 'random walk' ones and treated differently [Zeng *et al.* (1998)]. There have been efforts to model the nanoscale phenomenon by modifying the bulk physical properties to account for ultra-fine size effects: Xing [Xing *et al.* (1999)] improved the coalescence time prediction by using depressed melting temperature and Arcidiacono [Arcidiacono *et al.* (2004)] applied a similar approach to obtain reasonable predictions of the neck growth for ultra-fine nanoparticles. Clearly more work is needed to reach quantitative evaluation of the usefulness of the conventional neck growth mode that ignores all ultra-fine size effects. It should be noted the physical parameters needed for the analytical model need to be extracted directly from MD simulation, whereas the confined size effects on the physical properties can be fully taken into account without using modifications of bulk properties, therefore avoiding respective errors.

In summary, this work applied Molecular Dynamics simulations to study the sintering of gold nanoparticles by continuous heating. A conventional neck growth model was modified and adopted for continuous heating. The physical properties were extracted from simulation directly.

MD simulation was employed to cover a wide size range (4.4-10nm) and longer simulation time (~10ns), enabling the evaluation of the applicability of the conventional models over correspondingly wider size range.

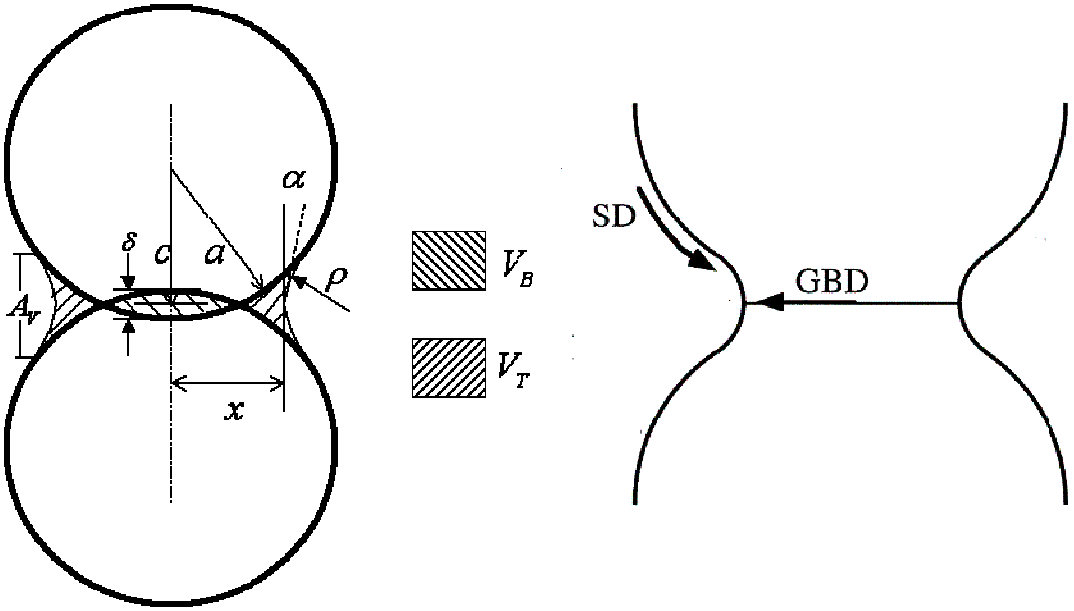

Fig. 2.1 Sintering geometry and atom movement pathways for different sintering mechanisms.

2.2 Modeling Methods

2.2.1 Molecular Dynamics Simulation

To track the sintering process, an atomistic simulation approach using classical MD was employed. In this study, the glue potential for gold developed by [Ercolessi *et al.* (1998)] was adopted since it was found to yield an accurate description of bulk, defect, and surface properties of gold. In the glue model, the potential energy of a system of *N* atoms consists of a sum of pair potentials and a many-body glue energy:

$$V = \frac{1}{2}\sum_{ij}\phi(r_{ij}) + \sum_{i}U(n_i) \tag{2-1}$$

where r_{ij} is the distance between two atoms, $\phi(r_{ij})$ is a standard two body potential, $U(n_i)$ is the energy associated with the coordination n_i of the atom *i*. The parameters are reconstructed empirically to reproduce the experimental values of gold over a wide range of thermodynamic conditions. The details of the model and related parameters are given in the reference [Ercolessi *et al.* (1998)].

A parallel MD simulation program has been developed that can currently handle up to 150,000 atoms for the study of relatively long time scale events (~10ns), such as sintering, at a reasonable computational time. Atom trajectories were determined by integrating the classical equations of motion using the velocity form of the Verlet algorithm with rescaling of atomic velocities to

achieve temperature control. Time steps of 3.0 fs were typically used and the atom neighbor list was updated every time step. Single gold nanoparticles of various sizes (2633, 5053 and 31077 atoms) were prepared at different temperature. The target temperature was obtained by rescaling every 200 time steps. The rescaling was applied for 10^4 time steps, after which, up to 10^5 time steps were allowed to achieve full equilibrium before property sampling was conducted.

To simulate the sintering process, two identical particles were first brought into contact at a center-to-center distance of 2R+0.5nm at ~300K. The initial neck growth was allowed to complete without laser irradiation. After the initial neck growth, the particle pairs were subjected to continuous laser heating. The heating rate is in the range of $0.89\times10^{11} K/s$ to $2.20\times10^{11} K/s$ simulating the heating by a continuous laser with laser intensity around $10^{10} W/m^2$. No heat loss to the environment was considered in the present study. To mimic the laser heating, the kinetic energy of the system was increased by a fixed amount at each step by rescaling the velocities, so the total energy increases linearly in time.

The structural change was monitored during sintering via calculating bond order parameters (BOP). Four bond order parameters were used together to identify the structure accurately. The values of these bond order parameters for fcc, hcp, amorphous structures and the detailed description of the BOP can be found in reference [Steinhardt *et al.* (1993)].

2.2.2 Analytical Neck Growth Model

The model is essentially the one presented by Johnson [Johnson *et al.* (1968)] modified for continuous heating. The geometrical configuration and symbols of the sintering particles follows Johnson [Johnson *et al.* (1968)] are shown in Fig. 2.1. Each particle is represented by a sphere with radius *a*. ρ is the radius of the neck surface, α is a measure of the grain boundary groove angle, *c* is the distance of the center of the particle to the symmetry plane, δ is the extent of the overlapping of the two spheres, and A_V is the surface area of the neck. The value of *c* gives an indirect measure with respect to the mechanisms at work. Its value will only decrease from its initial value if material is moved between the particles by grain boundary or volume diffusion. It is also assumed that *a* is unchanged during the sintering. This geometry is valid only until *x* = *a*. At that value, the system assumes a "pill" shape. This is sufficient for modeling the necking growth, but can not follow the system all the way to complete coalescence.

With a few additional geometrical parameters defined as follows, $y=\frac{a-c}{a}$, $X=\frac{x}{a}$, $R=\frac{\rho}{a}$, and $\theta=\sin^{-1}(\frac{a-ya+\rho\sin\alpha}{a+\rho})$, the exact equations for the geometrical parameters can be written as [Johnson *et al.* (1968)]:

$$\rho=\frac{a(y^2-2y+X^2)}{2(1-(1-y)\sin\alpha-X\cos\alpha)} \tag{2-2}$$

$$A_V=4\pi\rho[(\theta-\alpha)(a+\rho)\cos\theta-\rho(\sin\theta-\sin\alpha)] \tag{2-3}$$

$$X = (1+R)\cos\theta - R\cos\alpha \tag{2-4}$$

The total volume of the material that has moved into the neck, defined as V_T, will be the sum of the volume of overlap of the original sphere V_B and the volume of material arriving from the sphere surface V_S. The schematic of V_B and V_T are shown in Figure 2.1. Thus,

$$V_T = V_B + V_S \tag{2-5}$$

By geometry reasoning,

$$V_T = 2\pi a^3 R^2 (1+R)[2(\sin\theta - \sin\alpha) - \cos\theta(\sin\theta\cos\theta + \theta - \sin\alpha\cos\alpha - \alpha) - \sin\theta(\sin^2\theta - \sin^2\alpha\alpha)]$$
$$V_B = (\frac{2\pi a^3 y^2}{3})(3-y) \tag{2-6}$$

In order to evaluate V_B and V_S, the mechanisms of the neck growth needs to be identified. It is known for nano-size particle sintering, only grain boundary and surface diffusion mechanisms are in effects [Zhang *et al.* (1998)]. Therefore, let J_{GBD} and J_{SD} represent the material flux, then

$$\frac{dV_S}{dt} = \Omega J_{SD} \tag{2-7}$$

$$\frac{dV_B}{dt} = \Omega J_{GBD} \tag{2-8}$$

where Ω is the molar volume. The individual flux can be calculated from the equations derived by Johnson [Johnson *et al.* (1968)]. By expressing the flux in terms of stress gradients rather concentration gradients and assuming the stress distribution is a function of radial position along the grain boundary, the grain boundary flux can be written by:

$$J_{GBD} = \frac{8\pi\gamma b D_B (x + \rho\cos\alpha)}{kTx\rho} \tag{2-9}$$

The surface diffusion flux can be written as a function of concentration using Fick's equation. The variation of the concentration of vacancies due to surface curvature can be expressed in terms of geometrical parameters. Therefore the surface diffusion flux can be written by:

$$J_{SD} = \frac{2\pi\gamma\Omega^{1/3} D_S (X + 2XR - R\cos\alpha)}{akTR^2} \tag{2-10}$$

where D_B and D_S are the diffusion coefficients for grain boundary and surface respectively, b is the thickness of the region of enhanced diffusion at the grain boundary, k is the Boltzmann constant, T is the temperature and γ is the surface tension.

The temperature of the particle subjected to laser irradiation can be calculated by assuming uniform temperature inside the particle and neglecting the temperature increase due to the reduction of surface area:

$$\frac{dT}{dt} = \frac{IA_{cross}\kappa}{CV_P} \tag{2-11}$$

where I is the laser intensity, A_{cross} is the cross section area of the particle, C is specific heat, V_P is particle volume, and κ is the absorption efficiency which is determined from predetermined heating rate.

The implementation of the above model is described as the following. Equation 2-11 is used to calculate the temperature at any instant of time. The rate equations for the neck volume (Equ. 2-7 to 2-8) were integrated numerically with respect to time to update the neck volume based on the flux equations 2-9 to 2-10. At each time step, the simultaneous nonlinear equations (Eq. 2-2 to 2-6) governing the geometry were solved using a Powell-Hydrid algorithm in Matlab to obtain the new necking profile. An initial temperature and neck volume were specified to begin the computation.

2.3 Results and Discussion

2.3.1 Extracting Physical Properties from MD simulations.

The self-diffusion coefficient D is calculated from the slope of the atomic mean-square displacement (MSD):

$$MSD = \frac{1}{N}\sum_{i=1}^{N}[r_i(t) - r_i(0)]^2 \tag{2-12}$$

$$D = \frac{1}{6}\frac{d}{dt}(MSD) \tag{2-13}$$

where N is the number of atoms sampled and r is the position of each atom. For the present study, D is evaluated for surface atoms. The extracted surface diffusivities for different particle sizes are plotted in Figure 2.2a. It is interesting to note that smaller particles have higher diffusivities, qualitatively in agreement with empirical consideration of size effects on diffusivity [Xing *et al.* (1999)]. For the present study, grain boundary diffusivity D_B is estimated to be same as of surface diffusivity D_S [Saitoh *et al.* (1999)].

The surface tension is computed using the mechanical approach reported by Thompson [Thompson *et al.* (1984)].

$$\gamma = \left(-\frac{(p_L - p_G)^2}{8} \int_0^\infty r^3 \frac{dP_N(r)}{dr} dr \right)^{1/3} \tag{2-14}$$

where p_G is the gas pressure outside the particle, which is neglected and p_L is pressure inside the particle and P_N is the normal component of the pressure to the spherical surface. It is worth mentioning that the term $\frac{r}{2}\frac{dP_N(r)}{dr}$ in this equation stems from the mechanical arguments [Thompson *et al.* (1984)] that relate surface tension γ to $P_N(r) - P_T(r)$, where the tangential component of the pressure P_T can be related to P_N by $P_T(r) = P_N(r) + \frac{r}{2}\frac{dP_N(r)}{dr}$. The p_L and P_N were obtained following the procedures described in [Thompson *et al.* (1984)]. Since the pressure outside the particle is neglected then the upper bound in the integration in Equ.2-14 is actually the particle radius. It should be pointed out that Equ.2-14 is valid for gas-liquid interface. This liquid droplet model is applied to solid nanoparticles in this work as an approximation. The validity of this approximation is based on a recent publication [Nedasani *et al.* (2007)] where the calculated surface stresses for silver nanoparticles (similar size as the particles considered in this work) are close to the theoretical values of surface energies. The calculated surface tension is plotted in Figure 2.2b along with an empirical model from Murr [Murr *et al.* (1975)]. A reasonable agreement was found except that the extracted values are lower than the empirical bulk data, which might be due to small size effects [Thompson *et al.* (1984)].

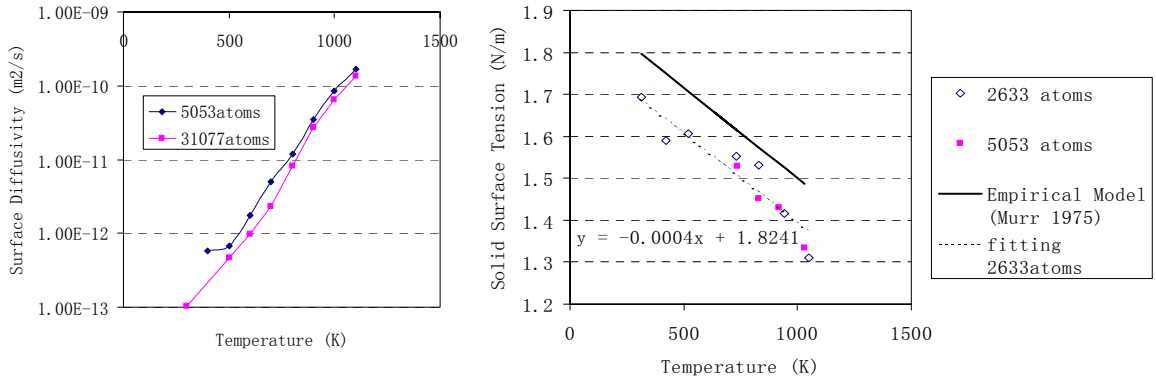

Fig. 2.2 Extracted diffusion coefficients (a) and surface tension (b) from MD simulation.

2.3.2 MD results.

Owing to their ultra-fine size, sintering can occur between two bare nanoparticles at low temperature without laser irradiation. The qualitative features of the sintering of two nanoparticles (2633atoms, 2.2nm radius) at 300K are clearly seen in Figure 2.3a where the neck width is plotted against time. The sintering consists of two phases, i.e. a very fast neck growth within 10ps wherein the neck grows to about 1.2nm, followed by a slower process that increases the neck radius to

about 1.5nm within 150ps. It is clear that the first fast neck growth is due to elastic deformation. According to Zhu [Zhu *et al.* (1996)], the upper limit of the contact radius due to elastic deformation of two 2.4nm Cu nanoparticles is 0.84nm. This value is on the same order of the neck width observed after the first neck growth. The slow growth after the elastic deformation is due to the movement of the atoms near the void that is driven very strongly toward the void by very high atomic potential gradients where two surfaces of rapid curvature form a sharp cusp on contact [Zeng *et al.* (1998)].

The resulted dump-bell shape particle pair is then subjected to laser irradiation. The evolution of the radius of gyration along the inter-particle axis of the particle pair is plotted against temperature for different particle sizes in Figure 2.3b. For each size particle, there are two obvious drops of the gyration radius, labeled as *B* and *D*. It is obvious that for both cases the turning point *D*, marking the full coalescence, is due to melting. For the 2633 atom particles, the evolution towards equilibrium shape is continuous at high temperature (after *B*) and more steplike at low temperature (before *B*), indicating that at high temperatures atoms continuously move to their final positions, whereas an additional discontinuous mechanism is operative at low temperatures. One possible mechanism is the presence of facets, which persist or rearrange during coalescence in a discontinuous manner [Combe *et al.* (2000)]. Another more likely mechanism is due to the plastic deformation induced by a large number of small 'sliding' events of atomic planes at the grain boundaries or dislocations within the grains [Schiotz *et al.* (1998)]. To provide insight into the atom movements, a vector field showing the atom trajectory is shown in Figure 2.4a. Each vector connects the positions of an atom before and after the shape transition. The atom trajectory between *A* and *B* reveals that one particle is almost uniformly sliding in one direction and the other moves in another direction and that most of the sliding deformation occurs near the grain boundary. To better understand this sliding mechanism, crystalline structure of atoms was identified via determining the bond order parameters. Atoms in local f.c.c order are considered to be inside the crystalline grain and colored as yellow; atoms in local h.c.p order are classified as stacking faults and colored green. All other atoms are considered as belonging to the grain boundaries or amorphous layers, colored gray, shown in Figure 2.3c. It is seen that crystalline structure is formed in the necking region after the initial rapid neck growth at low temperature (400K). At the beginning of the heating process, a dislocation at the necking region is developed indicated by a plane of stacking faults (h.c.p). During the heating, instead of increasing the h.c.p atoms, the grain boundary (amorphous) atoms keep growing at the necking region suggesting that grain boundary sliding could be responsible for most of the steplike transformations up to the turning point *B*.

For particles consisting of 5053 atoms, the quick drops at *B* and *D* can still be distinguished. However, unlike the case for 2633 atoms particles, the steplike drops before *B* is absent. The reason could be because larger size particles can pile up dislocations in the interior, rendering the dislocation mechanism less important [Zeng *et al.* (1998)]. Meanwhile, with a lower fraction of atoms assigned to grain boundaries, the grain-boundary sliding becomes less possible [Schiotz *et al.* (1998)]. Instead, the atom trajectory reveals that grain boundary diffusion is the dominant mechanism at this point, as shown in Figure 2.4b, where atoms migrate along the boundary between two particles. To study the mechanism of the observed drop at point *B*, the atom motion trajectory between *B* and *C* is also plotted in Figure 2.4c. It can be seen a large portion of atoms move from the center region to the neck region. Contrary to what one might expect, the movement as observed through the atomic motion is not symmetric. Evidently, the neck grows by surface diffusion at the 'top' of the particle, while interior atoms move down to fill in the neck at the

'bottom', developing a flow pattern similar to the reported by Zachariah [Zachariah *et al.* (1999)] in a simulation of coalescence of two 580-atom particles. It appears that coalescence takes place via both a surface and a grain boundary mechanism. However, unlike the conventional grain boundary diffusion where atoms migrate along a very thin grain boundary layer [Johnson *et al.* (1968)], a large portion of atoms outside the grain boundary layer also participate in the movement. The flow pattern resembles a viscous flow type motion. The deviation from normal diffusion could be attributed to the failure of linear diffusion kinetic law in the presence of the large driving force for these nanoscale dimensions [Pan *et al.* (2004)]. This can also be attributed to the accumulation of amorphous layer. Calculation of the fraction of atomic structure composition reveals that at point *B*, around 78% of the atoms are amorphous. It is known that viscous flow is a very important mechanism for amorphous materials [Exner *et al.* (1979)]. The accumulation of amorphous layer enabling rapid viscous flow driven by surface curvature to reduce surface energy could be another possible reason for the drop at point *B*. Wang [Wang *et al.* (2003)] also reported a pre-melting transformation accompanying a structural change from fcc to hcp. It was suggested in his paper [Wang *et al.* (2003)] that it is the building up of an amorphous layer during the heating process that drives the pre-melting transformation where planes of atoms slide against each other, thus transforming fcc atoms into hcp and vice versa. The transformation in the present study can be due to a similar mechanism, except that no structural change is found, which could also be attributed to the exceptionally high fraction of amorphous atoms. Lastly, it needs to be pointed out that for such small particles, surface energy tends to be very important, therefore resulting in a surface tension driven atomic migration that might be faster than normal force free diffusion migration. To quantitatively understand the difference in neck growth rate, MD results will be compared with analytical predicting in next section. Starting from *C*, the evolution slows down due to the so-called 'spherication' process. This process is driven by curvature induced surface diffusion. This process continues until *D* where melting occurs and the cluster collapses into a sphere.

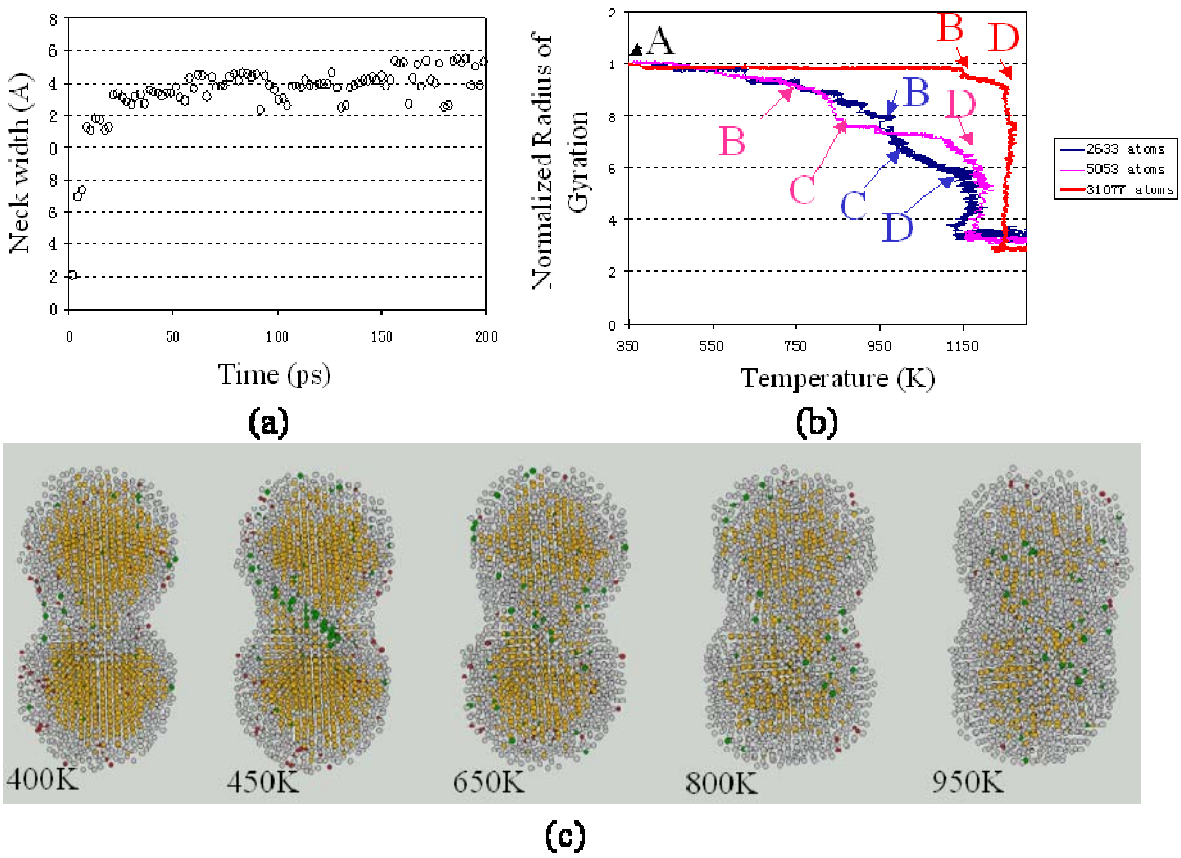

Fig. 2.3 Initial neck growth with respect to time (a), the temperature dependence of the radius of gyration. The transitions points are labeled as B, C, D for each size particle. The blue, purple and red labels and curves represent 2633, 5053 and 31077atom particles respectively (b). and configurations of the 2633atoms particle pair at different temperature with atoms colored according to their local structure.

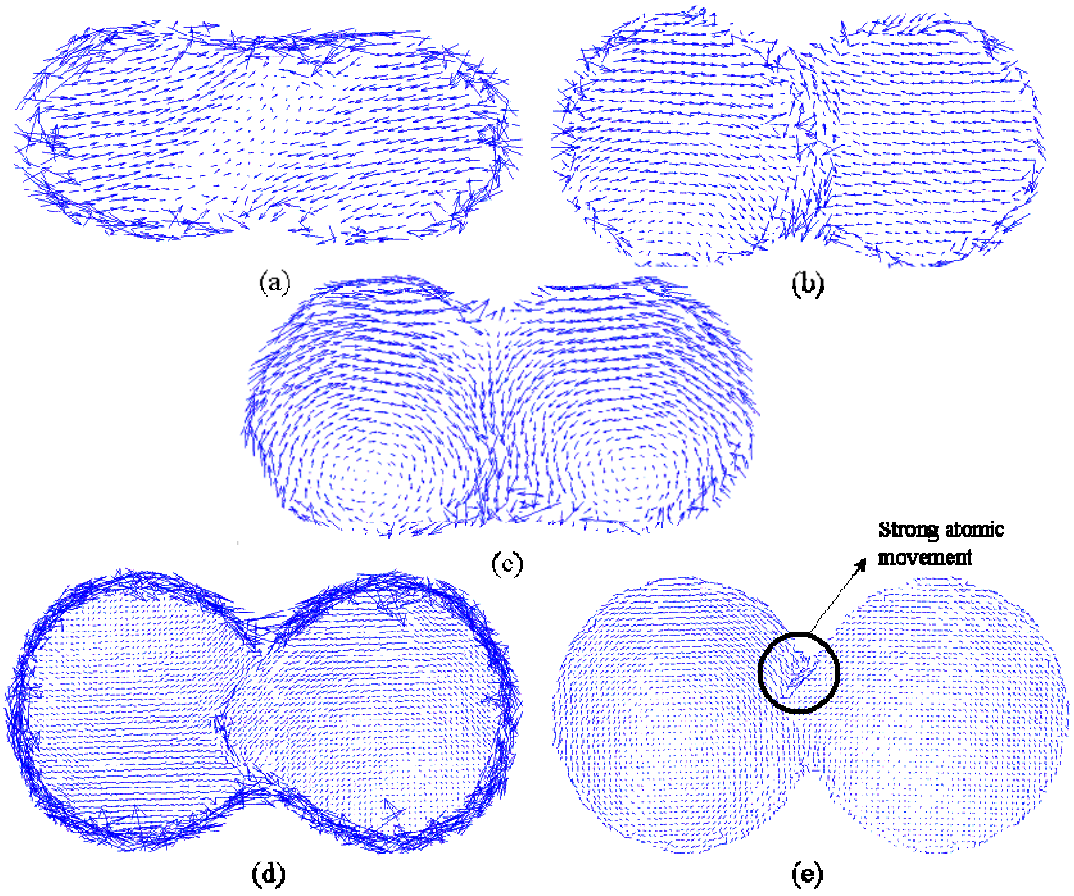

Fig. 2.4 Motion of atoms during the transition from A to B for 2633 atoms (a), from A to B (b) and B to C (c) for 5053 atoms particle; Figures subtitled (d) and (e) represent the motion of atoms for 31077atom particles during the transition between the two points indicated by arrows in Figure 2.5c and in Figure 2.5d respectively.

For larger particle (31077-atom), it can be noted that the transition points (*B* and *D*) approach each other [Wang *et al.* (2003)]. As a consequence, the transition point *B* is less apparent and occurs very close to *D*. Correspondingly, the reduction of the radius of gyration is completed almost entirely by the melting transition for the large particles with the heating rate considered. As will be pointed out in Sec.3.3, grain boundary and surface diffusions are the major mechanisms for neck growth before reaching melting for this size of particle. To summarize, the major contributing solid-state neck growth mechanisms during laser heating for different particle sizes are listed in Table 1.1.

Size	Major Solid-state Neck Growth Mechanisms during Laser Heating
2633 atoms	Grain boundary slidings/dislocations; Surface diffusion;
5053 atoms	Grain boundary diffusion; Surface diffusion; Viscous flow;
31077 atoms	Grain boundary diffusion; Surface diffusion;

Table 1.1 Summarized major neck growth mechanisms during laser sintering for different particle sizes.

2.3.3 Comparison with neck growth model.

The time resolved neck growth during the heating predicted by the modified neck growth model for solid-state diffusion is plotted along with MD simulation results for 5.4nm (5053 atoms) and 10nm (31077 atoms) particles subjected to different heating rates. It can be found that the analytical modeling always underestimates the growth rate for 5.4nm particles when the neck growth undergoes through the intermediate transition (point *B*, indicated in Figure 2.3&2.5). The possible causes for this departure have been discussed in the previous section. On the contrary, satisfactory agreement can be found for 31077-atom (10nm) particles. In Fig. 2.5c, the solid-state neck growth model reasonably predicts the neck radius, indicating that surface diffusion and grain boundary diffusion are mostly responsible for the neck growth. Correspondingly, Fig. 2.4d showing the atomic trajectory between the two arrows as described in Fig. 2.5c, clearly indicates very active atomic movement can only occur at the surface and along grain boundary in agreement with the analysis. The agreement in Fig. 2.5d is less satisfactory mostly due to step-wise neck growth indicated in the figure. Similarly, to provide an insight into this step-wise transition, the atomic trajectory between the arrows as indicated in Fig. 2.5d is plotted in Fig. 2.4e. It can be seen that the major contributions of atomic movements originate from the contact line of the neck surface. The radius of the neck surface is very small and therefore a deviation of neck growth rate can be expected as explained by Pan [Pan *et al.* (2004)] and Zeng [Zeng *et al.* (1998)].

It should be pointed out that in current study, only the solid-state diffusion driven neck growth within the entire sintering and coalescence process has been discussed using the analytical model. The temperature range covered so far is below equilibrium melting temperature. The remaining of the neck growth process and the completion of the coalescence require the particle temperature to approach or even exceed the melting temperature, where especially higher neck growth rate is expected as described in Fig. 2.5 for the final stage in the process. It is believed that the final stage can be described by the K-F model [Friendlander *et al.* (1994)] with given precise values of viscosity (as a function of temperature). Evaluation of the viscosity using MD simulation to complete the description of the coalescence is still under investigation.

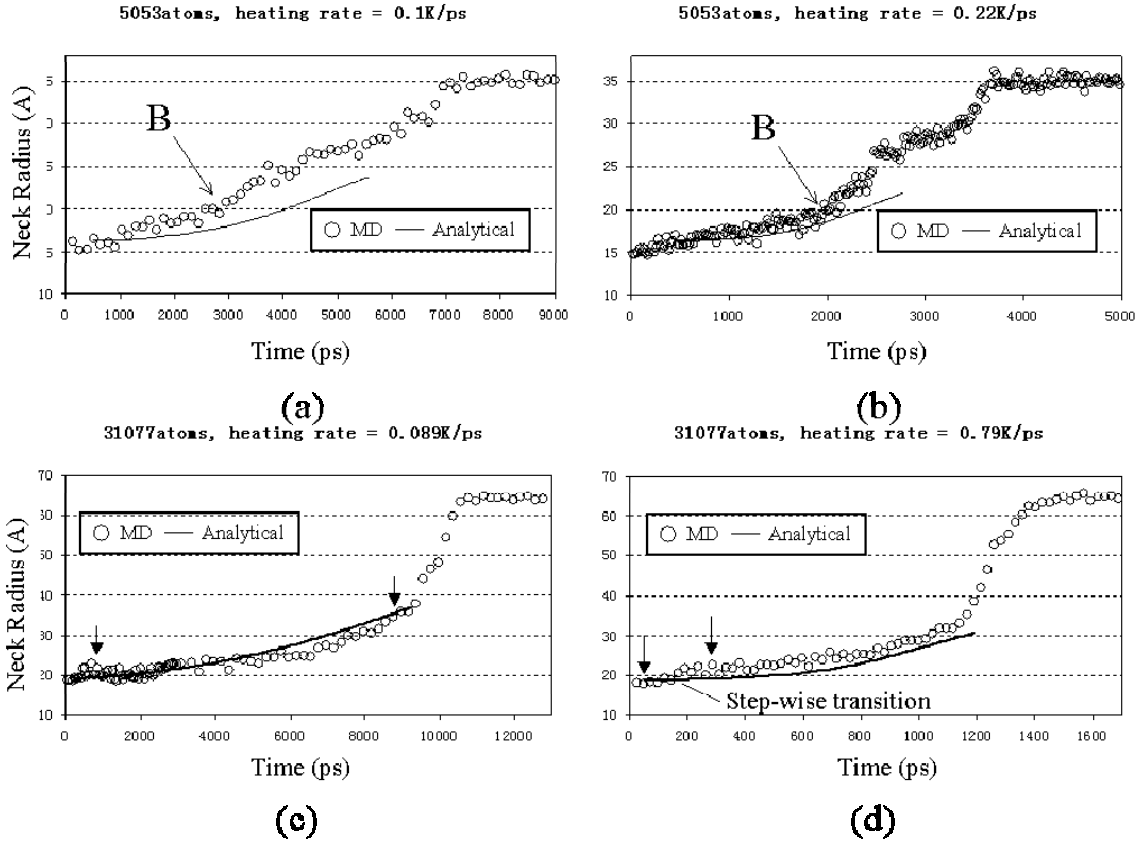

Fig. 2.5 The comparison between analytical model and MD simulations for 5053atoms (a)(b) and 31066atoms (c)(d). Solid line is the analytical model and circle is MD simulations.

2.4 Conclusions

Molecular Dynamics Simulation was applied to study the solid diffusion necking growth of gold nanoparticles induced by laser heating. A classical neck growth model was modified to enable prediction of the neck growth during the continuous heating process. With the assistance of MD simulation, the detailed neck growth mechanisms were identified and analyzed for different particle sizes. Satisfactory agreement between analytical neck growth model and MD simulation was found only for large particles (10nm). The small grain size effects for particle below 10nm are the major causes for the failure of the conventional model.

CHAPTER 3

FUNDAMENTAL STUDIES OF LASER INDUCED MELT-MEDIATED NANOPARTICLE COALESCENCE

Gold nanoparticles supported on a quartz substrate are fabricated by e-beam lithography and subjected to nanosecond laser irradiation to induce coalescence. In combination with ex-situ Scanning Electron Microscopy and optical extinction spectra, transmission is monitored in-situ to determine the characteristic coalescence time, the threshold fluence for the onset of coalescence and the produced particle morphology. Parallel Molecular Dynamics simulation is employed and shown to reasonably predict the coalescence time, explaining the experimental results.

3.1 Introduction to laser induced nanoparticle coalescence and pump & probe method.

Recent interest in fabricating flexible electronics has spurred research related to defining both active and passive device components in a cost effective and precise manner. The printing of nanoparticles followed by low temperature thermal treatment has shown substantial promise for ultra-low-cost electronics fabrication. Employing laser radiation to define micron and even sub-micron features offers considerable advantages in terms of meeting performance and cost requirements [Ko *et al.* (2007), Chung *et al.* (2004), Ko *et al.* (2006), Ko *et al.* (2007)].

Previous research efforts on laser patterning of nanoparticle-laden materials in micro-fabrication as well as potential applications in nano-fabrication have sparked great interest in understanding the fundamental phenomena involved in the laser-induced nanoscale phase change and coalescence transformation. These processes can be utilized efficiently for realizing low resistance ohmic nanocontacts [Kim *et al.* (2005)] and are also of interest to the plasmonic optics community due to the wide application of supported nanoparticle arrays. Accurate control of the sintering/coalescence process induced by laser irradiation requires knowledge of the desired laser energy density and irradiation time to initiate changes in the particle morphology [Su *et al.* (2003), McMahon *et al.* (2006)]. Pump-and-probe techniques have been applied extensively to observe picosecond dynamics of electron-phonon relaxation [Hodak *et al.* (1998)], phonon-phonon relaxation events [Hu *et al.* (2004)], and even femtosecond dynamics of excited electrons [Fann *et al.* (1992)] in nanoparticle systems. These methods have also been used to ascertain the dynamics of the laser induced shape transformation [Link *et al.* (1999)] and the size reduction [Plech *et al.* (2005)] of gold nanoparticles or nanorods suspended in aqueous solutions on the picosecond scale. Recently, transient absorption was monitored in the nanosecond time scale and longer [Inasawa *et al.* (2006)], mostly in the context of observing phase change related phenomena. However, no study has been reported on the coalescence dynamics.

In this work, we probe the nanoparticle coalescence process in real time. In conjunction with ex-situ scanning electron microscopy and optical extinction spectra, we quantitatively determine the coalescence time and threshold laser fluence for coalescence. Furthermore, parallel Molecular Dynamics is employed to compare with the experiments.

3.2 Experiment and Simulation Methods.

The gold nanoparticles were prepared on quartz substrates by electron-beam lithography (EBL) and a standard lift-off process. To reduce charging effects during EBL, 10-nm-thick indium tin oxide (ITO) films were sputtered on the quartz substrates. Polymathylmethaacrylate (PMMA) films were then spin-coated on this ITO-quartz glass and used as positive photoresists for e-beam lithography. For these experiments, samples were fabricated as periodic rectangular arrays of pairs of gold nanoparticles, shown in Figure 3.1. By varying the electron dose and inter-particle distance, the diameter of fabricated nanoparticles is controlled to be about 100nm with the neck width ranging from 0-60nm. The samples were examined by Field Emission Scanning Electron Microscopy to characterize size and shape. Typical patterned areas were approximately $60 \times 60 \mu m$ consisting of nine $20 \times 20 \mu m$ sub-areas for each single laser processing. Due to the non-wettabilty of the Au/ITO interface and that fact that the cohesion between gold atoms is larger than the adhesion between Au and substrate, the gold particles will coalesce into a single particle and establish an equilibrium contact angle upon laser heating without spreading into a thin liquid film.

The gold nanoparticles were excited using Nd:YLF laser irradiation (Spectra-Physics) with $\lambda = 527 nm$ and pulsed width = 30ns (full width at half maximum), focused by a 10X long

working distance objective lens at an angle of incidence of 45 degrees onto the sample. The polarization of the excitation laser was set along the inter-particle axis. The Nd:YLF pulse was only mildly focused to an ellipsoidal spot with short axis length of ~11 μm and long axis ~18 μm. A monochromator and a photodetector (J.A. Woollam) were used to obtain static transmission/extinction spectra in the 450nm-800nm range. For the transient measurement, a continuous wave He-Ne laser of 633nm was used at normal incidence on the surface. The probe laser light was focused to ~6 μm and transmitted through the center of the excited area, so that the effects of the intensity variation of the pulsed laser beam across the ellipsoidal area could be minimized. The transmitted light was detected by a fast Si photodiode (Thorlabs) and the signals were amplified and recorded with a fast digital storage oscilloscope (H.P., Infinium). An interference filter placed in front of the photodiode suppressed any contribution of the laser pulse to the measured signal. Figure 3.1 illustrates the experimental setup details as well as the pump and probe laser configuration (Fig. 3.1b).

The Discrete dipole approximation (*DDA*) has been proved very efficient and accurate in modeling the spectral properties of metallic particles such as gold and silver [Draine *et al.* (1994)]. In this work, the *DDA* program DDSCAT developed by Draine and Flatau [Draine *et al.* (1994)] was used to simulate the extinction spectra of arrays of nanoparticle pairs before and after the laser irradiation and compare with experimental results. To achieve better understanding of the phenomenology and specifics of the coalescence process of gold nanoparticles, classical Molecular Dynamics is employed based on a reliable model for the inter-atomic potentials, called the glue potential [Ercolessi *et al.* (1998)]. In the glue model, the potential energy of a system of N atoms consists of a sum of pair potentials and a many-body glue energy:

$$V = \frac{1}{2}\sum_{ij}\phi(r_{ij}) + \sum_{i}U(n_i) \tag{3-1}$$

where r_{ij} is the distance between two atoms, $\phi(r_{ij})$ is a standard two body potential, $U(n_i)$ is the energy associated with the coordination n_i of the atom i, $n_i = \sum_j \rho(r_{ij})$ is defined as the superposition of contribution from neighbor atoms and $\rho(r)$ is a short-range monotonically decreasing function of distance. It is worth mentioning that glue model can consider all the mechanisms involved in the coalescence process, including atom diffusion and fluid flow under the influence of surface tension, etc. The details of the model and its parameters are given in reference [Ercolessi *et al.* (1998)]. A parallel *MD* program is developed that is capable of computing up to 200,000 atoms at a reasonable computation time. This enables the study of nanoparticles (nanodisks) of size ranging from 2.5nm to 15nm. Two identical particles were brought into contact and placed on a smooth substrate. Particles considered in this study are of size ranging from N=815 to N=61786 atoms. The substrate is a slab of dimension $250\times350\times10A^3$ made of 51580 atoms. The substrate atoms were considered frozen in order to increase the simulation time. The interaction between substrate and Au atoms was assumed to be of the Lennard-Jones type.

$$V_{ij} = 4\varepsilon\left[\left(\frac{\sigma}{r}\right)^{12} - \left(\frac{\sigma}{r}\right)^{6}\right] \tag{3-2}$$

The parameter of σ = 0.27nm was kept constant, and the well depth ε was chosen to be 0.1eV to simulate moderate adhesion interaction.

3.3 Results and Discussions

The linear optical properties of the array of nanoparticle pairs were examined via polarized white light transmission at normal incidence. The optical field was polarized along the inter-particle axis. Figure 3.2a shows the extinction spectra with different neck widths and accompanying SEM images for each representative particle configuration. Samples labeled as *A* having smaller neck width (~0-20nm) and *B* with larger neck widths (~60nm) were fabricated by e-beam lithography via varying the inter-particle distance. Sample *C* was produced by subjecting *A* to a single laser pulse. The *DDA* simulation results are presented to provide qualitative prediction of the corresponding plasmonic resonance (Fig. 3.2b). No attempt is made herein to predict the exact resonance spectral location since this will shift by a substantial amount depending on the array lattice constant and the surrounding medium [Haynes *et al.* (2003), Zhao *et al.* (2003)]. It needs to be pointed out that the experimentally observed characteristic resonance peaks are less clear than *DDA* predictions. This is mostly due to the manufacturing issues: the variation of the morphology of each particle pair exists within the array and e-beam fabricated particle shape deviates from sphere and appears to be elliptical due to e-beam stigmation. All these induce the broadening of the resonance. However, both simulation and experiment clearly show similar trends in describing the "neck" size effects on the associated spectral characteristics. For pairs with necking (A and B), the spectral characteristics show a clear contribution to the extinction coefficient at two distinct wavelengths, that is, one located at visible and one at infrared. With the particle pair overlap increasing (A->B), the long wavelength resonance increases and blue shifts accompanied by the reduction and blue shift of the short wavelength resonance. These results are consistent with previous studies [Atay *et al.* (2004), Gunnarsson *et al.* (2005)]. This optical response can be interpreted by different multipolar orders for plasmon polariton contributions [Atay *et al.* (2004)]. For example, the Mie solution for single insolated nanoparticles can be viewed as a superposition of dipole, quadrupole and higher order contributions. For diameters up to about the 100nm range, the quadrupole contribution can effectively compete with the dipolar mode. The idea of competing dipole and quadrupole modes is applicable to explain the necking effects [Atay *et al.* (2004)]: particle pairs with small neck *A* can favor the quadrupole mode, while for particles with larger neck *B*, the dipole mode establishes dominance. For particles of the *C* type morphology that are spherical, multipolar resonances overlap and form a collective resonance at ~600nm. Based on the characteristics of the plasmon spectrum, for the present study, the laser wavelength at 633nm was chosen for observing the permanent shape transformation by coalescence.

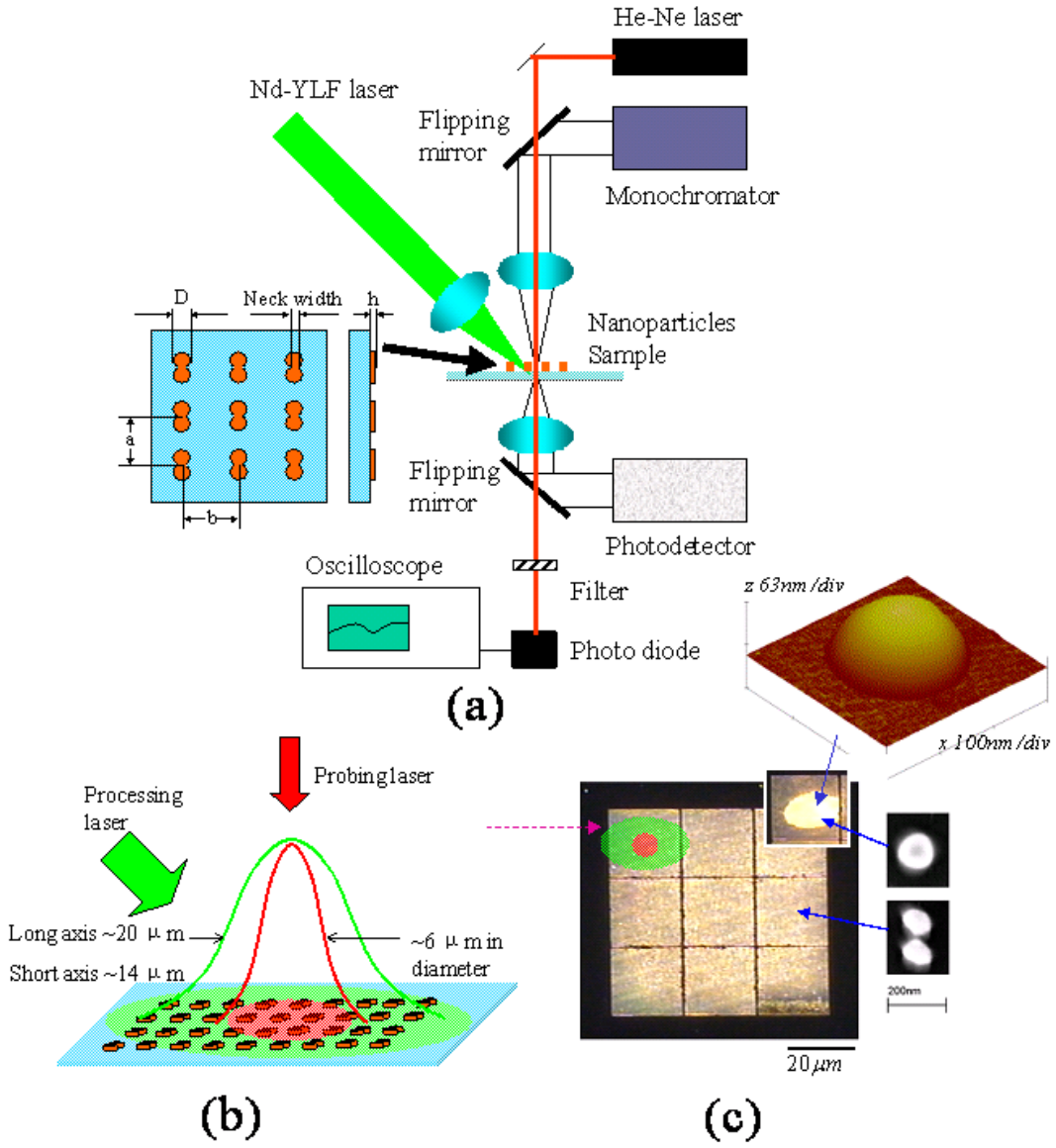

Fig. 3. 1 Experimental setup and array of nanoparticle pairs on ITO coated quartz wafer (a). The diameter *D* is ~100nm and height *h* is ~30nm. For each sample, the lattice constant *a* is 250nm and *b* is 400nm. (b) The relative pump and probe laser beams configurations are illustrated. (c) Unpolarized dark-field optical image of the patterned area consisting of 9 sub-areas. The pattern produced after the ns laser irradiation is shown as inset. The laser induced coalescence is indicated by strong contrast between processed area and unprocessed area as well as the morphology change shown in the inserted *SEM* and *AFM* images, the AFM image shows that the resulted particle after coalescence is semispherical in cross-section.

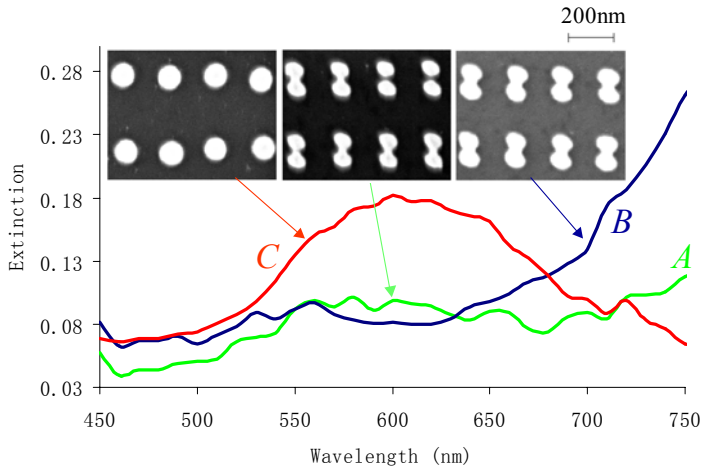

(a)

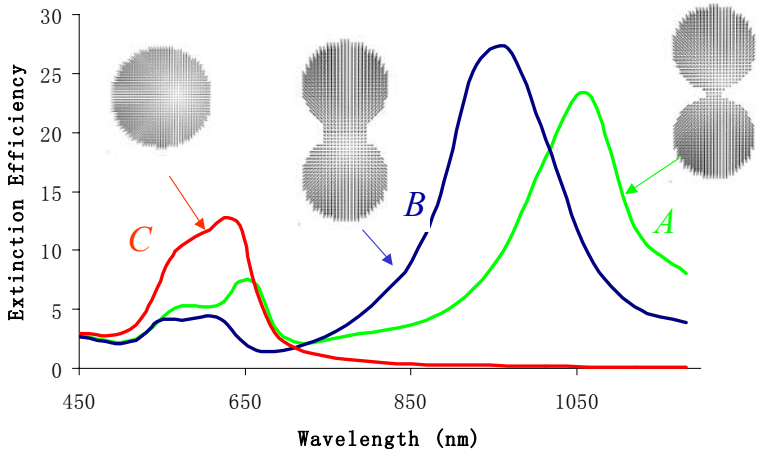

(b)

Fig. 3. 2 Polarized extinction spectra in periodic arrays of pairwise gold nanoparticles with different neck profiles. (a) Experimental measurement of the spectral response of *A* and *B* samples fabricated by adjusting the inter-particle distance in e-beam lithography. *C* is produced from the *A* sample upon laser irradiation. (b) *DDA* Simulation results.

A series of tests with different laser fluences (from 100 mJ/cm^2 to 335 mJ/cm^2) was performed where the optical extinction spectra were measured before and after laser irradiation. It was found that for laser fluences between 130 mJ/cm^2 and 210 mJ/cm^2, the weak resonance located in the visible range grows into a much stronger resonance at ~600nm (Fig. 3.2a). Correspondingly, a distinct color change can be observed via optical microscopy, as shown in Fig. 3.1c. The spectrum remains unchanged upon laser irradiation. At lower fluence (<~130 mJ/cm^2), no changes can be detected.

The transient transmission traces of the probing laser (633nm) are shown in Fig. 3.3 along with the temporal profiles of the excitation laser for a wide range of laser fluences. At an energy density of 150 mJ/cm^2 (Fig. 3.3(a)), the transmission signal bleaches by two consecutive transitions. The first transition, having a characteristic time of ~6ns, occurs within the laser pulse duration and is followed by a plateau. The plateau lasts for ~30ns until the second transition takes place with a slightly longer characteristic time. Corresponding SEM images reveal that spherical particles are generated via coalescence of particle pairs with no observable mass loss. For higher fluence 210 mJ/cm^2, the two-step transition is less evident and the signal appears to bleach with a longer characteristic time ~28ns. For the highest fluence applied, 334 mJ/cm^2, the signal bleaches and thereafter recovers almost to the original level. Similar results were observed for pulse energy higher than 210 mJ/cm^2. The SEM images could help attribute the cause of the recovery to the reduction of the particle size, possibly via evaporation. Therefore, the laser fluence window suitable for ns laser induced coalescence should be between 130 mJ/cm^2 and 210 mJ/cm^2. Close to the upper limit of this range at 210 mJ/cm^2, it is believed that particles are fully melted. In addition, slight evaporation maybe expected, as indicated by the SEM image that reveals a certain reduction in particle size.

The heating rate of nanoparticle pairs subjected to laser fluence at 150 mJ/cm^2 can be estimated with first order accuracy, to be $6.5\times10^{11} K/s$ by assuming a simple lumped capacitance thermal model and neglecting heat loss to the surroundings. The specific heat used is 128*J/kgK*, density is 19300 Kg/m^3 and the absorption efficiency calculated from DDA is ~0.96. Based on a modified heat conduction model [Habenicht *et al.* (2005)] accounting for the interfacial (Kapitza) thermal resistance between the particle and the substrate, a realistic heating rate could be 5-10 times lower.

For the case of the lower fluence of 150 mJ/cm^2, the estimated temperature could exceed the melting temperature within the laser pulse duration but remain far below the boiling point. In the context of pulsed laser interaction with materials, the equilibrium boiling point does not have a particular physical significance but serves as a rough indicator for conditions of substantial ablative material removal. Therefore, the two-step transition described previously can be interpreted in the following way: the first transition observed is due to melting induced structural change, whereas the extinction efficiency is significantly increased due to the coalescence corresponding to the observed transmission signal drop. The characteristic time will be discussed later through MD simulation. After this transition, heat is transported into the substrate. Solidification of the liquid particle begins after tens of ns, releasing latent heat that compensates the conductive heat transfer loss. Consequently, the second transition is due to solidification after substrate cooling. Phase transition could be accompanied by jumps in the optical constants [Otter *et al.* (1961)]. Consequently, a separate experiment was conducted to examine this effect: the particle sample produced after coalescence was subjected to pulsed laser radiation and the

transmission signal was recorded and shown in Fig. 3.4. It can be seen that upon laser irradiation, the particle array exhibits higher transmission with the signal dropping to the original level tens of ns after the laser pulse. This experiment can be repeated, implying that the melting/re-solidification process contributes to the optical signal jumps. To quantify expected transmission changes, the extinction efficiency of a semi-spherical particle (radius ~60nm) on ITO substrate was calculated using *DDA* on the basis of the optical constants as determined by Otter [Otter *et al.* (1961)]. The extinction efficiency can be computed to be 5.12 and 7.54 for liquid and solid respectively at the wavelength of 620nm. Therefore, it is suggested that the observed second transition could be due to re-solidification after cooling.

For the higher fluence of $210\,mJ/cm^2$, the temperature can rise well above the melting point. It is known that gold vapor at pressure higher than 10^4 Pa can be formed [Inasawa *et al.* (2006)] at ~2700K. Since the nascent vapor can effectively scatter light, it may also be responsible for the signal bleach seen in Fig. 3.3b. It is therefore concluded that the long characteristic bleach time (~28ns) could be the result of melting induced structural change and due to scattering related to evaporation. The work function of gold is 5.3eV, which is larger than the excitation source (2.35eV), suggesting that two-photon absorption is needed for electron ejection. Therefore, it is believed that photoemitted electrons are unlikely to cause the observed bleaching in the present study.

In order to characterize and analyze the first transition in Fig. 3.3a, MD simulation employing the glue potential was carried out. Figure 3.5a shows the configuration of the simulation. Despite the fact that a realistic heating rate should be 5-10 times lower, the heating rate of $\sim 5.0\times10^{11}\,K/s$ was chosen in the present simulation, mainly to reduce the computational effort while providing sufficient insight into the physical mechanisms involved. The evolution of the radius of gyration was employed to depict the coalescence during laser heating as shown in Fig. 3.6(a). For the *D*=5nm particles, the coalescence process, indicated by the reduction of the radius of gyration, proceeds very slowly until the temperature reaches ~680K (labeled as *A,* in Fig. 3.6b). The slow process is driven by solid-phase diffusion and possibly hindered by substrate adhesion. Beyond *A*, the radius of gyration drops much faster. The fast decay slows down at 945K and only very gradual decrease can be seen from 945K to 1200K. At 1250K, labeled as *B*, the melting begins and the two particles completely coalesce into a sphere. Wang [Wang *et al.* (2003)] reported a very similar evolution process in MD simulation of the laser heating of gold nanorods. The transition at *A,* that is the so-called intermediate transition [Wang *et al.* (2003)], is explained by the accumulation of amorphous layers while the transition *C* is due to melting. A separate detailed MD study on the coalescence process between *A* and *B* reveals that: a) this evolution process is faster than the prediction by the solid-state diffusion neck growth model. b) the calculation of the fraction of atom structure composition shows that at point *A*, more than 70% of the atoms are in amorphous phase. In reference [Exner *et al.* (1979)], it is well known that viscous flow is a very important mechanism in amorphous materials. The accumulation of amorphous layer enabling rapid viscous flow driven by surface curvature to reduce surface energy could be the reason for the fast intermediate transition, in agreement with Wang's observation. Smaller particles exhibit depression of the melting temperature. This effect is also evident in the present coalescence study, since for the 2.5nm particles the coalescence occurs at lower temperature due to that fact that more atoms are less bounded and located at the surface, therefore having stronger tendency to coalescence and reduce surface energy.

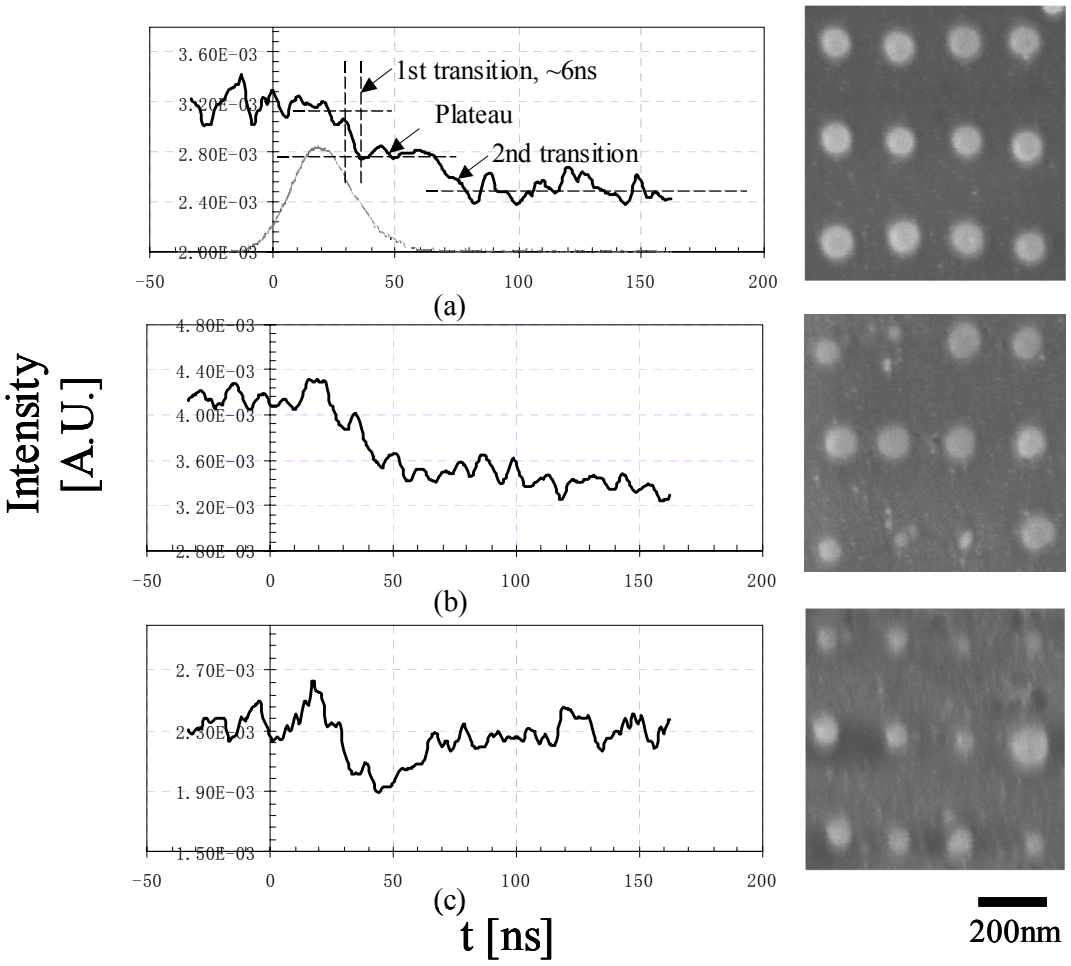

Fig. 3. 3 Time-resolved transmission traces upon pulse laser annealing recorded with 633nm probing laser. The pulse energy at 527nm was (a) 150 mJ/cm^2, (b) 210 mJ/cm^2 and (c) 334 mJ/cm^2 respectively.

.

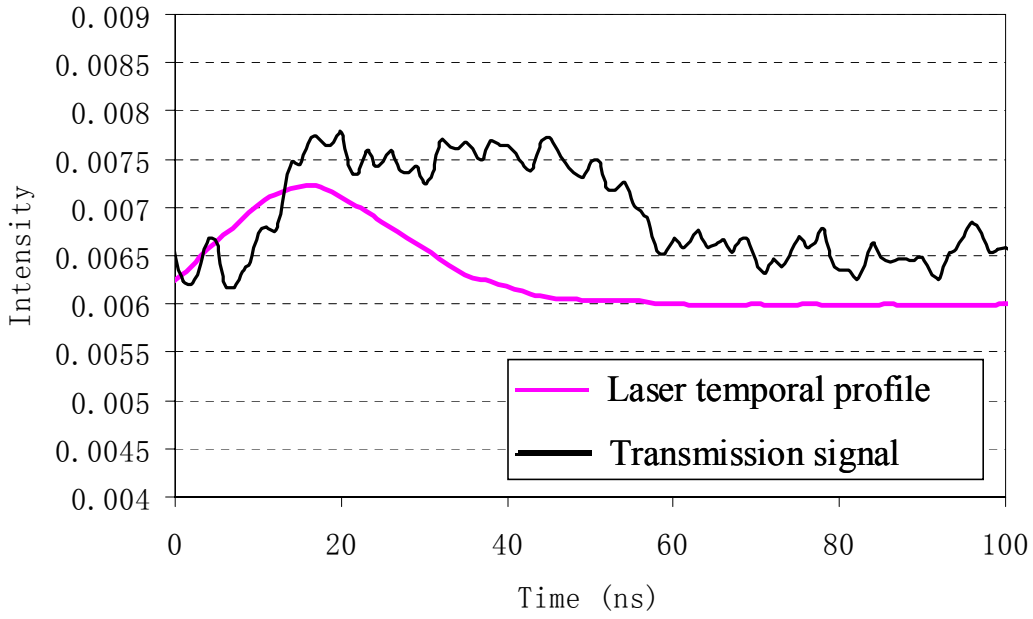

Fig. 3. 4 The time-resolved transmission trace of coalesced particles that have been subjected to laser pulse irradiation. The transmission signal increases upon laser irradiation and drops to the original level tens of ns after the instant of the laser peak intensity.

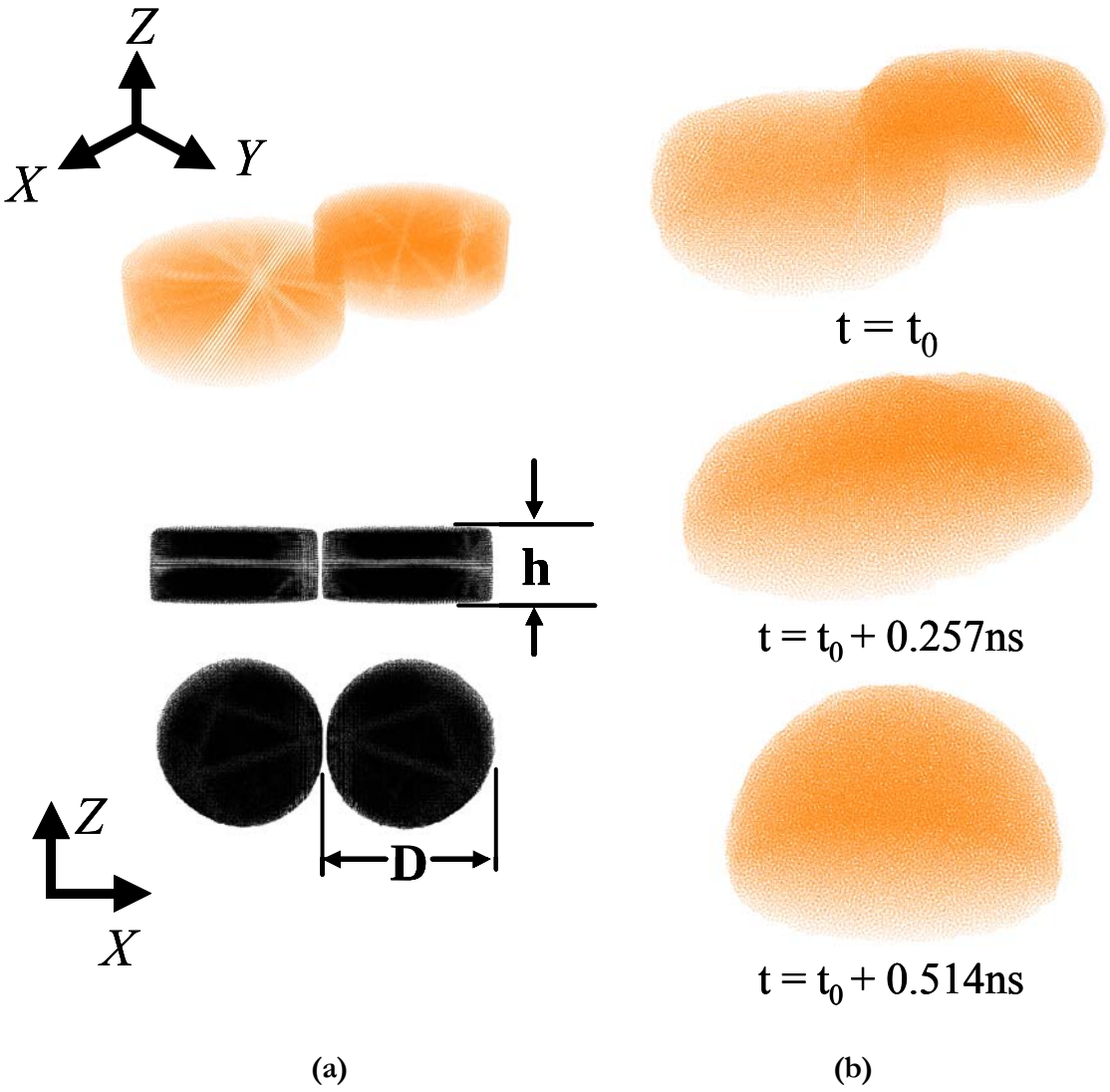

Fig. 3. 5 Initial configuration of the Molecular Dynamics simulation (a). Two gold disks (*D*=15nm) are chopped out of single crystal and placed on a smooth surface. (b) Snapshots of the dynamic coalescence process of the supported gold nanoparticles under laser irradiation, total atom number *N* is 123,572.

It should be emphasized that the transition points *A* and *C* approach each other with the particle size increasing [Wang *et al.* (2003)]. As a consequence, the transition point *A* disappears and the coalescence is completed almost entirely by the melting transition, *C*, for larger particles (15nm) with the heating rate considered here. It can be postulated that for particles with even larger diameter (100nm, used in the experiments) the melting transition will possibly dominate the coalescence.

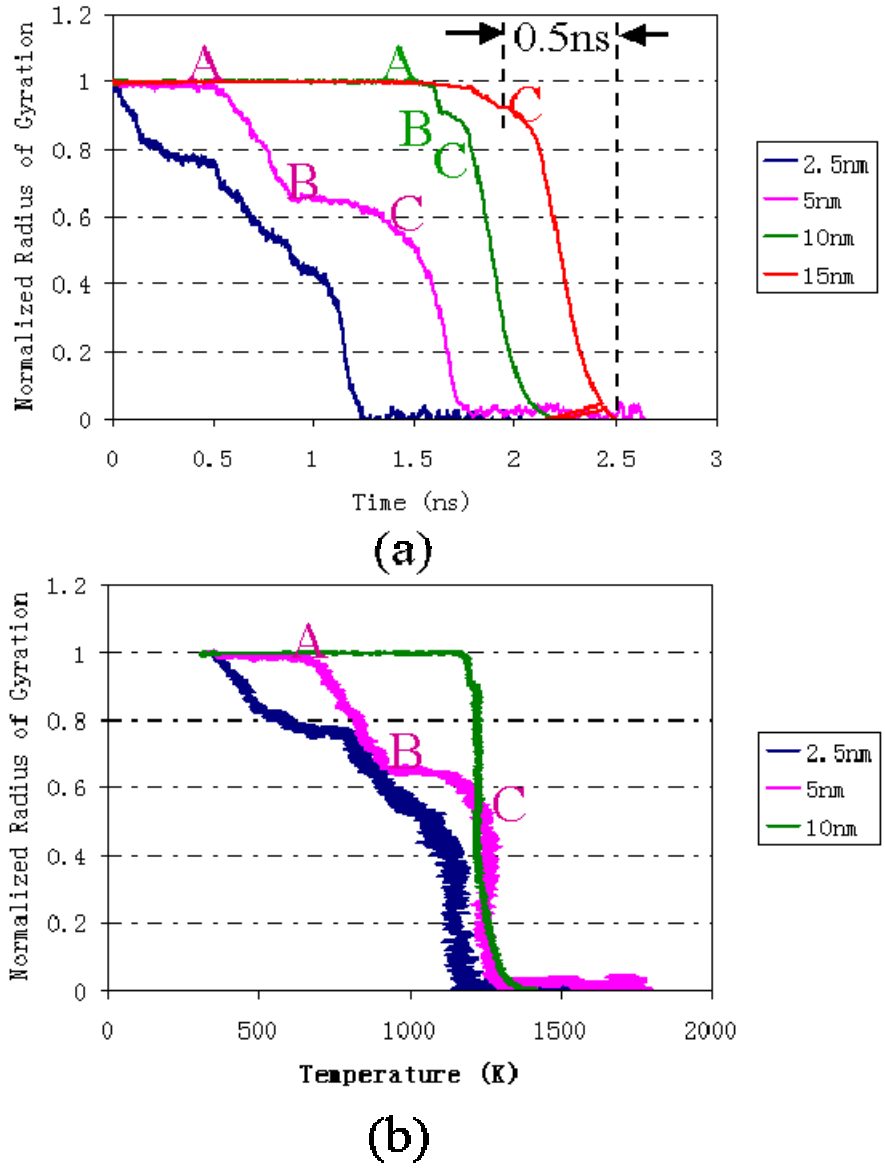

Fig. 3. 6 The evolution of the coalescence with respect to time for particles with different sizes (a) and the temperature dependence of the radius of gyration (b). The heating rate is about $5\times10^{11}K/s$. The letter *A* indicates the onset of the shape transition and *B* indicates the onset of melting.

The coalescence time for the fully melted particles was first calculated. Solid particles were melted by heating up to 1400K. Coalescence was then allowed between two melted particles. It can be clearly seen the coalescence time is linearly proportional to the particle diameter, as indicated in Fig. 3.7. This behavior agrees with the following equation for the coalescence time [Hawa *et al.* (2005), Frenkel *et al.* (1945)]:

$$\tau = \frac{\eta D}{\alpha} \tag{3-3}$$

where η is the viscosity and α is the surface tension. In order to extrapolate the coalescence time for two nanodisks on substrate upon laser heating, the coalescence time for 15nm particles during laser heating estimated from Fig. 3.6a to be ~0.5ns is used. Assuming the scaling given by (3-3) and extrapolating, the time for the 100nm particle is estimated at ~3.3ns. This is shorter than the coalescence time measured from experiment (first transition in Fig. 3.3a, ~6ns). This result should not be too surprising since in this study a) an array of particles is monitored and time has been averaged over the assembly. The measured value is actually the statically average value among all the particles within the probing beam, which is considered to be slightly different from predicted value for individual particle due to the non-uniformity of the laser intensity and particle morphology variations; b) the estimated heating rate in the experiment is lower than that used in MD simulation, and a slower heating rate could slow down the coalescence process. It is known that the coalescence time is strongly dependent on temperature – the linear relation ($\propto d$, Eq. 3-3) holds only for high temperature and liquid-like transformation while for colder particles solid-like behavior ($\propto d^3$) is anticipated [Zachariah *et al.* (1999)]. Furthermore, a regime corresponding to particle solidification/melting transition where the coalescence time longer than liquid-like cluster can be expected [Zachariah *et al.* (1999)]. All these could be mechanisms involved in the observed longer coalescence process. Lastly, the particle-substrate adhesion might also affect the coalescence time. A separate test simulation has been conducted to confirm reduction in coalescence time using a weak particle-substrate interaction (not presented here).

Despite all these factors, the reasonable agreement between experiment and simulation suggests that melting is the major mechanism involved in nanosecond laser induced coalescence of supported 100nm nanoparticles and the characteristic time of the coalescence of should be at least a few nanoseconds. This result is in line with the previous work reported by Habenicht [Habenicht *et al.* (2005)] where the characteristic coalescence time of differently shaped Au structure was found to be 10ns. In contrast to another previously reported 30ps characteristic time of nanorod-to-nanodot transformation occurring in a suspension by laser induced melting [Link *et al.* (1999)], the time obtained here is substantially longer. It is believed that the major difference originates from the much longer laser pulse duration, larger particle sizes used and the effects of the substrate.

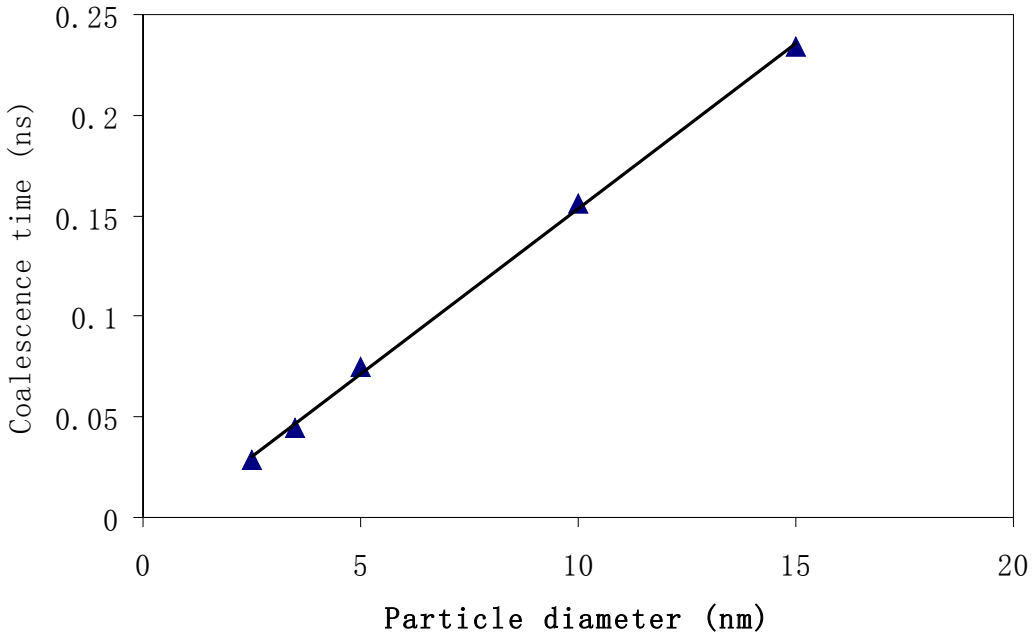

Fig. 3. 7 The dependence of coalescence time on particle size.

3.4 Conclusions.

In summary, the transient characteristic of the nanosecond laser induced coalescence of supported gold nanoparticles is measured by in-situ monitoring the characteristic plasmon resonance of particles with different necking structure. The coalescence time for melted particles is measured to be ~6ns. Molecular Dynamic simulation has been conducted to reasonably predict the characteristic time and explain the transformation mechanisms. An improvement of the current experiment would be underway by using near-field optical microscopy (*NSOM*) probe to measure the behavior of single particle pair. Slower necking evolution, driven by solid diffusion instead of viscous flow that accompanies melting may be investigated by applying lower laser energy densities.

CHAPTER 4

MELT-MEDIATED LASER ANNEALING OF ZNO NANOPARTICLE FOR THIN FILM TRANSISTORS

Nanoparticle solutions are considered promising for realizing low cost printable high performance flexible electronics. In this work, excimer laser annealing (ELA) was employed to induce melting of solution-deposited ZnO nanoparticles and form electrically conductive porous films. The properties of the films were characterized by scanning electron microscopy, high-resolution TEM, DC conductance, and photoluminescence measurements. Thin-film field effect transistors have been fabricated by ELA without the use of conventional vacuum or any high temperature thermal annealing processes. The transistors show n-type accumulation mode behavior with mobility greater than $0.1 cm^2/V\text{-}s$ and current on/off ratios of more than 10^4. Optimization and control of the laser processing parameters minimized thermal impact on the substrate. This technique can be beneficial in the fabrication of metal oxide based electronics on heat sensitive flexible plastic substrates using low-cost, large-area solution processing combined with direct printing techniques.

4.1 Introduction

Due to its wide bandgap and large piezoelectric constant, zinc oxide has drawn attention for its potential applications in a broad range of fields such as room temperature UV lasing [Sun *et al.* (2003)], transparent conducting electrodes [Minami *et al.* (2005)], gas sensors [Ding *et al.* (2005)], solar cells [Law *et al.* (2005)] and surface-acoustic wave devices [Chen *et al.* (2005)]. There have been a number of recent reports on field effect transistors (FETs) using ZnO as the active channel layer [Carcia *et al.* (2003), Hoffman *et al.* (2003), Nishii *et al.* (2003)]. These transistors have high visual transparency, electrical mobility and are stable in air. ZnO deposition at room temperature over large areas was reported [Carcia *et al.* (2003), Fortunato *et al.* (2004), Fortunato *et al.* (2005)][6,9,10] with mobility between 0.01 and 25 cm^2/V-s and an on/off ratio from 10^3 to 10^7. This suggests compatibility with flexible polymer substrates. However, most such ZnO films have been formed by vacuum deposition methods: sputtering, RF sputtering or pulsed-laser deposition [Carcia *et al.* (2003), Hoffman *et al.* (2003), Nishii *et al.* (2003)]. As an alternative cost-effective ZnO deposition method, solution deposited ZnO FETs have been demonstrated recently without using vacuum processes [Ohya *et al.* (2001), Norris *et al.* (2003), Volkman *et al.* (2004)]. However, the reported deposition methods at some point require high temperature annealing processes that are not compatible with flexible polymer substrates. Chemical solution methods, such as sol-gel [Ohya *et al.* (2003)], need annealing steps above 600ºC. Simple solution processing of ZnO nanoparticles (NPs) reported to date such as spin coating, dip coating, or ink jet printing [Norris *et al.* (2003), Volkman *et al.* (2003)] also involve a high temperature post-deposition thermal annealing/sintering step (>300ºC), making these processes incompatible with plastic substrates. The use of a pulsed laser is therefore more advantageous for annealing because laser heating is highly local and very rapid. Excimer Laser Annealing (ELA) has previously been used in place of thermal annealing of thin films [Smith *et al.* (1997)] and nanowires [Misra *et al.* (2007)] to provide compatibility with heat sensitive materials. In this work, we demonstrate solution deposited and excimer laser annealed ZnO NPs as an active channel layer to obtain ZnO NP FETs without using any vacuum or high temperature thermal annealing processes.

4.2 Experimental Method.

The ZnO NP solution was prepared by dispersing ZnO nanopowders (<100 nm, Sigma Aldrich) in ethanol (3.5%w.t.). The ZnO NPs dispersion was sonicated for 1 hour before using. A drop (0.7 μL) of ZnO dispersion was applied to the substrate, and capillary spreading formed a uniform ZnO NP film. The ZnO NP film can also be obtained by spin coating. For spin coating, ethylene glycol (EG) should be added (EG vs. Ethanol = 1:10) to adjust the evaporation rate in order to obtain uniform NP films. A krypton fluoride (KrF) excimer laser (wavelength: 248 nm, pulse width (full width at half maximum: 20 ns) was used to anneal the ZnO NPs. A large-area, uniform, top-flat beam profile of 11 × 11 mm^2 was obtained by using a fly's eye homogenizer to ensure uniform laser annealing. Scanning electron microscopy (SEM) and high resolution transmission electron microscopy (HRTEM) were employed to examine the structural changes. A DC conductance measurement was performed to characterize the electrical properties. To examine the optical properties, photoluminescence (PL) measurements were performed. The PL system uses a SPEX 1404 0.85 m double spectrometer and a room temperature photomultiplier tube detector. The excitation source is the 325 nm line of a HeCd laser. Measurements were performed at room temperature in the backscattering geometry. To fabricate thin-film transistors, ZnO NP solution was applied on pre-patterned metal contacts followed by laser annealing. Figure 4.1 shows a schematic of the laser annealing process and a thin-film FET structure. The ZnO thin-film

FETs have a typical bottom gate/bottom contact transistor configuration with a highly doped n-type silicon wafer as the back gate and a 100 nm thick SiO_2 layer as the gate dielectric. Gold source and drain electrodes were defined by a standard lift-off technique. The channel length (L) was varied from 2 μm to 20 μm and the channel width (W) was fixed at 160 μm. The absorption efficiency can be calculated from the ZnO complex refractive index (**n** = 1.8 + 0.43i at 248 nm) [Washington *et al.* (2003)] for bulk material. The absorption efficiency of two ZnO nanoparticles (80 nm diameter) was calculated by discrete dipole approximation to be in the range of 0.95-1.2 depending on inter-particle spacing. This signifies that the particle density needs to be optimized in order to maximize laser energy coupling.

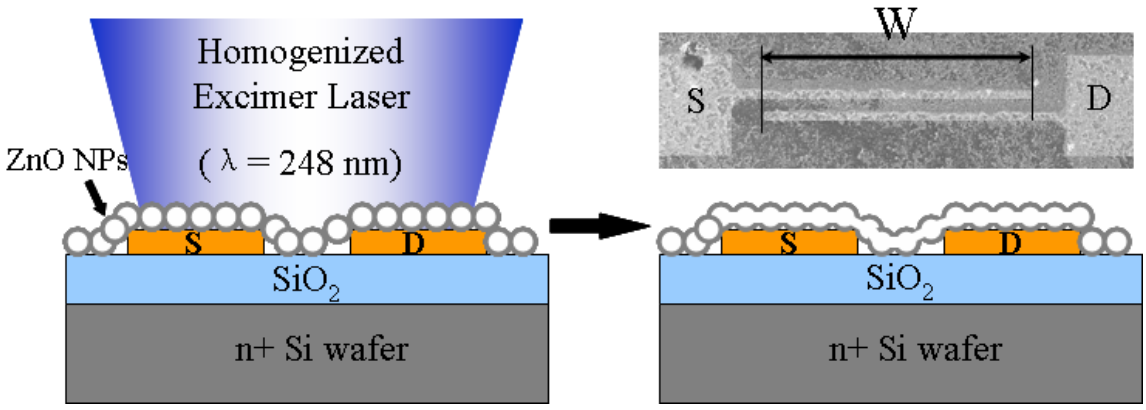

Fig. 4. 1 Schematic side view of the excimer laser annealing process and the ZnO NP FET structure. "S" and "D" indicate source and drain electrodes respectively. Right top inset is the top view SEM image of transistor electrodes with a layer of deposited ZnO NPs. Inset arrow corresponds to 160μm.

4.3 Results and Discussions.

Excimer laser annealing induces structural, electrical and optical property changes in ZnO NP films. Figure 4.2(a) shows the SEM images of single laser pulse annealed microstructures at three different laser fluences (100, 130, 160 mJ/cm^2 from left to right). At low laser fluences (≤130mJ/cm^2), pulsed-laser annealing kept intact the structural properties of nanostructured films. At the fluence of 160 mJ/cm^2, large interconnected grains surrounded by voids were formed after annealing. It has been reported that excimer laser fluences larger than 130mJ/cm^2 can induce melting of ZnO nanoparticles [Ozerov *et al.* (2004)]. The fact that laser heating of NP films up to melting strongly changes microstructures is confirmed from the observations by TEM. Figure 4.2(b) shows the TEM image of NP films after annealing with 160mJ/cm^2. The discretely facetted nanocrystals were transformed into rounded and smooth agglomerations after annealing. Moreover, the grain boundaries of the crystallites within agglomerations can be clearly seen in HRTEM image (Fig. 4.2(c)). The polycrystalline structure, further confirmed by electron diffraction pattern from marked region, should be expected after *ns* laser induced melting and subsequent resolidification. Based on our previous *in-situ* measurement of resolidification/cooling time for supported NPs (~tens of *ns*) [Pan *et al.* (2008)] and reported measurements for suspended NPs (5*ns* to 1μs) [Plech *et al.* (2004)], the quenching rate can be estimated to be lower than

10^{11}K/s, insufficient to obtain amorphous structures. For DC conductance measurement, Al ohmic contacts were made to both as-deposited NP and laser annealed porous films. Figure 4.3(a) shows the room temperature dark *I-V* characteristics of the Al contacts at different laser fluences. Measurements showed the resistance between 1.4cm spaced contacts was determined to be 3.4 x 10^4 MΩ for a film without laser annealing, 171 MΩ for one annealed at 140 mJ/cm^2, and 78 MΩfor one annealed at 216 mJ/cm^2. The resistance was reduced by three orders of magnitude by laser annealing and linear *I-V* behavior was exhibited in all samples. Figure 4.3(b) shows the room-temperature normalized PL (I/I_{UV}) spectra of ZnO samples as a function of wavelength for solution-deposited films with and without laser annealing. Three major emission bands can be seen: UV near-band edge emission (381nm), and defect-related violet (420nm) and green (500nm) emissions. At a laser fluence of 90mJ/cm^2, below the melting threshold, it is found that UV emission increases as exhibited by a reduction of both defect-related emissions in the normalized PL (Fig.4.3b). Further increasing of laser fluence reduces the violet emission until a substantial level of melting is seen at a laser fluence of 160mJ/cm^2. On the other hand, the green emission band located at 500nm, commonly attributed to oxygen vacancies, [Vanheusden *et al.* (1996)] is found to increase with laser annealing. This is due to the fact that the high photon energy of the excimer laser can break chemical bonds, create oxygen vacancies and remove excess oxygen [Ozerov *et al.* (2003)].

The inset in Figure 4.4(a) shows a SEM image of the ZnO NP FET channel with laser annealing. The SEM image reveals no observable damage to substrate and electrodes after laser annealing. The particles are distributed homogeneously with a high degree of porosity that is consistent with a high surface area structure between electrodes. The electrical characteristics of individual transistors were measured using an Agilent 4155A semiconductor analyzer in a dark Faraday cage. Figure 4.4(a) shows the output characteristics of a laser annealed ZnO FETs with a *W/L* of 160/12 μm. The source-drain voltage (V_{DS}) was scanned from 0 to 2V while the gate voltage (V_{GS}) was fixed at -15V (circles), 0V (crosses), 15V (squares), 30V (triangles). The shown maximum V_{DS} has been limited to 2V because a strong shift of V_T to negative values and punch-through could be observed when a higher V_{DS} was used. This is due to the fact that the annealed film is relatively thick and the laser processing is limited to the film surface region, then the region close to the gate is less laser-processed and gate modulation is less efficient. Using smaller NPs and forming optically and physically thinner film can remedy this issue. Therefore device operation is shown only in the linear region here. Figure 4.4(b) shows the corresponding transfer characteristics. Gate voltage was scanned from -30 to +30V while the drain voltage was fixed at 1V (triangles), 2V (squares). The transfer characteristics graph indicates that the transistor operates in an n-channel accumulation mode. A semi-log plot of I_D vs V_G (not shown here) also shows an on/off current ratio of >10^4 with a very low off current level (~10 pA), a sub-threshold slope of 5V/decade, and a threshold voltage (V_T) of 5 V. The transconductance (g_m) is 50 nS as shown in Figure 4.4 (b) inset graph. The effective field effect mobility (μ) of the ZnO nanoparticle porous film FET can be derived using the following relationship for the continuous thin film

$$\mu = \frac{Lg_m}{WC_{ox}V_{DS}} \tag{4-1}$$

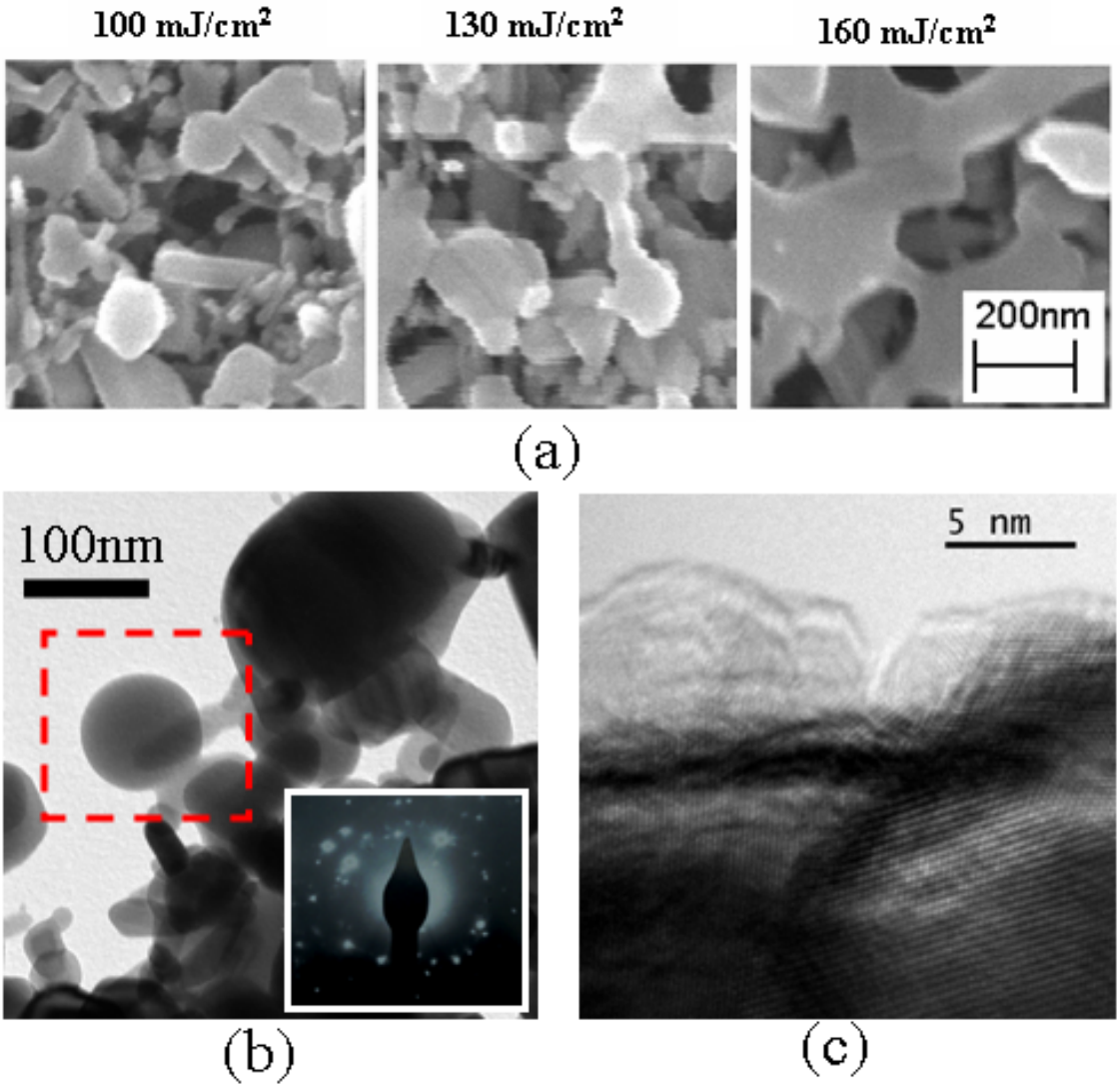

Fig. 4. 2 (a) SEM pictures of nanostructure changes of ZnO NP film after irradiation with different excimer laser fluences. (b) TEM images of ZnO NP film after excimer laser irradiation. Insert shows the diffraction pattern from marked region. (c) The HRTEM image reveals the poly-crystalline structure of the laser processed ZnO NP film.

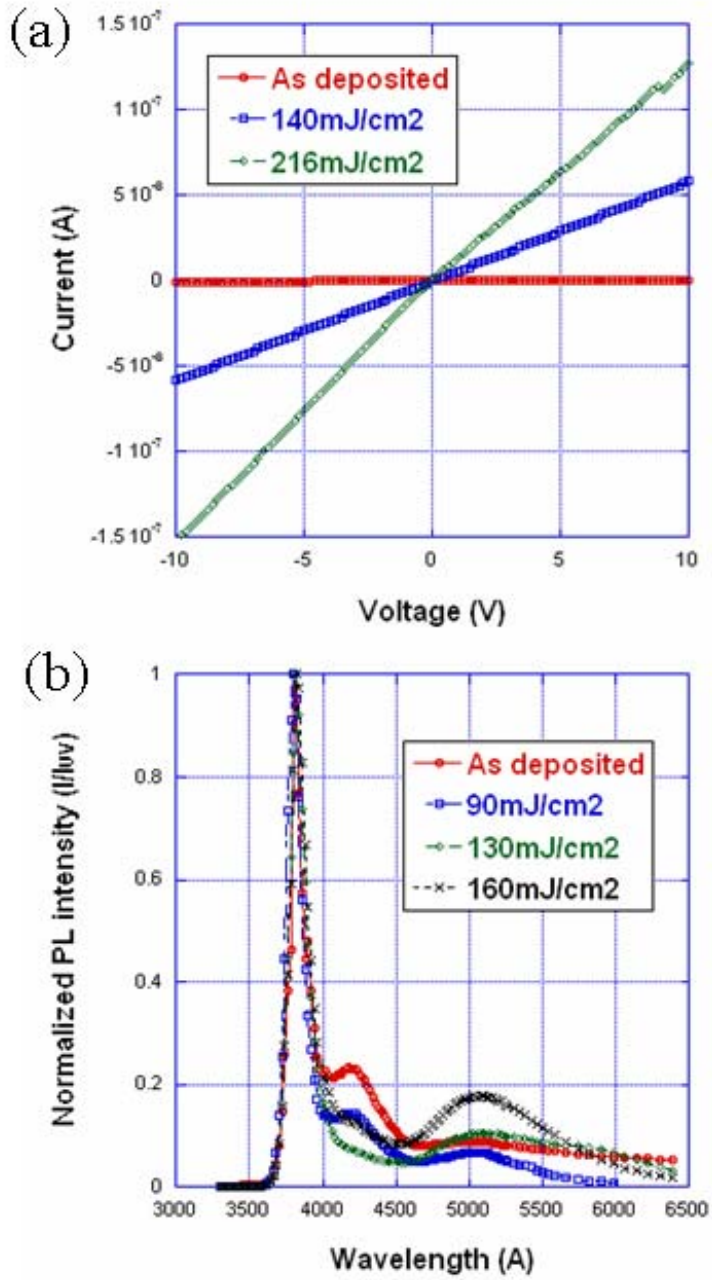

Fig. 4. 3 (a) Room temperature *I-V* data for an Al Ohmic contact to ZnO NP film after laser processing at different fluences. (b) Room temperature PL spectra with and without laser annealing.

where L, W, and C_{ox} indicate the channel length, channel width, and the capacitance, respectively. We point out that due to the geometry of the porous film and the absence of a simple estimate of capacitance, we have used an effective mobility assuming complete coverage. The effective mobility estimated in this manner is a lower-bound value. The effective field effect mobility extracted using this equation and the measured dimensions is estimated to be 0.106 cm^2/V-s. The laser annealed ZnO FETs show three to four orders of magnitude higher mobility and on/off ratio compared with unannealed devices. In addition, a reliable electrical contact can be expected following direct annealing of the semiconductor material on the electrodes. It should be noted that the mobility of the laser annealed ZnO measured here is comparable to the highest value (0.1-0.2 cm^2/V-s) reported for solution deposited and thermally annealed (at a temperature of ~700ºC) ZnO NP n-type FETs [Norris *et al.* (2003)]. Laser annealing of ZnO NPs enabled a reasonably good mobility without high temperature thermal annealing of the selected area. However, this value is still lower than the published ZnO thin film mobility (~10cm^2/V-s) for sputtered or pulsed-laser deposited ZnO thin film transistor [Nishii *et al.* (2003)]. Possible reasons for this could be due to porous structure, less actual coverage ratio, increased carrier scattering by significant film porosity, large surface area and large impurity concentrations in the film. Also note that the gate leakage current reported here is very low (~10 nA) compared to the previously reported high gate leakage current since ZnO attacks the insulating SiO_2 layer during the high temperature annealing (>600ºC) [Ohya *et al.* (2001)]. The low gate leakage obtained in this work signifies that ELA minimized thermal effects on SiO_2/n+ Si substrate while providing sufficient energy to induce particle annealing and coalescence.

4.4 Conclusion.

In conclusion, excimer laser annealing of solution-deposited ZnO NPs for high performance n-type FETs fabrication was demonstrated without using any vacuum process or high temperature thermal annealing process. A single laser pulse of 160 mJ/cm^2 fluence could transform solution deposited discrete ZnO NPs into interconnected porous structures, thus enhancing the electrical mobility. The remarkable improvement of the FET performance with low gate leakage current and intact underlying electrodes after laser annealing signifies that current process can be used potentially for low temperature, low cost flexible electronics on heat sensitive polymer substrates. This process can be easily integrated with recently developed metal NP inkjet printing and selective laser sintering [Ko *et al.* (2007), Ko *et al.* (2007), Ko *et al.* (2007)] or metal NP direct nanoimprinting [Ko *et al.* (2007)] for low temperature, high resolution FET electrode fabrication. Current solution deposited and laser annealed ZnO NP FETs can replace low mobility semiconducting polymer to achieve cost effective, all printing, low temperature, lithography free and high performance electronics on polymer substrates.

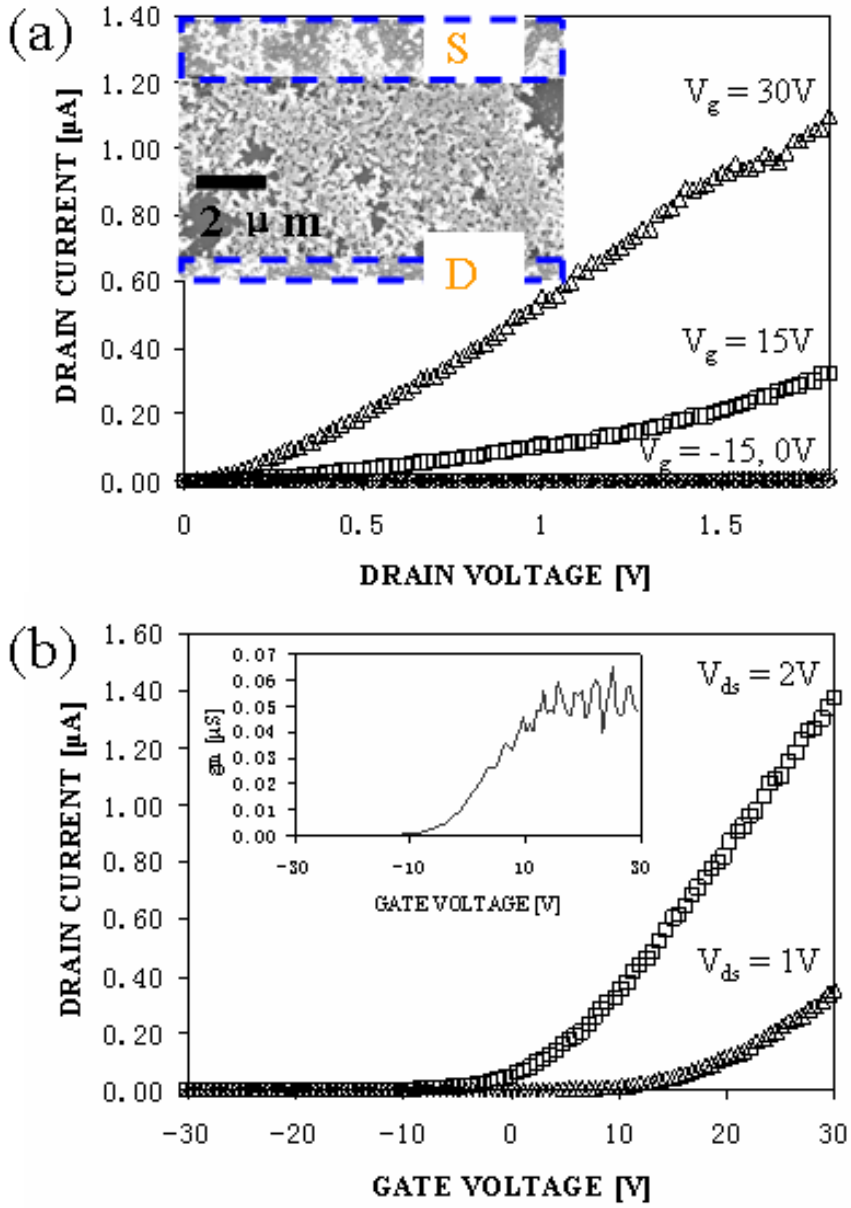

Fig. 4. 4 (a) Output characteristics of an excimer laser annealed ZnO NP FET with W/L=160/12 μm. Inset shows SEM image of the channel region covered by laser annealed NPs. Drain voltage was scanned from 0 to 2V while gate voltage was fixed at -15V (circle), 0V (cross), 15V (square), 30V (triangle). (b) Transfer characteristics of the device. Gate voltage was scanned from -30 to +30V while the drain voltage was fixed at 1V (triangle), 2V (square). Inset graph is a transconductance curve of the device when the drain voltage was 2V. The saturation value is 50nS.

CHAPTER 5

LASER ANNEALING OF TIO_2 NANOPARTICLES FOR DYE SENSITIZED SOLAR CELLS

We report a rapid and low temperature process for fabricating TiO_2 electrodes for dye-sensitized solar cells (DSSCs) on glass and plastics by *in-tandem* spray deposition and laser annealing. A homogenized KrF excimer laser beam (248nm) was used to layer-by-layer anneal spray deposited TiO_2 nanoparticles. The produced TiO_2 film is crack free and contains small particles (30nm) mixed with different fractions of larger particles (100-200nm) controlled by the applied laser fluence. Laser annealed double-layered structure is demonstrated for both doctor-blade deposited and spray-deposited electrodes and performance enhancement can be observed. The enhancement could come from the laser induced optical and electrical properties changes. The highest demonstrated all-laser-annealed cells utilizing Ruthenium dye and liquid electrolyte showed power conversion efficiency of ~3.8% under simulated illumination of 100mW/cm^2.

5.1 Introduction

Dye-sensitized solar cells (DSSCs) are a potential low-cost alternative to conventional solar cells owing to potentially high efficiency (~10%) and low cost fabrication processes [O'Regan *et al.* (1991), Gratzel *et al.* (2001)]. Conventionally, nanoporous TiO_2 photoanode is fabricated through blading or screen printing of TiO_2 slurry followed by high temperature (450ºC) thermal sintering. TiO_2 films are also produced by using spray pyrolysis [Okuya *et al.* (2004)] and polymer pyrolysis [Stathatos *et al.* (2007)]. However, these processes involve high temperature. Lowering the processing temperature is required for cell fabrication on flexible substrates. However, the material produced by simply sintering at lower temperature cannot compete in regard to the electrical properties with standard high-temperature process [Pichot *et al.* (2000)]. Other low temperature processes and corresponding reported efficiencies under illumination of $100mW/cm^2$ include compression (3%) [Lindstrom *et al.* (2001), Lindstrom *et al.* (2001)], hydrothermal crystallization (4.2%) [Zhang *et al.* (2003)], CVD with UV treatment (3.8%) [Murakami *et al.* (2003)], microwave irradiation (2.3%) [Hart *et al.* (2007)], and electron bombardment (2.8%) [Kado *et al.* (2003)].

In present study, we report a low temperature method that can produce electrodes with distinct particle size and composite layers via layer-by-layer (LBL) laser annealing. Laser processing of DSSC has been reported [Kim *et al.* (2007), Kim *et al.* (2007)]. However, reported cell efficiency is not satisfactory (1.8%) unless a high temperature sintering step is added (4.3%). Recently, we demonstrated the excimer laser annealing (ELA) of metal oxide (ZnO) nanoparticles to improve the electrical properties in producing FETs [Pan *et al.* (2009)]. Here, ELA is coordinated with spray deposition to realize DSSC on glass and plastic substrates with performance comparable to high temperature annealed cells. The laser annealing of doctor-blade deposited TiO_2 is also studied for examination of laser induced effects.

5.2 Experimental Method.

The TiO_2 nanoparticles were deposited and simultaneously annealed by laser on SnO_2 coated glass (Hartford Inc.) and ITO coated PET (Delta Technologies) as shown in Figure 5.1a. The nanoparticle suspension was prepared by mixing commercially available TiO_2 nanopowders (Degussa) in solvent containing water, nitric acid, Triton, ethanol and methanol. A collision nebulizer (Ted Pella, Inc.) was used to transfer the suspension into aerosols and the carrier gas, e.g. nitrogen, was regulated by a flow meter (Omega). The aerosol jet impinged on the receiving substrate at an angle of incidence of 45º. A krypton fluoride (KrF) excimer laser (wavelength: 248 nm, pulse width 20 ns) was used for annealing. A large-area, uniform, top-flat beam profile can be obtained by using a fly's eye homogenizer to ensure uniform laser annealing. The deposition and annealing were performed inside a sealed chamber. By regulating carrier gas flow rate, an aerosolization rate of ~0.8mL/min was maintained. The overall thickness of the TiO_2 film monotonically increases with the aerosolized volume as shown in Figure 5.1b. Figure 5.1c shows the obtained porous, macroscopically uniform and crack-free film. The surface profile (5.1d) indicates that the film is non-uniform microscopically and consists of agglomerates with lateral dimension from few μm up to 100μm. Nanoparticles carried within the spray droplets tend to form agglomerates if the evaporation of the solvent upon intercepting the substrate is fast compared to the deposition rate.

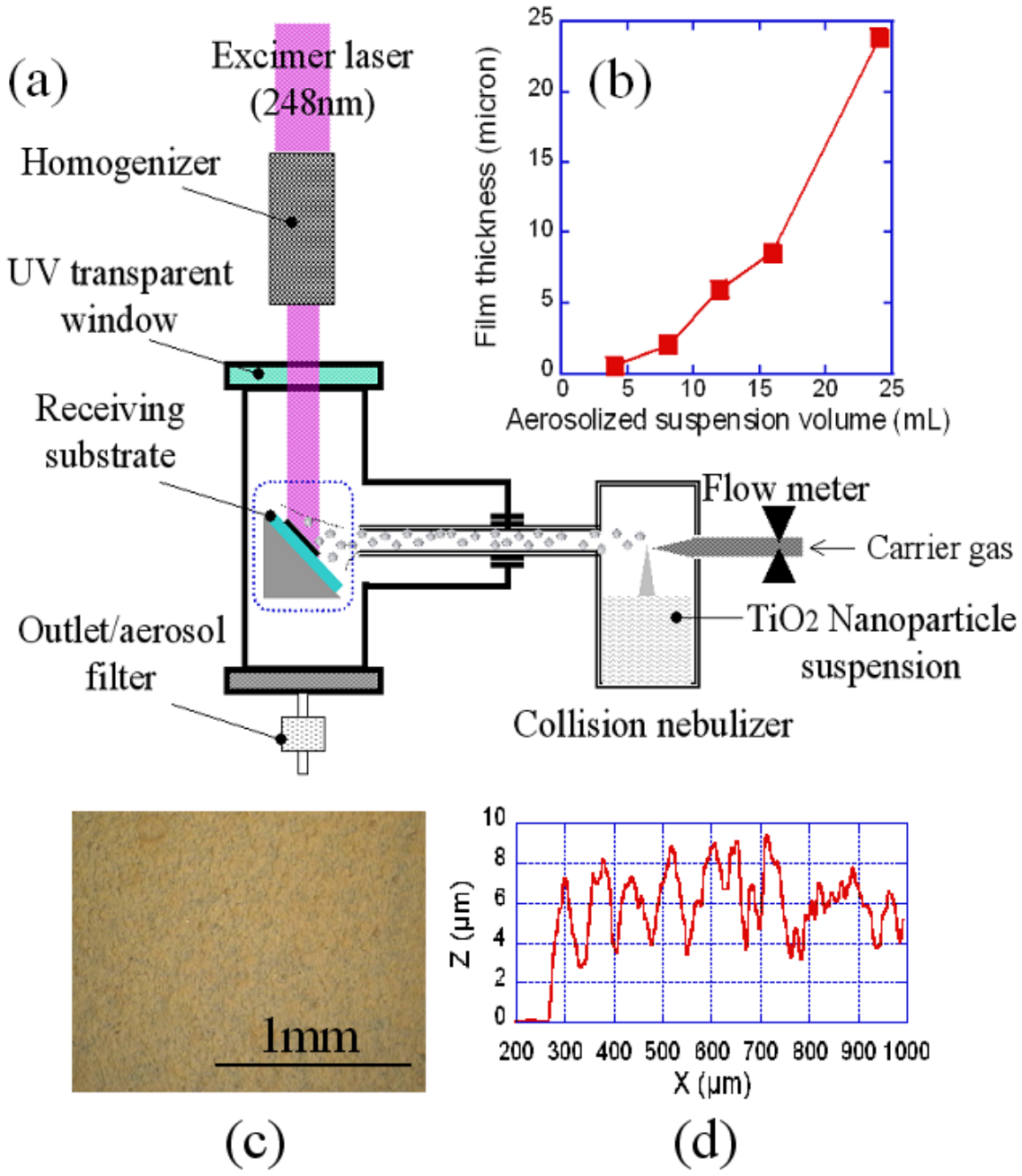

Fig. 5. 1 (a) The schematic of *in-tandem* spray deposition and laser annealing setup. (b) The relation between aerosolized nanoparticle suspension volume with deposited film thickness. (c) Optical dark field microscopy image of spray deposited and laser annealed film. (d) Film surface profile measured by profilometer.

The annealed film area was 0.35 cm^2. The films were dipped overnight (~15h) into a sensitizing 0.3mM dye solution Ruthenium 535-bisTBA (Solaronix) in ethanol at room temperature. The counter electrodes were made by doctor-blading platinum catalyst (Solaronix) on Glass/SnO_2 and sintered for 400˚C for obtaining a transparent Pt layer. The Pt electrode and the dye-loaded TiO_2 electrode were sealed together with a 25-μm-thick Surlyn spacer. The I^-_3/I^- redox electrolyte (Iodolyte AN-50, Solaronix) was introduced into the gap formed by the two electrodes and observed to thoroughly wet the dye-covered TiO_2 electrode via capillary action. The current density versus voltage (*J-V*) characteristics of the cells was measured under AM 1.5 100mW/cm^2 illumination from a solar simulator immediately after cell assembly by a semiconductor analyzer (Agilent 4155A).

Besides the spray deposition method, doctor-blade deposition is also used for detailed study of laser induced structure and properties changes and their effects on solar cell performance. For doctor blading, suspensions with two concentrations (0.8g and 1.5g TiO_2 nanoparticles in 4ml nitric acid with PH 3-4) were prepared and deposited on SnO_2 coated glass by doctor blading. The TiO_2 film is subjected to excimer laser annealing, thermal annealing and optional UV-ozone cleaning steps. The rest of cell fabrication processes and cell testing procedure are identical to that described above.

5.3 Results and Discussions

5.3.1 Laser in-tandem annealing of spray on nanoparticles

Figure 5.2 shows SEM micrographs and the x-ray diffraction (XRD) patterns of laser annealed TiO_2 nanoparticles on glass under different laser fluences (with 10Hz repetition rate). Under the fluence of 33.7 mJ/cm^2, the particle size in the TiO_2 film remains largely unchanged (~30nm). The XRD pattern shows that the peak intensity ratio between anatase and rutile decreases slightly (from 3.27 to 2.88) indicating a small fraction of anatase phase is transformed into rutile. Increasing the laser fluence results in the appearance of larger nanoparticle (100-200nm) due to laser induced melting and coalescence. Correspondingly, the anatase to rutile intensity ratio reduces further to 1.6 with 80.9 mJ/cm^2 implying further increase of rutile phase. No changes can be found in full width at half-maximum (fwhm) of rutile peak upon laser annealing.

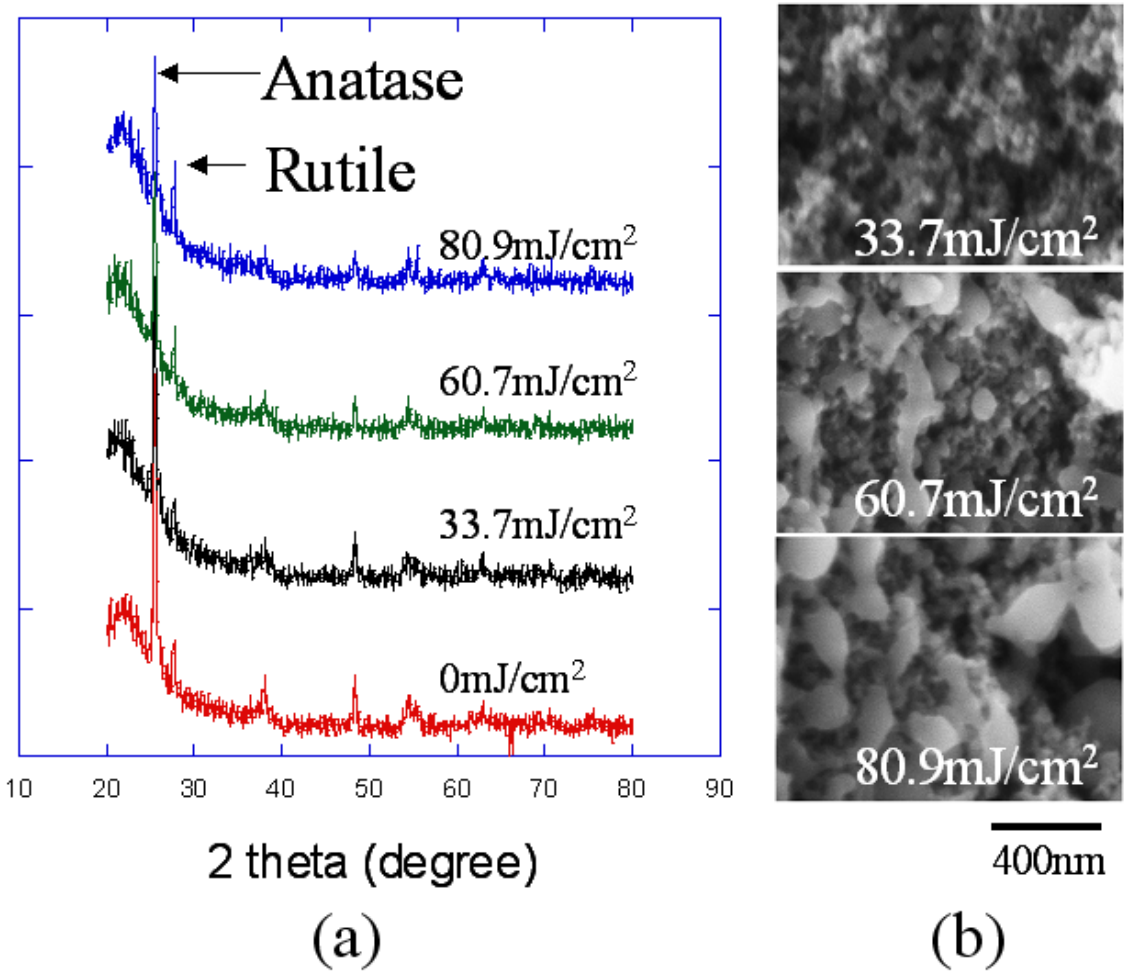

Fig. 5. 2 (a) The XRD pattern and (b) the SEM micrographs of nanoporous structures of TiO_2 films on glass obtained by laser annealing with different levels of fluences.

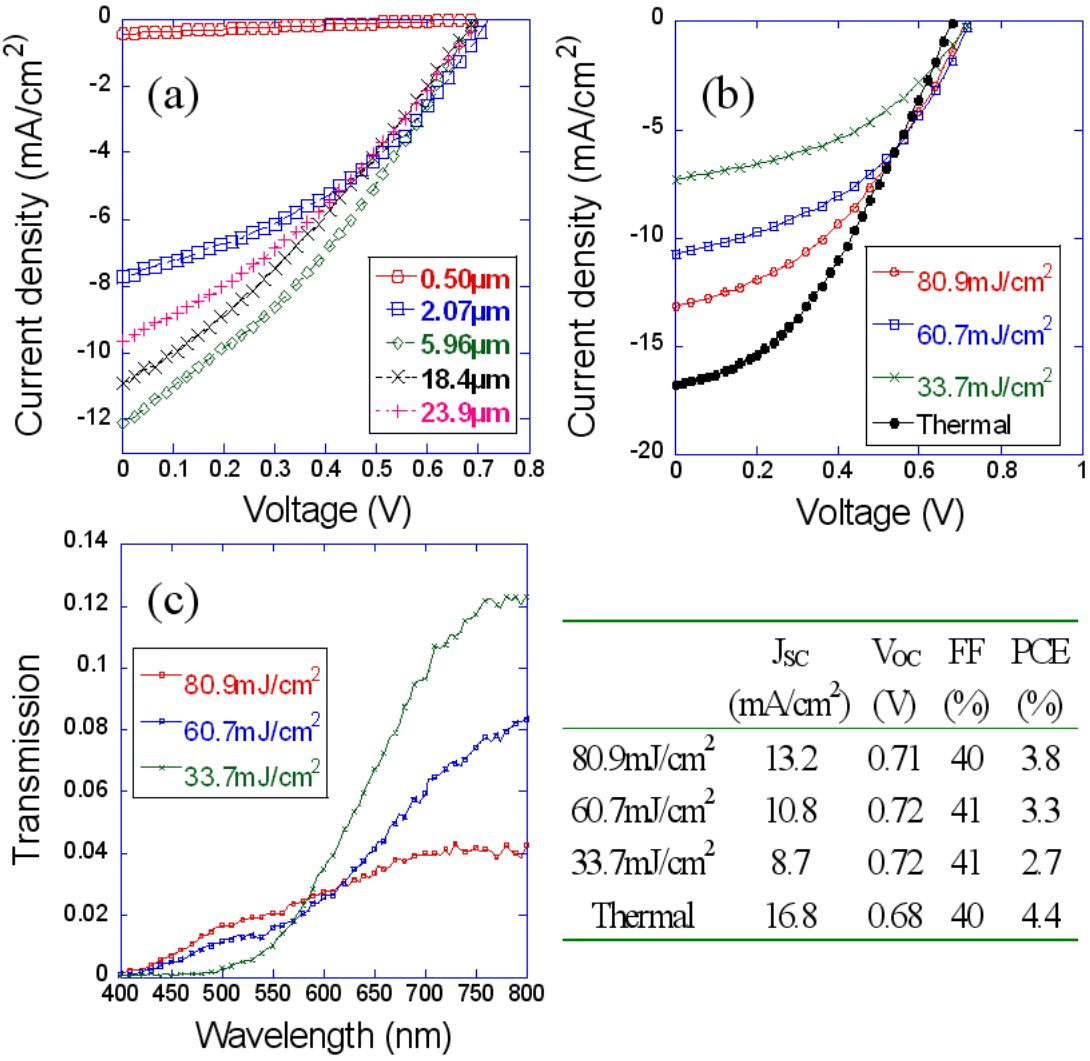

	Jsc (mA/cm^2)	Voc (V)	FF (%)	PCE (%)
80.9mJ/cm^2	13.2	0.71	40	3.8
60.7mJ/cm^2	10.8	0.72	41	3.3
33.7mJ/cm^2	8.7	0.72	41	2.7
Thermal	16.8	0.68	40	4.4

Fig. 5. 3 (a) The *J-V* curves of cells on glass with various TiO_2 electrode thicknesses. (b) The *J-V* curves of cells on glass annealed by different laser energy as well as the reference cell by standard thermal annealing. The key parameters are summarized in the table (c) The transmission spectra of TiO_2 films.

Figure 5.3a shows the *J-V* characteristics for several cells annealed with 80.9 mJ/cm^2 containing varying thicknesses on glass. In these cells, the short circuit current density (J_{sc}) rises to ~12 mA/cm^2 as the TiO_2 thickness is increased to 5.96μm and reduces upon further thickness increasing. The open circuit voltage (V_{oc}) only decreases slightly (3.8%, the difference is within the label size) when the thickness increases from 2.07μm to 5.96μm and remains approximately the same as thickness increases thereafter. The initial increase of J_{sc} can be related to the increased surface area of TiO_2 and the amount of adsorbed dye. As the thickness continues increasing, the number of surface recombination centers is also expected to increase and results in reduction of J_{sc} and V_{oc} [Huang *et al.* (1997), Park *et al.* (2000)].

Figure 5.3b shows the current-voltage (*J-V*) characteristics for DSSCs on glass with varying laser fluences. The TiO_2 film thickness is ~6μm. The short-circuit current (J_{sc}), open-circuit voltage (V_{oc}), FF, and PCE derived from the *J-V* curves for different cells are also presented in the table in Fig.5.3b. From Fig.5.3b, it can be seen that J_{sc} is clearly improved over the cells via use of higher laser fluence (from 8.75mA/cm^2 to 13.2mA/cm^2). The open circuit voltage remains almost unchanged, resulting in overall efficiency increase from 2.7% to 3.8%. Laser annealing could enhance the neck growth between particles and therefore the electron transport as has been suggested in thermal sintering [Nakade *et al.* (2002)]. At the same time, laser annealing generates dense diffusive particles and possibly photoactive sub-bandgap surface states that might promote light harvesting, enhance electron injection efficiency and electron transport [Gregg *et al.* (2003)]. However, the laser annealing reduces dye loading. Figure 5.3c shows the transmission spectra of the dye-sensitized electrode before cell construction. Lower transmission at 800nm can be observed as a result of scattering and the possible appearance of sub-bandgap defects for electrodes processed by higher laser fluence. Considering the transmission offset at 800nm, the transmission at 500nm reveals that 80.9 mJ/cm^2 incurs the lowest dye loading in agreement with the decrease of surface area and defects generation. Even with low dye loading, the cell exhibits better efficiency, suggesting better electrical properties and light harvesting resulting from laser annealing. The details will be discussed in the next section. A reference cell fabricated by doctor-blade deposited of ~15μm TiO_2 nanoparticles followed by standard thermal annealing process at 450°C reveals similar efficiency (4.4%) and fill factor (0.4).

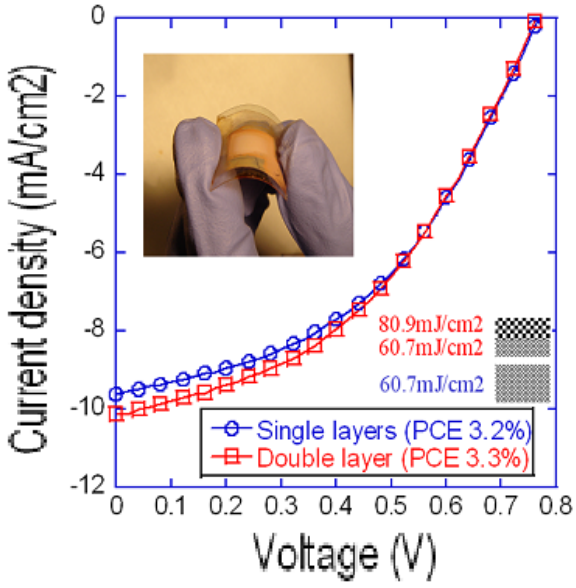

Fig. 5. 4 The *J-V* curves of cells on plastics.

To take advantage of current technique for processing on low temperature substrates, the fabrication of cells on ITO/FET by *in-tandem* spray and laser annealing is also demonstrated. Due to the lower damage threshold on plastics, a laser fluence of 60.7 mJ/cm^2 was used. Considering the laser radiation penetration depth in TiO_2 films, pre-deposited layer >3μm should be enough to prevent substrate damage from laser annealing. Based on this concept, a double-layered structure was also fabricated, whereby laser fluence was increased to 80.9 mJ/cm^2 after formation of a ~3μm

layer as illustrated by the inset in Fig.5.4. With this structure, a slight increase in efficiency from 3.2% to 3.3% was observed.

5.3.2 Laser annealing of doctor-blade deposited nanoparticles

Repetitive laser irradiation on doctor-blade deposited films induces coalescence of nanoparticles, therefore forming dense top layers consisting of larger particles, as shown in Figure 5.5a. The larger particle and laser annealing induced defects will affect the dye loading. The difference in the dye loading can be seen in the Figure 5.6, wherein dye is dissolved into NaOH solution from TiO_2 films with and without laser annealing. The transmission is measured to determine the dissolved dye solution in a transparent cuvette. The transmission evaluated at 650nm converted to dye concentration in the NaOH solution (dye loading) reveals that laser annealed film contains 1.3 times less dye. Even though the dye loading is less, the transmission of dye loaded laser annealed TiO_2 film is lower than that without laser annealing (as separately measured). This could be due to the diffusive top layer and the laser irradiation induced sub-band surface states [Gregg *et al.* (2003)].

To evaluate the effects of laser annealing on cell performance, sample cells are fabricated as shown in Table 5.1. Typical I-V curves are shown in Fig.5.5b. The parameters for laser annealing are ~100 pulses with fluence of 80-90mJ//cm^2. Thermal annealing at 400°C/150°C on hot plate follows the laser annealing step. Additional UV ozone cleaning for 10mins after thermal annealing is needed to remove the oxygen vacancy defects and residual organics.

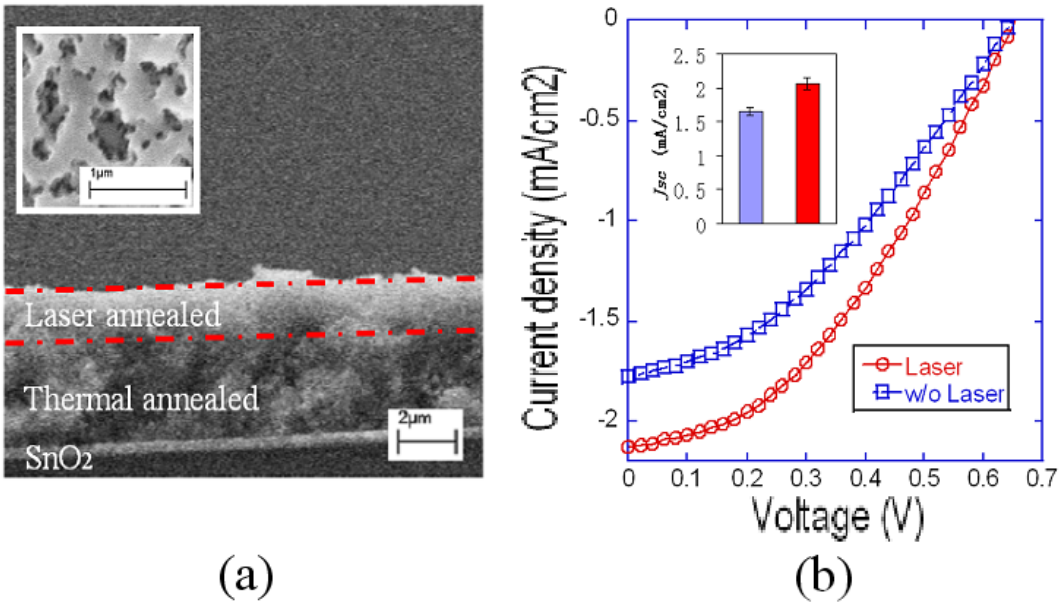

Fig. 5. 5 (a) The cross-sectional and top view (inset) of double-layered structure. (b) The *J-V* curves of the cells with and without laser annealing under illumination of 24 mW/cm^2. The inset shows the comparison of averaged short circuit current.

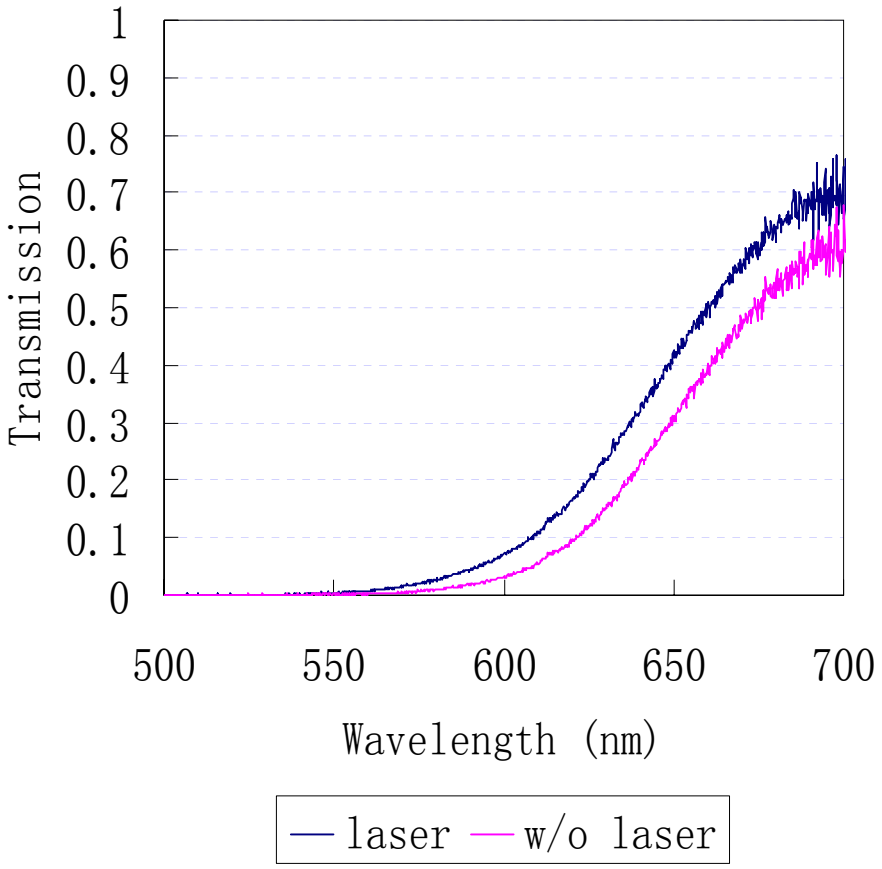

Fig. 5. 6 The transmission of dye detached from TiO_2 film with and without laser annealing.

Sample #	Laser annealing	Thermal annealing (30mins)	Ozone cleaning	TiO_2 film thickness (microns)
A	Yes	400° C	No	~7
B	No	400° C	No	~7
C	Yes	400° C	No	~4
D	No	400° C	No	~4
E	Yes	150° C	No	~7
F	No	150° C	No	~7
G	Yes	150° C	Yes	~7
H	No	150° C	Yes	~7
I	Yes	150° C	No	~4
J	No	150° C	No	~4
K	Yes	150° C	Yes	~4
L	No	150° C	Yes	~4

Table 5. 1 The DSSC processing parameters.

	Short Circuit Current (mA/cm^2)	Short Circuit Current (mA/cm^2)
Sample #	A	B
1	2.08	1.5
2	1.75	1.45
3	1.6	1.46

	Short Circuit Current (mA/cm^2)	Short Circuit Current (mA/cm^2)
Sample #	C	D
1	0.91	0.76
2	0.87	0.78
3	0.77	0.8

	Short Circuit Current (mA/cm^2)	Short Circuit Current (mA/cm^2)
Sample #	E	F
1	0.18	0.2
2	0.189	0.23

	Short Circuit Current (mA/cm^2)	Short Circuit Current (mA/cm^2)
Sample #	I	J
1	0.24	0.259
2	0.2	0.26

	Short Circuit Current (mA/cm^2)	Short Circuit Current (mA/cm^2)
Sample #	G	H
1	0.37	0.31
2	0.37	0.3
3	0.3	0.27

	Short Circuit Current (mA/cm^2)	Short Circuit Current (mA/cm^2)
Sample #	K	L
1	0.46	0.37
2	0.47	0.36
3	0.37	0.34

Table. 5. 2 The short circuit current comparisons for samples under the illumination of 20mW/cm^2.

The short circuit currents measured under the illumination of 20mW/cm^2 are summarized in Table 5.2. It can be seen that for samples with 400^{o}C annealing, the laser annealing step enhances the short circuit currents. One the other hand, for samples subjected to 150^{o}C annealing without ozone cleaning, laser annealing generates lower short circuit currents. The ozone cleaning helps to increase the current for both laser-annealed and non-laser-annealed samples while the more increase in laser annealed can be observed.

It is believed that laser annealing will change the dye loading capability, electrical and optical properties of the TiO_2 film. Typically, excimer laser can drive oxygen gas from the metal oxide target [Doeswijk et al. (2004)]. In present study, it is observed that the white oxide nanoparticle color changed into gray after excimer laser annealing, indicative of a metal-rich layer (Ti^{3+} states). It has been reported that the electrical resistance of the TiO_2 target decreases at least several orders of magnitude after excimer laser processing [Doeswijk *et al.* (2004)]. Surface Ti^{3+} sites may play

an important electron-transfer role -- electrons may travel faster in a surface with defects. However, the cell performance could be compromised by Ti^{3+} or oxygen vacancy defects. It is argued that defects tend to increase the surface recombination rate [Weidmann *et al.* (1999)]. Furthermore, dye molecules preferably attach by chemisorption onto thermodynamically stable Ti^{4+} sites rather than onto Ti^{3+}, because of Ti^{3+} instability. Obviously, adsorbed dye molecules per unit area will be different due to the Ti^{3+} content difference. Laser annealing generates a large amount of Ti^{3+} defects, therefore the dye loading is much less without removing the defects. Hence lower short circuit current can be observed for sample E, I than F, J. The ozone cleaning reduces the amount of Ti^{3+} defects, therefore enhancement can be observed (G, H, K, L vs. E, F, I, J). The removal of Ti^{3+} defects or oxygen vacancy defects can be observed via a change in color (from gray to white) after ozone cleaning. It is interesting to note that the short current increase in laser annealed cells is higher (G, K vs H, L). This could be due to the generation of large amount of sub-band photoactive defects by laser annealing other than Ti^{3+} or oxygen vacancies [Gregg *et al.* (2003)]. The laser annealing generated defects could be beneficial to DSSC performance. Firstly, the defects could alter the conduction band of the nanocrystalline titanium dioxide promoting electrons injection. Secondly, the photoactive surface defects generation could enhance the electron transport while possibly leads to reduced recombination [Gregg *et al.* (2003)]. Besides the laser induced defects, the formation of denser films by laser annealing could also lead to better electron transport and light harvesting.

5.4 Conclusions

In conclusion, a low temperature method for producing crack free composite electrodes by laser annealing is proposed. This technique not only realizes DSSCs on temperature sensitive substrates, but also enables full 3D engineering of nanoporous structures. Laser annealing also gives rise to the changes in optical and electrical properties (optical scattering, defects concentration and electron transport) changes in the TiO_2 film, whereas both positive and negative effects induced by defects deserve further investigation. By employing sources offering larger processing area such as high power industrial lasers or excimer lamp and translation systems, this technique can be adapted to roll-to-roll manufacturing.

.

CHAPTER 6

ELLIPSOMETRIC CHARACTERIZATION OF SILVER NANOPARTICLE THERMAL SINTERING

Low temperature sintering of metal nanoparticle (NP) inks is a promising technique in realizing large area and flexible optic- and electronics. It is demonstrated in the present study that spectroscopic ellipsometry (SE) in the spectral region of 0.75eV-3.5eV can be employed to characterize the sintering process manifested by the evolution of film thickness, effective dielectric function and percolation transition. A two-oscillator model can be used to model the effective dielectric function through the dielectric-to-metallic transition. The oscillator energy shifts towards the lower end and correlates well with the increase of DC conductance as demonstrated by both *in-situ* and *ex-situ* ellipsometric measurements. A simple model based upon 2D *R-L-C* impedance network was successfully adopted to explain experimental results quantitatively.

6.1 Percolation probing and Bruggemann theory

Due to its compatibility with jet printing and low-temperature processing required by flexible substrates, nanoparticle (NP) metal inks present a promising candidate for large-are electronics applications. Generally, thermal sintering is required to achieve the ink's transformation from a layer of densely packed nonconductive NPs into percolating or conductive film. Various devices have been demonstrated using this technique [Ko *et al.* (2007), Ko *et al.* (2007), Ko *et al.* (2007)]. Especially with the aid of laser, micron and sub-micron features can be defined [Ko *et al.* (2007), Ko *et al.* (2007)]. For these applications, it is important to determine the percolation threshold, or more precisely stated, the sintering conditions, i.e. temperature and time, over which the film transitions from insulator to conductor. Controlling the percolation level is shown to be critical for avoiding cracking and detachment from substrate upon the NP sintering [Sivaramakrishnan *et al.* (2007)]. Obtaining desired thickness is generally important in practical applications. Therefore, a non-contact way to probe percolation transition and thickness variation during sintering is desirable. As illustrated in Fig 6.1, we would like to probe the electrical conductivity (DC signal) during the sintering through optical measurement (AC signal). In the present study, we show the feasibility of using visible(VIS)-near IR(NIR) spectroscopic ellipsometry to achieve these goals.

Film under percolation transition has been studied extensively including electroless deposition [Vries *et al.* (2007)], evaporation [Seal *et al.* (2003)], and plasma growth [Oates *et al.* (2005), Oates *et al.* (2004)]. It is generally accepted that these percolating systems involving metal growth can be studied by Bruggemann approximation (BA) [Smith *et al.* (2004)]. The BA model is shown as the following which:

$$f\frac{\varepsilon-\varepsilon_{eff}}{\varepsilon+2\varepsilon_{eff}}+(1-f)\frac{\varepsilon_M-\varepsilon_{eff}}{\varepsilon_M+2\varepsilon_{eff}}=0 \tag{6-1}$$

Relates the effective dielectric function ε_{eff}, the dielectric function of the particle ε, and that of the matrix ε_M and the volume fraction of the particle *f*. So far no effort has been paid to study the percolation in NP film sintering. This process is very interesting and unique since it may not be modeled by the commonly accepted BA model. As-deposited NP film consists of closely packed particles insulated by thin organic surface layer. In this film, metal concentration *P* is usually high, which could be higher than the percolation threshold P_c=0.5 (0.33) predicted by 2D (3D) Bruggemann approximation. Furthermore, BA model is considered suitable for random films. For the as-deposited films, each nanoparticle is covered with electrically isolated layers. Since the conductivity of the covering layer is much lower than the silver nanoparticle core. Strictly speaking, in this case, the film can not be considered as completely random. Therefore, BA may not be applicable for percolation modeling and numerical calculation is required, which will be demonstrated in the present study.

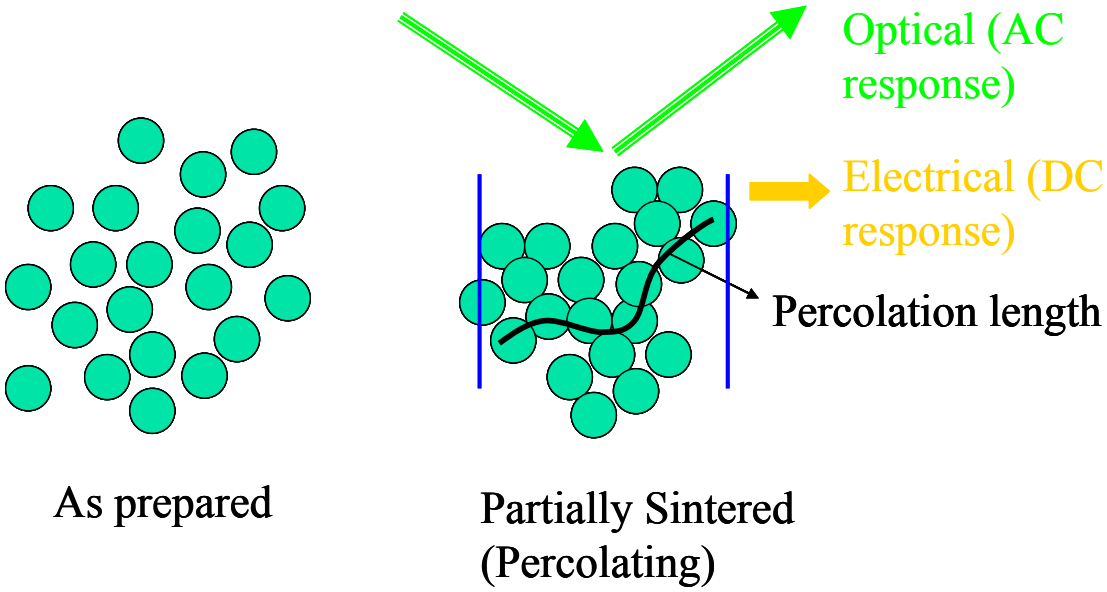

Fig. 6. 1 The illustration of percolation probing in solution deposited nanoparticle film sintering.

6.2 Experimental Method

Silver nanoparticles of size ~30nm was purchased from Sumitomo Inc. A thin organic surface coating exists on the surface to avoid nanoparticle agglomeration. NP suspension was prepared by adding 0.75g NPs to a mixture of 5ml ethanol and 0.5ml ethylene-glycol (EG). NP suspension was then spin-coated on a glass slide. Half of the slide's back surface was roughened to eliminate back reflection during ellipsometric measurement. The other half was left clear to facilitate normal transmission measurement, as illustrated in Fig.6.2d inset. Thermal sintering was performed in argon ambient on a hot plate at temperature of 250ºC. Samples with different sintering times were prepared for characterizations.

Optical properties of NP films were characterized by a spectroscopic ellipsometer (J.A. Wolllam Co.). The measured spectra range is from 0.75eV to 3.5eV. The ellipsometric angle (ψ) and phase difference (Δ) were recorded at an incidence angle of 75°. The normal incident transmission was also measured and used together with ψ and Δ to optimize curve fitting. By this way, refractive index and thickness can be uniquely determined and direct fitting of n, k and thickness is possible [A Short Course in Ellipsometry]. Two methods of fitting were employed. Firstly, the refractive index n, k and film thickness were declared as direct fitting parameters. Secondly, a two-oscillator model, as expressed as follows, was used to simulate the dielectric function:

$$\varepsilon(E) = \varepsilon_{\infty} + \frac{A_1}{E_1^2 - E^2 - i\Gamma_1 E} + \frac{A_2}{E_2^2 - E^2 - i\Gamma_2 E} \tag{6-2}$$

where $\varepsilon(E)$ is the effective dielectric function as a function of photon energy E, ε_{∞} is the value of real part of dielectric function at large photon energies. In each oscillator, A is the amplitude, Γ is the dissipative broadening and E_N is oscillator resonance energy, all in units of eV. The parametric model is particularly useful in revealing the physical implications behind the

directly fitted results. A two-layer model consisting of substrate and NP layer has been used to represent the sample.

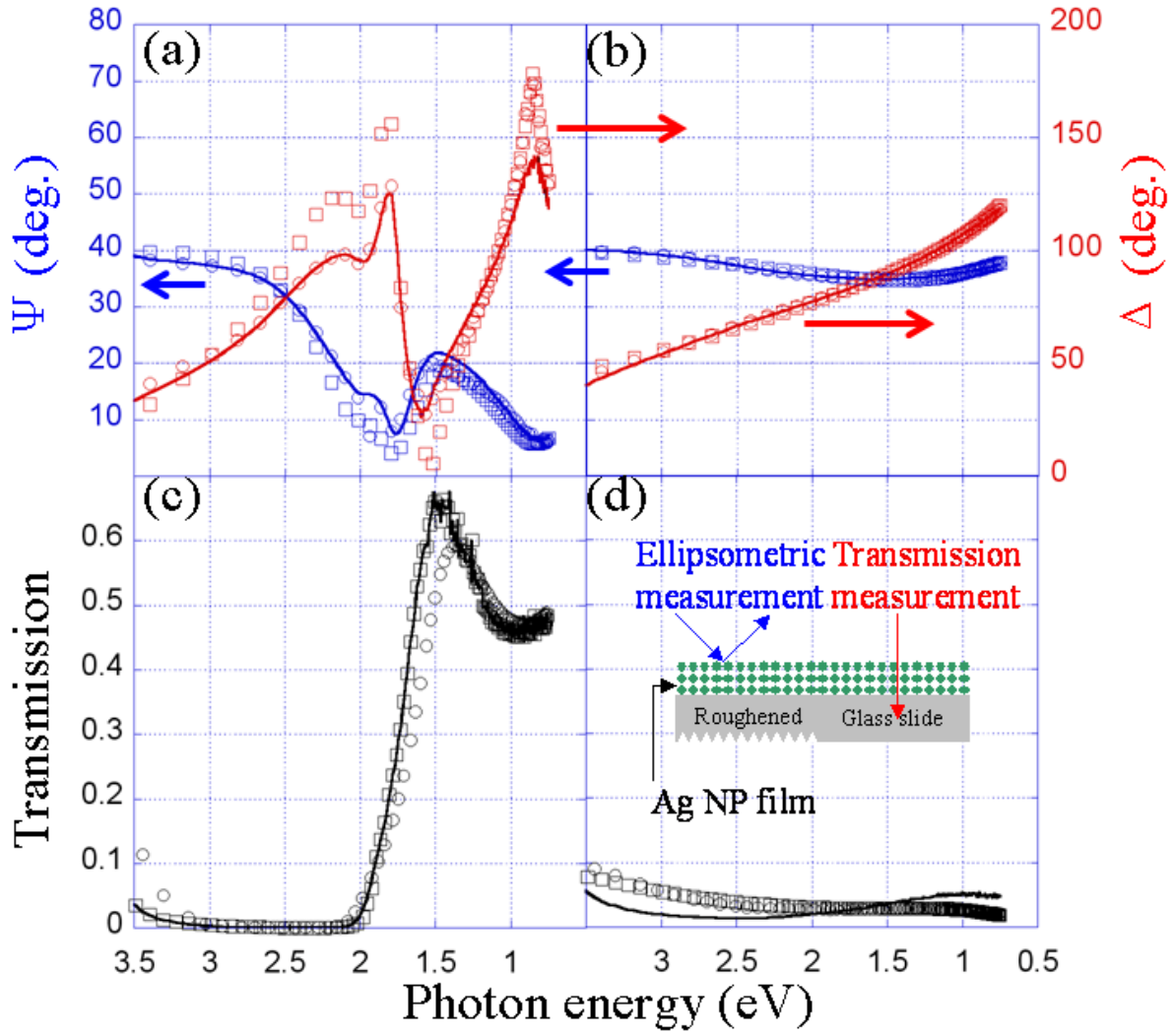

Fig. 6. 2 Ellipsometric data (ψ,Δ). Experimental (solid curves), two-oscillator model fitted (□), and direct fitted (○) for as-deposited NP film (a) and film sintered for 18mins (b), Normal incident transmission of as-deposited NP film (c) and film sintered for 18mins (d). Inset shows the measurement configuration.

6.3 Results and Numerical Analysis

Figure 6.2 shows the experimental (solid curves) and fitted (symbols) spectroscopic spectra of ψ and Δ as well as transmission as a function of wavelength for as-deposited and sintered NP films. Good agreement between the experimental and fitted spectra was obtained. For as-deposited film, a single Lorentz oscillator is sufficient to reproduce experimental and directly fitted results as shown in Fig.6.2a. It is expected since the as-deposited NP film consists of closely packed NPs that are electrically isolated from each other by organic surface layer, therefore electrons are confined within NPs. On the other hand, for sintered films two oscillators are required to provide a good fitting (Fig.6.2b&d). The positions of the two oscillators, labeled as *A* and *B*, can be identified in

the extracted dielectric function ε_1 and ε_2 for films after different sintering times (Fig6.3b). As-deposited film exhibits a Lorentz oscillator *A* with the resonance energy located at ~2.2eV. Considering that the plasmon frequency of isolated Ag NPs in air is ~3.5eV, the lower value observed herein is due to the close packing between neighboring NPs and surrounding dielectric layers. The Lorentz shape *A* undergoes substantial broadening, reduction in amplitude and red shift while the other oscillator *B* appears in the near infrared range upon thermal sintering. The magnitudes of *A* and *B* were summarized and plotted in Fig.6.3a(i) against sintering time. Oscillator *B* appears at ~13mins and its value approaches zero after ~17mins. The evolution of the film thickness obtained from both direct fitting and two-oscillator model is plotted along with AFM measured values (Fig.6.3a(ii)) and reasonable agreement was found. This validates the use of the empirical two-oscillator model to quantify film transition. Further validation will be shown via numerical simulation.

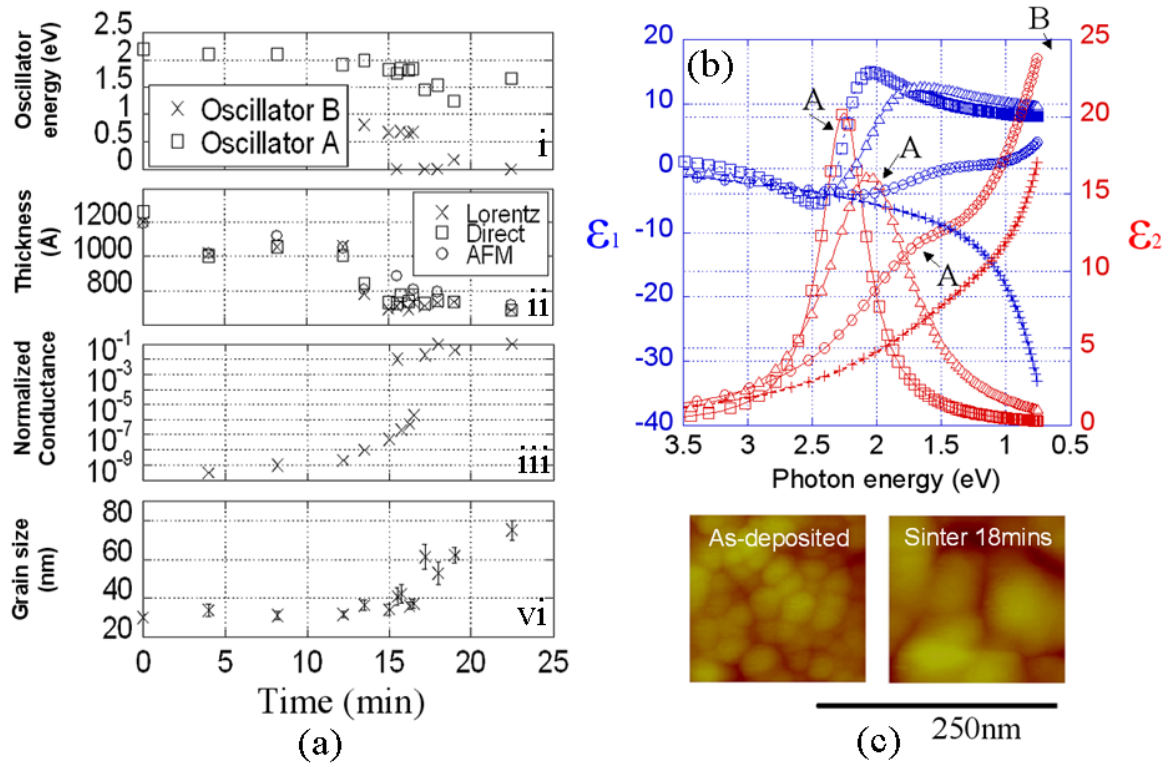

Fig. 6. 3 (a) The evolutions of oscillator energy (i), the thickness (ii), DC conductance (iii) and grain size (vi) as a function of time. (b) Spectra of dielectric functions ε_1 and ε_2 for NP films: (□) as deposited, (△) sintered for 4 mins, (○) sintered for 15 mins and (┼)sintered for 18 mins. (c) The AFM images NP films.

A semiconductor analyzer (4155A, Agilent) with two probes separated by 2mm was used to measure the DC conductance of each sample. The measured DC conductance of the sample sintered for 22.5mins was used to normalize the values measured for other samples. The evolution of the conductance is plotted in Fig.6.3a(iii). The DC conductance increases abruptly (indicating percolation) at ~17mins. The conductance variation correlates well with the behaviors of oscillators *A* and *B*, namely the normalized conductance falls in the range 0.1-1.0 only when *B* moves close to

zero (<0.25eV). The AFM images taken for each sample clearly show the growth of NP size as a result of thermal sintering (Fig.6.3a(vi) and Fig.6.3c).

To acquire more data points during the percolation transition and furthermore examine the correlation between optical and electrical signals, *in-situ* ellipsometric and DC conductance measurements were also performed. To facilitate *in-situ* DC measurement, a NP solution was spun on a Si wafer where Au electrodes with gaps of L=6 μm and 20 μm were lithographically patterned. The two-oscillator model was used to fit the ellipsometric data (w/o transmission). The oscillator energy and normalized conductance were plotted in Fig.6.4. For the smaller L=6 μm gap, the system percolates when B~ 0.8eV, while for larger system with the L=20 μm gap, the percolation requires lower energy of B.

To explain the observed experiment facts, quasi-static *dc* and *ac* calculations based on network of 2D R-L-C (resistance, inductance and capacitance) were carried out. In a first order approximation, 2D system is assumed considering the fact that the film has 3-4 layers of NPs and should be in the transition from 2D to 3D [Zhang *et al.* (1995)]. In the quasistatic limit, the Maxwell equation for electric field is reduced to the current conservation law

$$\nabla \cdot j = 0 \tag{6-3}$$

where j is the local current. This equation can be discretized on a 2D square lattice so that the film that constitutes a binary composite of metal NPs and dielectric layers can be represented via metallic and dielectric bonds connecting the lattice sites (Fig.6.5b inset). Thus, each metal NP consists of 24 metal bonds forming a square surrounded by dielectric bonds representing a dielectric layer covering the metal NPs (Fig.6.5b left inset). The NP sintering and connecting processes are modeled by randomly replacing dielectric bonds with metal bonds (as for example shown in the Fig.6.5b right inset and Fig.6.5c). The percentage of dielectric bonds being replaced (filling percentage) indicates the level of sintering. Drude's formula is used for metal permittivity:

$$\varepsilon_m(\omega) = \varepsilon_b - (\omega_p / \omega)^2 / (1 + i\omega_\tau / \omega) \tag{6-4}$$

where ε_b is the contribution due to the interband transitions, ω_p is the plasma frequency and ω_τ is the relaxation rate. For silver, ε_b=5.0, ω_p=9.1eV and ω_τ=0.021eV. For dielectric layers, ε_d=2.25. The discretized equations were solved numerically using Block Elimination method [Genov *et al.* (2003)].

Prediction of the imaginary part of the effective dielectric function ε_2 for an array of 38×38 NPs with different filling percentages is presented in Fig.6.5a from 0.7eV to 2.0eV and Fig.6.4b from 2.0eV to 3.0eV. Due to the sintering and connection between neighboring NPs, a wide distribution of larger cluster size appears in the film which gives rise to a collection of plasmon resonances from 0.7eV to 2.0eV. It is interesting to find that ε in this range (the collection of plasmon resonance) can effectively be approximated by single Lorentzian line shape consistent with the experimental trend. The fitting also reveals that the location of peak B moves toward lower energies as the filling increases (Fig.6.5a). The peak A in Fig.6.5b due to the plasmon resonance of original NPs has Lorentzian shape and is located at ~2.6eV. The amplitude of A reduces substantially with filling percentage rises per the experimental observation. It is therefore deduced that the empirical two-oscillator model applied in the analysis of the ellipsometric data originates physically from these two peaks A and B just described.

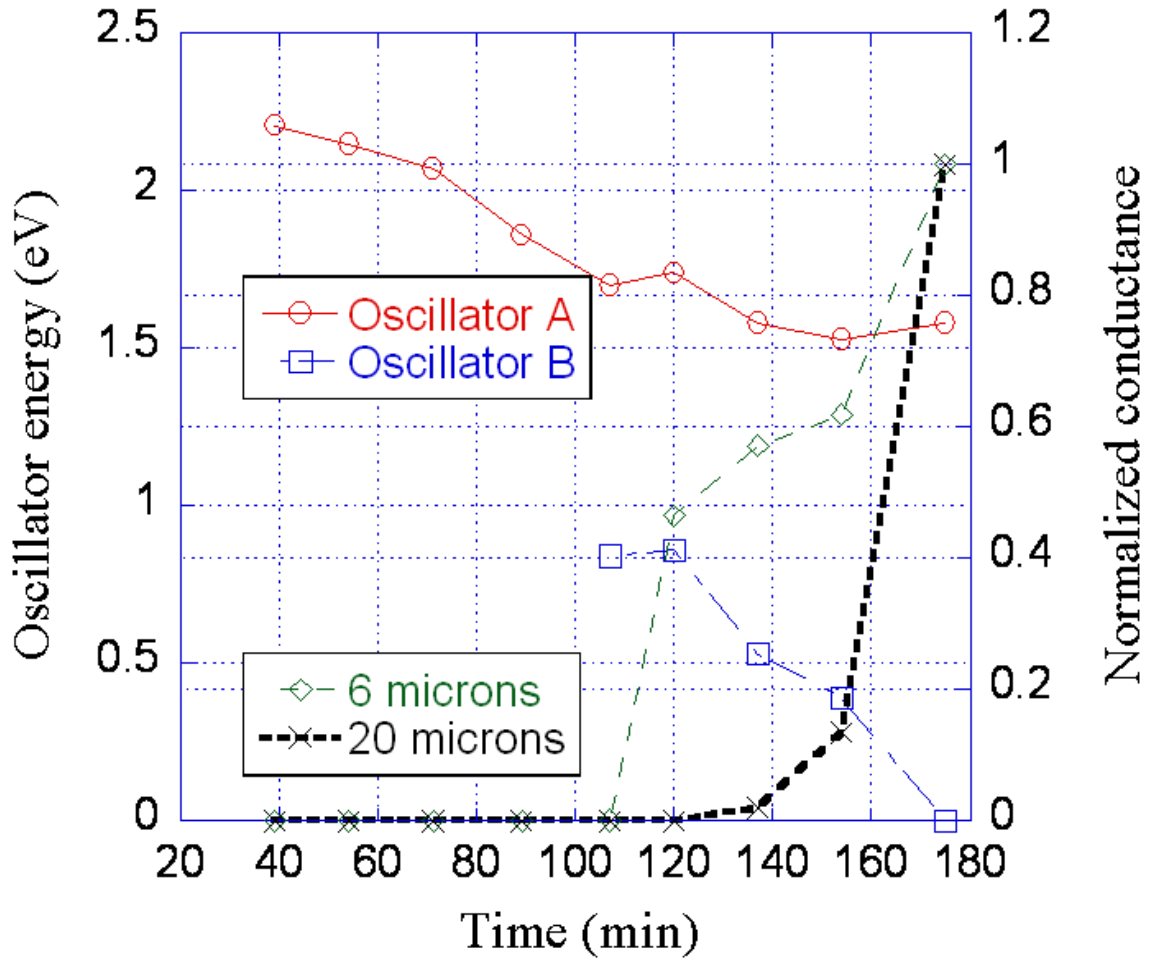

Fig. 6. 4 *In-situ* ellipsometric (evolution of oscillator energy A and B *vs.* time) and DC measurement (evolution of conductance for electrode gap of 6 μm and 20 μm *vs.* time) results.

Finally the correlation between the position of *B* and DC conductance was evaluated numerically. The DC conductance was calculated for an array of 75×75 NPs and an array of 83×83 NPs respectively with filling percentage of 15%. With this filling percentage the peak *B* is located at ~0.8eV (0.78eV, Fig.6.5a). This value is chosen because Fig.6.5 shows experimentally with oscillator energy *B* at ~0.8eV, percolation occurs for system with size ~6 μm. Numerical calculation of DC conductance reveals that with 15% filling, the array of 75×75 percolates but not for the array of 83×83. This implies the longest cluster size in the film will be $\sim80\times NPsize$ or percolation occurs for any measuring system smaller than this size. Let *NP size be* 40nm (larger than original NP size 30nm considering NP growth, Fig.6.3a(vi)), $80\times NPsize = 3.2\mu m$ which is close to experimental observation that when *B*~0.8eV, transition occurs with a characteristic size *L*=6 μm.

6.4 Conclusion

In conclusion, the sintering of solution-deposited silver nanoparticle films has been characterized by VIS-NIR SE. The results show dielectric functions and thickness of the film during sintering can be monitored by this non-contact optical method. Furthermore, the parameterization of dielectric functions using a two-oscillator model provides direct connection between optical and DC electrical properties. The percolation in various sample sizes, e.g. from μm to *mm*, can be identified readily from SE measurements.

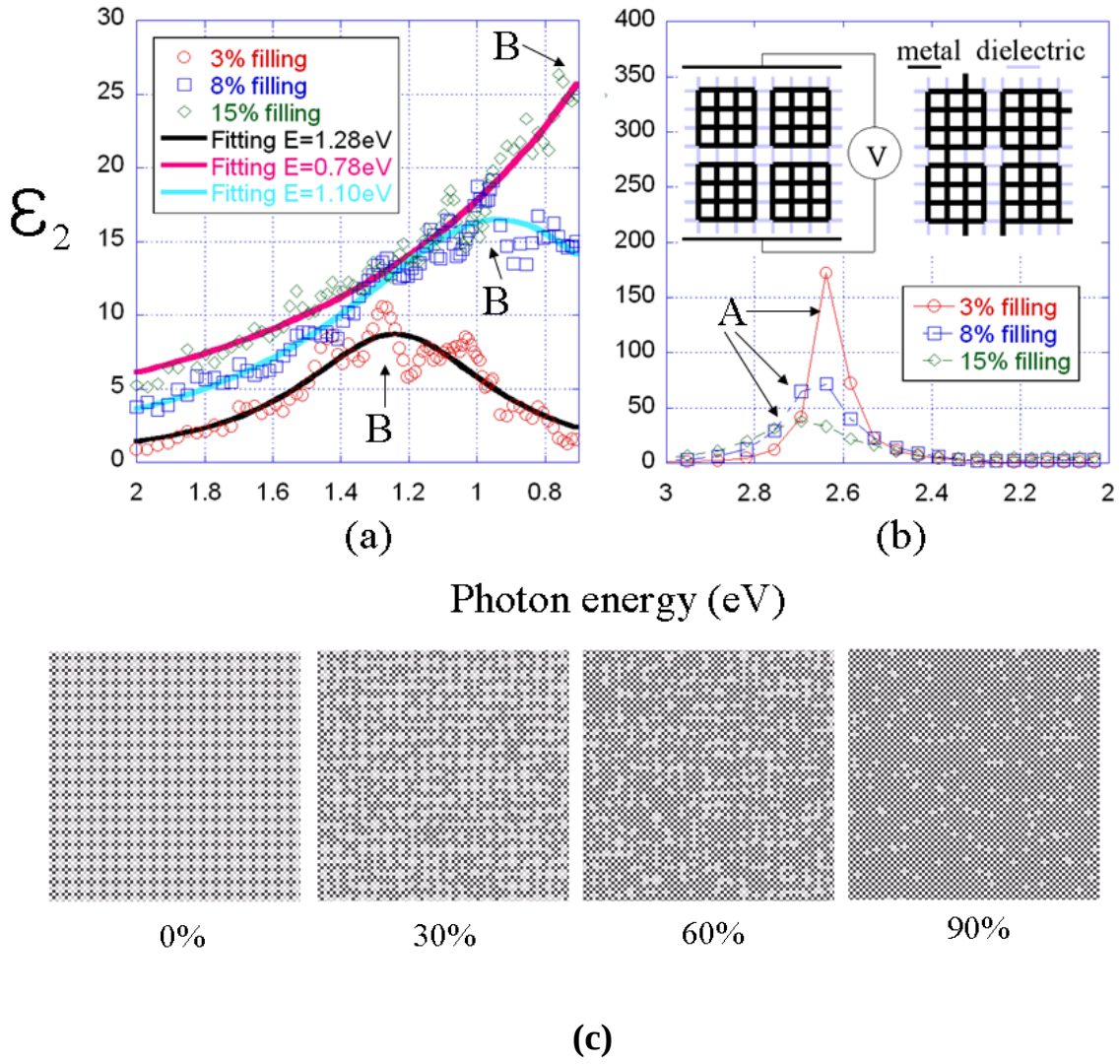

Fig. 6. 5 Calculated imaginary part of dielectric function ε_2 for various filling percentages. (a) from 0.7eV to 2.0eV and (b) from 2.0eV to 3.0eV. The inset shows the R-L-C network configuration and the representation of NP film structure and sintering process for *ac* and *dc* calculations. The black bars and gray bars represent metal bonds and dielectric bonds respectively. Metal NP consists of 24 metal bonds and forms a square surrounded by dielectric bonds. The dielectric bonds can be replaced by metal bonds randomly to simulate the sintering process. (c) The illustration of the film with different filling ratios.

CHAPTER 7

HIGH-THROUGHPUT NEAR-FIELD OPTICAL NANOPROCESSING OF SOLUTION DEPOSITED NANOPARTICLES

The application of nanoscale electrical and biological devices will profit from the development of nanomanufacturing technologies that are high-throughput, low cost and flexible. Utilizing nanomaterials as building blocks and organizing them in a rational way represents an attractive approach towards this goal and has been pursued for the past few years. This chapter presents a new scheme for the high-throughput optical near-field nanoprocessing of nanoparticles. The method unitizes fluidically assembled microsphere as near-field focusing lens array for laser assisted nano-sintering or nano-ablation of nanoparticles. Benefiting from the low processing temperature and the reduced thermal diffusion in the nanoparticle film, minimum feature size down to ~150nm can be realized. In addition, we observed that smaller feature (50nm) can be obtained by furnace annealing laser-sintered nanodots at 400° C. Molecular dynamics simulation and thermal modeling are performed to predict nanoparticle film thermal conductivity and processing temperature. Electrical conductivity of sintered nanowire is studied. Using nanowire electrodes with submicron gap, we subsequently fabricate organic field effect transistors (FETs) with oxygen stable semiconducting polymer.

.

7.1 Introduction

The nanomanufacturing technique to fabricate nanoscale devices and patterns for various electrical and biological applications including nanobiosensing [Cui *et al.* (2001)], displays [Lee *et al.* (2002)] and data storage [Tseng *et al.* (2005), Park *et al.* (2009)] etc, is an area of intense research. Essentially, it requires the generation of nanostructures of metals, semiconductors, metal oxides, polymer and biologically active molecules with well-defined feature size, shape, spacing, orientation and properties. In addiction, the ability to masklessly generate arbitrary nanostructures of various materials will undoubtedly contribute to device design shifts, the fundamental study of molecular and cell biology, and nanopatterning of multiple biomolecule nanoarrays. Another important experimental challenge entails fabrication of controlled and functional nanostructures on large area while keeping the cost at low level.

Traditionally, metallic and semiconducting nanostructures are fabricated through conventional lithography based processes, such as e-beam lithography and DUV lithography. These processes are subject to limitations in that they are multi-step, strong solvents and carry a high cost of implementation. In order to alleviate the limitation on high capital investigation and render substantial flexibility, a number of maskless nanopatterning approaches have been introduced, including both optical and non-optical methods. Optical nanopatterning would generally require near-field configuration to overcome the theoretical diffraction limit. Features of size much smaller than the optical wavelength have been produced by illuminating the tip of an AFM or via delivery through a near field scanning optical microscope (NSOM) tip to create near-field effects [Chimmalgi *et al.* (2005), Hwang *et al.* (2006), Sun *et al.* (2006)]. Self-assembled array of microspheres would generate nano features at large area but only in hexagonally-close-packed patterns. Direct writing by optical trapped microsphere overcomes this issue and enables arbitrary nanopatterning [McLEOD *et al.* (2008)], although the processing needs to be conducted in fluid environment, which may limit the applicable material systems. Plasmonic lithography is a new emerging technique which utilizes an air slider for maintaining a precise spacing between the plasmonic lens and substrate. The high speed scanning of the slider imposes severe requirements on the substrate smoothness [Srituravanich *et al.* (2008)]. On the other hand, this method has been demonstrated todate on materials pertinent to optical storage. Essentially all the above methods require patterning of bulk thin films, hence multiple steps are needed and the processing temperature is generally high. Non-optical processes include nanoimprinting [Chou *et al.* (1996)], gravure printing [Kraus *et al.* (2007)], electrodynamic printing [Park *et al.* (2007)], dip-pen [Piner *et al.* (1999)], and fluid assembly [Li *et al.* (2008), Pauzauskie *et al.* (2006)], etc.

To massively generate nanostructures, e.g. nanowires and nanodots, in a single step, this work suggests an entirely new route of nanomanufacturing where solution-carried ultra-small nanoparticles (1-3nm diameter) are used as building blocks [Ko *et al.* (2006), Pan *et al.* (2008), Pan *et al.* (2008)] for nanostructuring with 100nm-200nm resolution. The solution deposition eliminates the need of multiple steps and vacuum deposition. The suppressed melting temperature of nanomaterials also eliminates the need of high temperature processing. This process can significantly simplify the manufacturing process and allows potential applications that are low temperature and extremely low cost while maintaining reasonable spatial resolution and properties. The versatility of this approach also exhibits itself in the easiness for adapting to different material systems. In solution processing, in general, materials are deposited in solution phase (e.g. printing) followed by nanopatterning and/or annealing steps for achieving superior spatial resolution. Reasonable electrical and optical properties are required to create functional devices. The capability to deliver these nanostructures on a large scale and at a cost effective way remains a

challenging task. Towards this objective, the present work introduces an alternative implementation of microsphere near-field focusing for large scale optical nanoprocessing of solution deposited nanoparticles. The microspheres are assembled into a regular array and brought parallel to the substrate utilizing capacitance distance sensing. Each microsphere, used as a near-field focusing lens, can be addressed individually by spatial light modulation. The laser nanoscale processing includes sintering of nanoparticles to generate conductive structures and ablation to generate negative structures. This technique may find a host of potential applications in electrical and biological nanoarray technology. For example, using this technique nanowire transistor arrays or transistor with nanochannels can be produced with relatively high-throughput. Biological nanostructures can be created by first generating gold or metal-oxide nanostructures technique to subsequently attach the biomelecules of interest selectively. It can also be exploited in the patterning of large-area plasmonic metallic nanostructures for surface enhanced Raman scattering (SERS) and biomedical sensing. Another area that will benefit from this novel platform technology, thanks to its flexibility in terms of pattern shape, is the study of cell adhesion and motility. In present work, we will mainly demonstrate the feasibility of massively generating gold nano features down to ~150nm using this method and further annealing result in 50nm size and better crystalline structure. We furthermore demonstrate the so-fabricated nanowires can be used for organic FETs with oxygen stable poly(3-hexylthiophene) deposited from solution phase.

7.2 Experiment methods

7.2.1 Experimental apparatus.

The process illustration and detailed experimental apparatus are shown in Figure 7.1. A nanosecond (Nd-Yag, New Wave) and a continuous (Argon, Lexel) laser were used for nano-ablation and nano-sintering respectively. The laser beam was directed towards a Digital Micromirror Display (DMD, Texas Instrument, 400x600 pixels) array and the modulated beam is then focused by a 10X long working distance objective lens onto the microsphere array (Fig.7.1d). Two 5-axis translational/tilting stages were used to precisely position the microphere array slide (processing slide) and the ITO slide (target slide). A PVP (poly-4-vinylphenol, MW~8,000AMU) dielectric layer dissolved in hexanol with a small amount of the cross-linking agent, poly(melamine-co-formaldehyde), was spincoated on the ITO slide. The PVP served as dielectric layer for devices and wetting layer for subsequent nanoparticle deposition. 1-3nm sized gold nanoparticle (nanoinks) encapsulated by hexanethiol self-assembled momolayer (SAM) in organic solvent (alpha-terpineol or toluene) were spun coated on. The gold nanoparticles were synthesized using a two-phase reduction method (details are in supporting materials). SAM is critical for nanoparticles because it controls the size of the nanoparticles in addition to enhancing long term stability and achieving favorable optical properties through Au-thiol chemistry. Uniform nanoparticle films were obtained by adjusting the spin speed and evaporation.. In order to control the gap between processing slide and target slide, a high precision LCR meter (Instek LCR-821) was used to measure the capacitances. Four pads were fabricated lithographically on the processing slide near the microsphere array. Each of the pads and the target slide (ITO) were counter electrodes for one capacitor, where the gap between them can be monitored by capacitance measurement. The parallelism between the processing and target slides was ensured by repeatedly adjusting orientation until four capacitance values are equal. A description of the capacitance adjustment was found in the supporting materials. The range of capacitance suitable for laser

processing is of the order of several pF. Both top and bottom view during the processing could be observed by two CCD cameras.

7.2.2 Near-field focusing lense array preparation.

The near-field focusing lense array, which is the key to this process, was fabricated by lithography method. Four gold pads were firstly patterned on Pyrex glass slide by standard lift-off process. These pads were used together with the conductive surface (ITO glass) under the nanoparticle film as electrodes in capacitance measurement for gap control, Figure 7.2.

Four pads were positioned as shown in Figure 7.2 such that the gap and parallelism between two slides could be easily controlled without inducing crosstalks between axes. After the gold pads were defined, photoresist was spun on the glass and followed by a lithography step to define 20×20 holes arrays. The hole-to-hole distance was 13μm. The hole array was positioned at the center of the 4 pads as shown in Figure 7.3. The hole array was used as template to assemble microspheres. To assemble the microsphere, a cover slide was placed on the glass slide forming a gap of 30μm controlled by spacers. A drop of microsphere (~3μm in diameter, Bang Inc.) suspension was applied at the slide edges and capillary force moves the drop into the gap and spreads the suspension. After the solution was evaporated, the cover slip was removed and the glass slide was dipped into aceton after a short time annealing on hot plate. Photoresist was stripped off and a regular array of microsphere was left and ready to be used for laser material processing.

7.2.3 Thiol-capped gold nanoparticle optical properties and film thickness measurement by ellipsometry.

The thiol-capped gold nanoparticle solution was spin-coated on the PVP coated glass slide. The thickness and optical properties of PVP were measured separately before the nanoparticle film coating. Both transimission and ellipsometric parameters (ΨandΔ) were measured using a VIS-NIR ellipsometry (Woollam inc). The refractive index was obtained by simultaneously fitting transmission, Ψ and Δ, as shown in Figure 7.4.

7.2.4 Thiol-capped nanoparticle synthesis.

The gold nanoparticles were prepared by the two-phase reduction method. Aqueous metal salts (HAuCl4) were mixed in a toluene solution containing long-chain alkylammonium surfactants to form a two-phase system. 1.5 g of tetroactylammonium bromide was mixed with 80 mL of toluene and added to 0.31 g of hydrogen tetrachloroaurate (III) hydrate ($HAuCl_4 \cdot H_2O$) in 25 mL of deionized (DI) water. Vigorous stirring transferred the metal salt ($AuCl_4$) into the organic phase (toluene) and the aqueous phase was removed. A measured quantity of capping agent, a long-chain thiol (hexanethiol), was added to the gold solution while stirring. A reducing agent, sodium borohydride ($NaBH_4$), mixed in 25 mL of water was then added into the organic phase over approximately 10s to nucleate nano-crystals. The mixture reacted at room temperature for three and a half hours. The toluene was removed with a rotary evaporator and the leftover black particles suspended in ethanol and sonicated briefly. The particles were washed with ethanol and acetone and air dried. The average nano-crystal size was coarsely tunable by adjusting the ratio of capping groups to metal salt, whereas size selective precipitation was employed to narrow the initial size distribution. In this method, the size distribution of synthesized nanoparticles is controlled by the ratio between metal salt and surface monolayer that additionally prevents the agglomeration of nanoparticles. The size of synthesized nanoparticles was distributed in the range of 1 to 3 nm as

measured by TEM. Monolayer-protected gold nanoparticles were suspended in *a*-terpineol with 10 %in weight

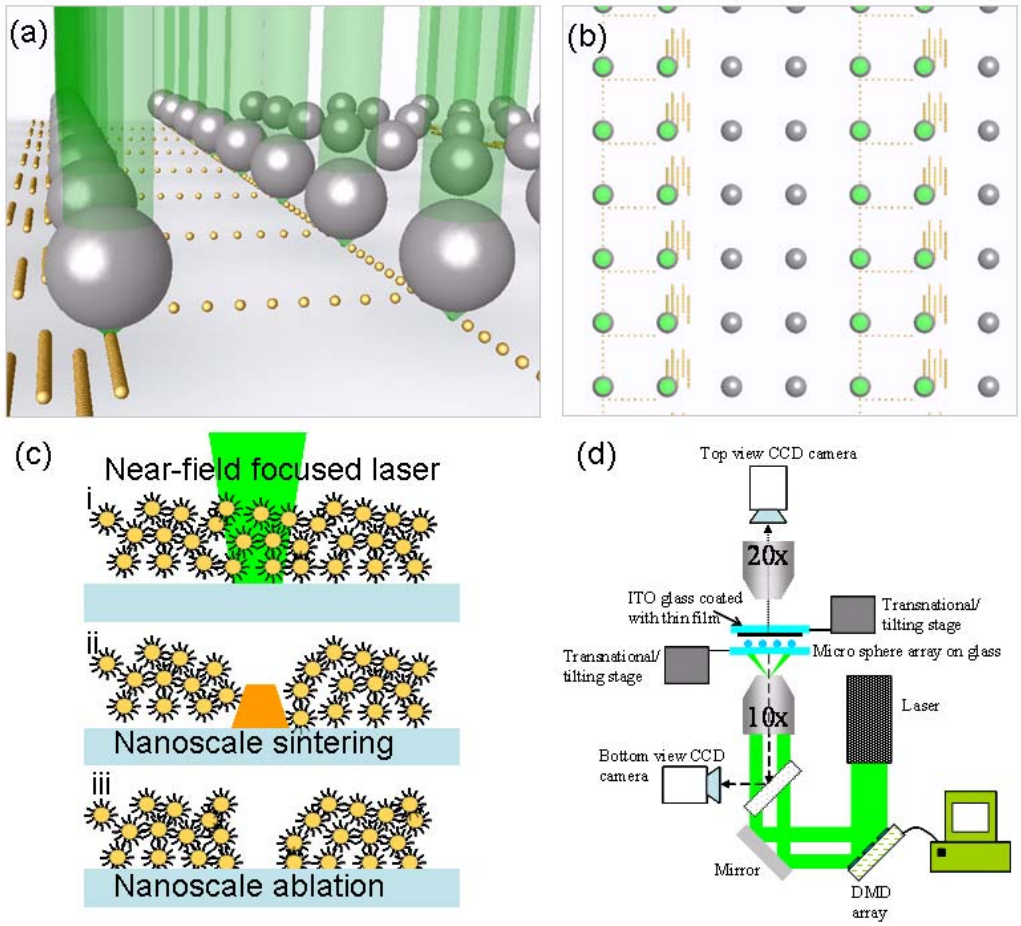

Figure 7. 1 Concept illustrations of the high-throughput near-field nanoprocessing and experimental apparatus. (a) 3D illustration of the process. (b) The microsphere array can be selectively illuminated (as indicated by green dots) for arbitrarily patterning. (c) Illustration of near-field laser nanoprocessing (sintering and ablation) of solution deposited nanoparticles. (d) Experimental apparatus of the laser processing.

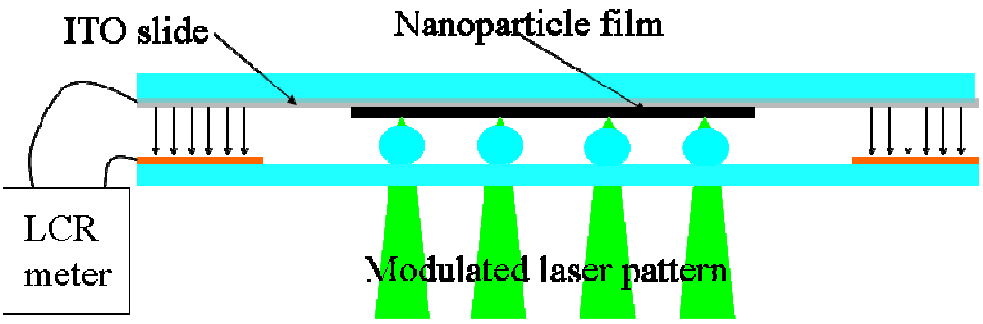

Figure 7. 2 The configuration for gap control.

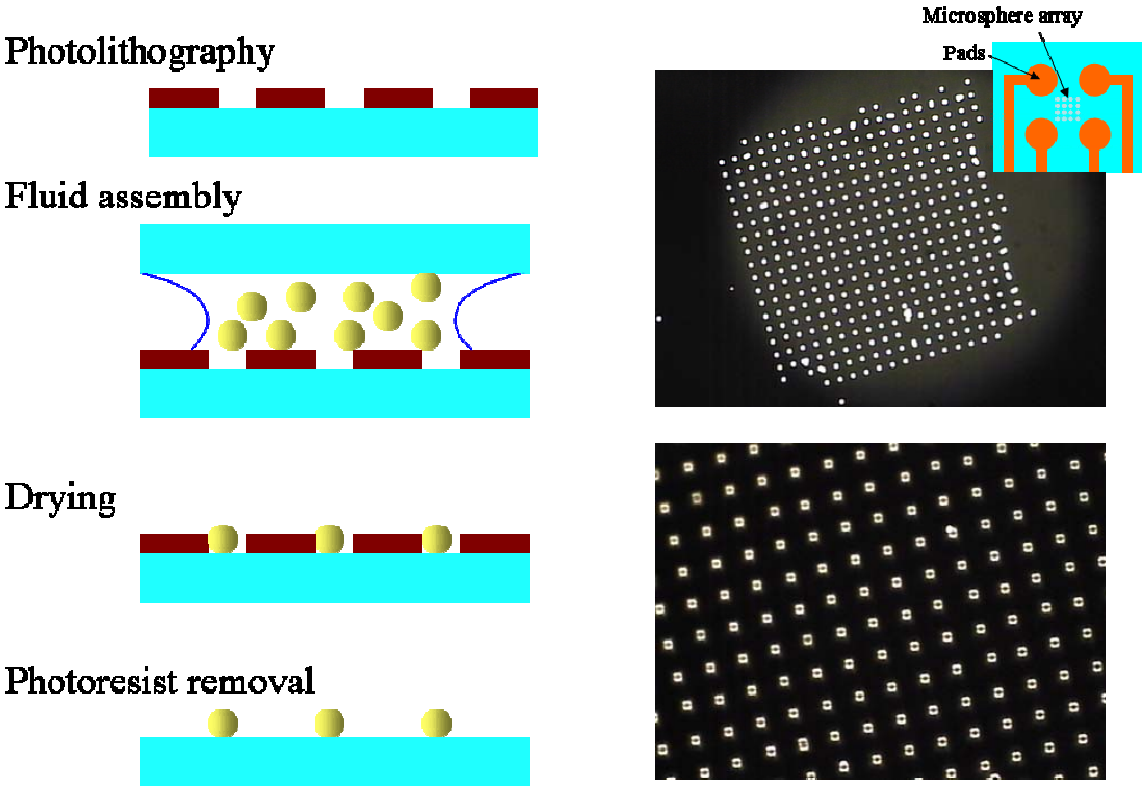

Figure 7. 3 The self-assembly of microsphere arrays.

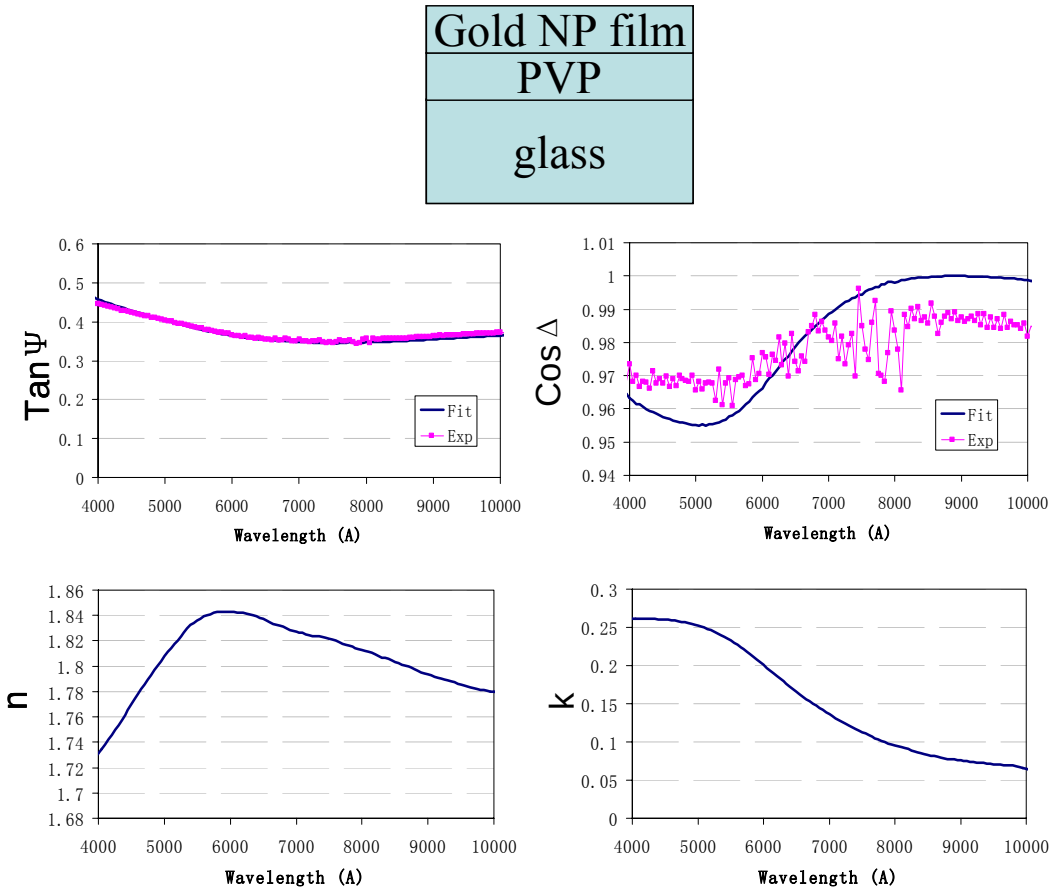

Figure 7. 4 The ellipsometric measurement of optical properties of nanoparticle film.

7.3 Molecular dynamics simulation of thermal properties of hexanethiol-capped gold nanoparticles

In the MD simulations, a united atom model was used for SH, CH2 and CH3. The united atom interacts with each other with Lennard-Jones pair interactions. The interactions used in our MD simulation include united-atom model potential describing intra- and intermolecular interaction of the alkyl (CH_2 and CH_3) segments: a sulfur-to-gold interaction Morse potential, sulfur-sulfur and sulfur to alkyl-segment interaction, and an alkyl-segment to Au interaction [Hautman *et al.* (1989)][Luedtke *et al.* (1996)][Zhao *et al.* (2006)]. The potential for gold atoms is the glue potential [Ercolessi *et al.* (1998)].

To validate the potential, the interaction of two thiol-capped nanoparticles was examined. The nonequlibrium steered MD simulation was used to compute the potential of mean force between two particles. The mean force F_{mean} for two NC constraints at distance r was defined as the average force in direction of their connecting line. The PMF is defined as

$$\phi_{MF}(r) = \int_r^{\infty} F_{mean}(s)ds \tag{7-1}$$

The calculated potential of mean force of two hexanethiol capped nanoparticles (gold core diameter 2.4nm) is plotted in Figure 7.5(a). The potential reaches a minimum at around 3.7nm. The interaction energy is around 1eV with temperature at 266K which compares favorably with the value reported [Schapotschnikow *et al.* 2008].

The principle of the thermal conductivity determination is illustrated in Figure 7.5(c). Consider two plates located at L/4 to the left and right sides. Periodic boundaries were imposed in all directions. At each iteration, the particles in the plates were determined and a constant energy was added to P1 and substrated from P2. By this procedure, a constant heat flux per unit area was imposed. The energy modification was done by rescaling the velocities of the particles inside the plates. To avoid an artificial drift, this had to be done with the total momentum of the plates being zero. The thermal conductivity is given by

$$\kappa = -\frac{J}{\partial T / \partial x} \tag{7-2}$$

The temperature gradient can be extracted from simulation. The simulation was divided into 20 slides and temperature is calculated in each slide. The simulation was performed for 920000 steps when equilibrium was reached in the system. A linear distribution of temperature between P1 and P2 could be found after attaining equilibrium. The respective temperature gradient is shown in Figure 7.6.

7.4 Results on nanoablation.

The spun coated nanoparticle film had to be sufficiently dry before the ablation to avoid reflow and smearing out of the ablated feature. Figures 7.7-7.10 show the nano-ablation results. The atomic force microscopy (AFM) topography images of the features are shown in Fig.7.8b. Negative features with diameters from ~200nm to ~500nm were generated by varying the incident laser fluence. The beam focusing and normalized intensity distribution underneath the microsphere were calculated by the discrete dipole approximation (DDA) [Draine *et al.* (1994)] as shown in Fig.7.7a. The DDA calculated local intensity was particularly important in evaluating the crater profiles produced by laser ablation. Furthermore, it was also used to estimate the beam diameter and depth of focus. The beam diameter $2w_0$ was estimated as the intensity dropped to $1/e^2$ of the peak intensity at the center (Fig.7.7b). It can be observed the beam diverges from 630nm to 740nm as the measuring plane shifts from the tighter focusing plane (240nm below the microsphere) to the plane 740nm below. Therefore, the enhancement resulting from near-field focusing is affected by the gap between the microsphere and the target planes, although from a practical standpoint this variation is workable. To calibrate the gap distance, the capacitance was measured to be ~6.6pF when the microspheres touched the NP substrate (as evidenced by dents formed on nanoparticle film by the microspheres). The capacitance used during nano-ablation is ~5.5-6.0pF corresponding to ~300nm-600nm below the microsphere by invoking the simple relation between capacitance and gap distance. The distance was left intentionally to provide a conduit for ablated ejecta removal.

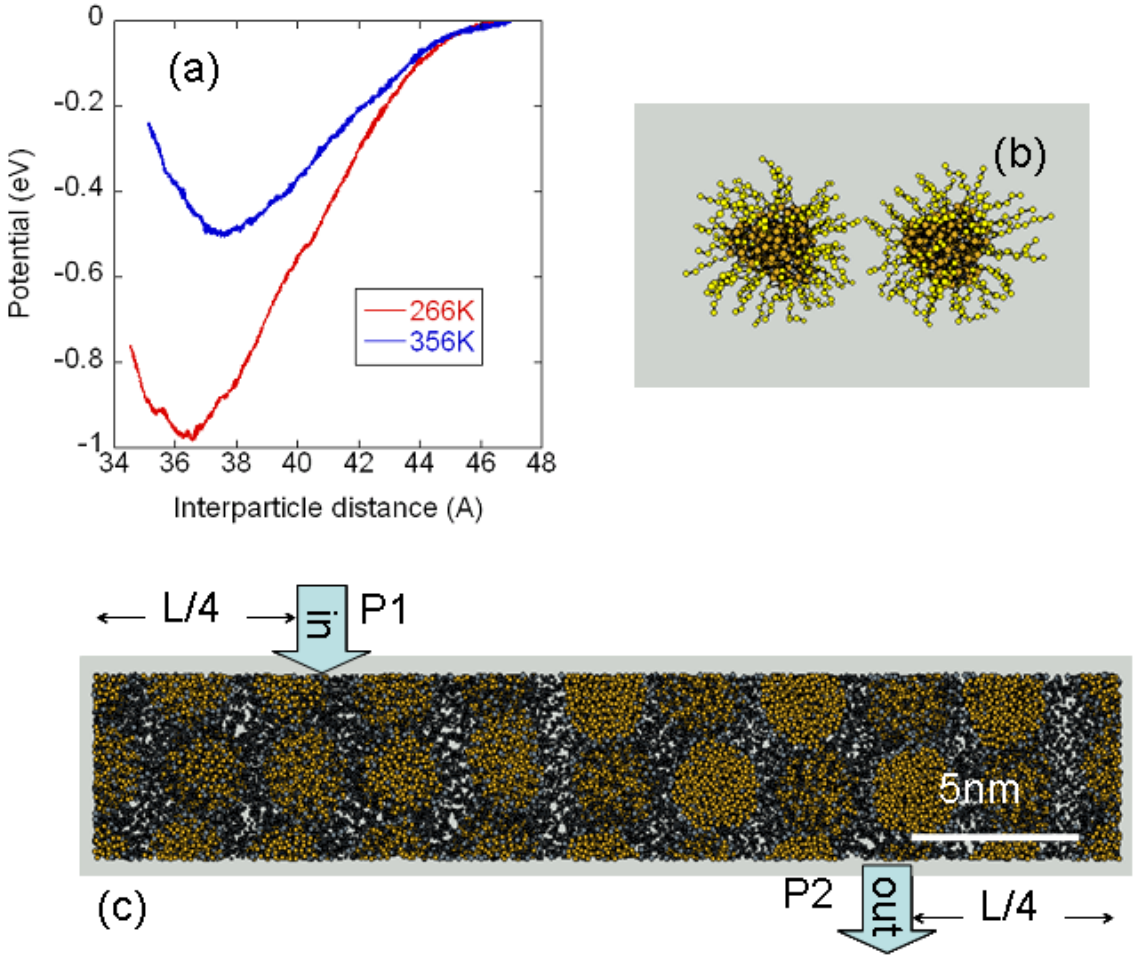

Figure 7. 5 The molecular dynamics simulation of thermal conductivity.

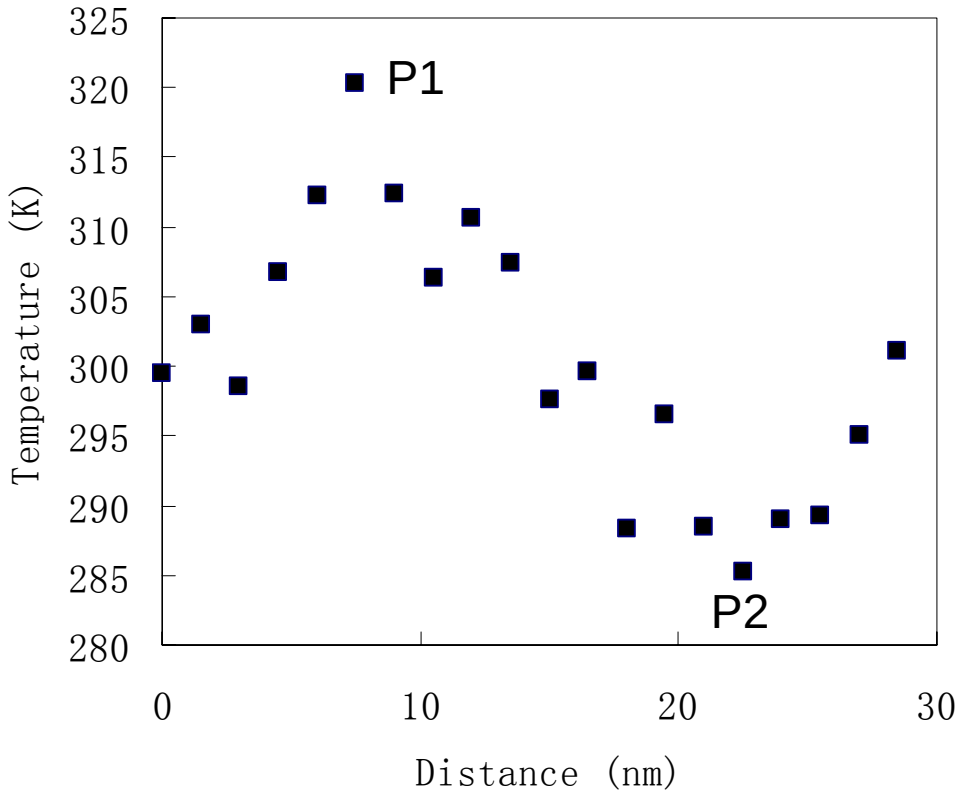

Figure 7. 6 The calculated temperature profile.

The feature diameter $2r_a$ vs. fluence can be fitted with the following equation to estimate the threshold F_A by assuming a beam diameter of 700nm,

$$r_a = \frac{w_0}{\sqrt{2}}\sqrt{\ln\left(\frac{N_{peak}F_{inc}}{F_A}\right)} \tag{7-3}$$

where N_{peak} is the near-field enhancement at the beam spot center that is estimated to be ~50, while F_{inc} is the incident laser fluence. The fitting results in a threshold fluence of ~190mJ/cm^2. Comparing to the reported threshold fluence ~40-80mJ/cm^2 in far-field laser micro-ablation of similar material [Ko *et al.* (2006)], the discrepancy is mainly due to the overestimation of the enhancement factor that could be due to inaccuracy in gap distance estimation and imperfection in the beam alignment. To shed a light on the complicated nano-ablation mechanism, the ablated volume is plotted vs. the laser fluence depicting a linear relation (Fig.7.9b). The linear trend suggests that evaporation could be a key ablation mechanism. The rapid heating of nanoparticle may produce temperature well above the evaporation temperature of the desorbed alkyl-thiols chains. The phase change involvement in ablation is also consistent with our molecular dynamic simulation finding that pure mechanical stress buildup caused by rapid thermal expansion is insufficient to ablate the nanoparticle film (not shown here). To demonstrate the capability for generating 1-D structures, the target slide was translated by piezoelectric actuators (1μm/s).

Direct writing of nano-trenches as well as massively parallel, high-throughtput manufacturing are shown in Fig.7.10, Ideally, the maximum translation distance required to fabricate continuous structures is the spacing between the microspheres – 13μm in the present study – which falls within the typical traveling range of most piezo-actuators.

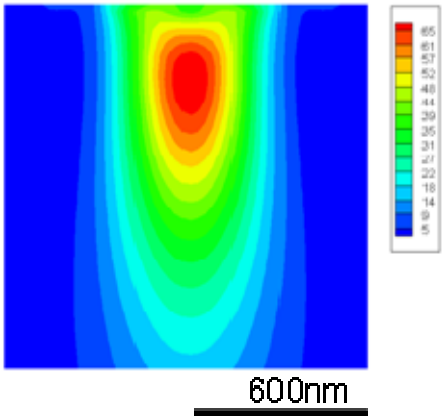

(a)

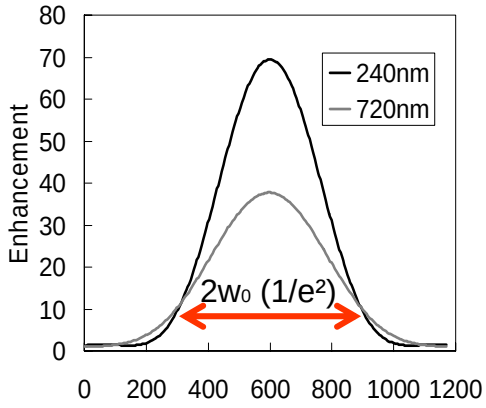

(b)

Figure 7. 7 (a) The near-field intensity distribution below the microsphere. The enhancement is relative to the incident intensity. (b) The plots of relative intensity at two focal planes located at 240nm and 720nm below microsphere. The red arrow indicates the focal spot diameter.

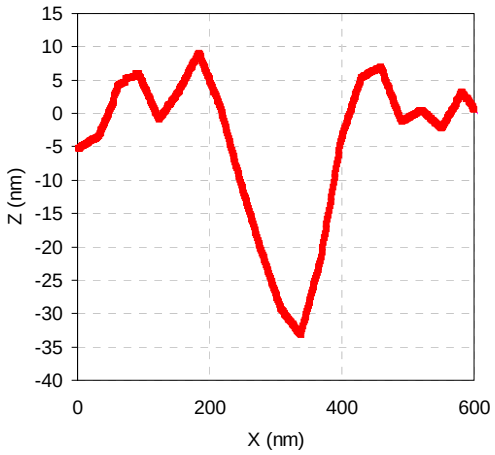

(a)

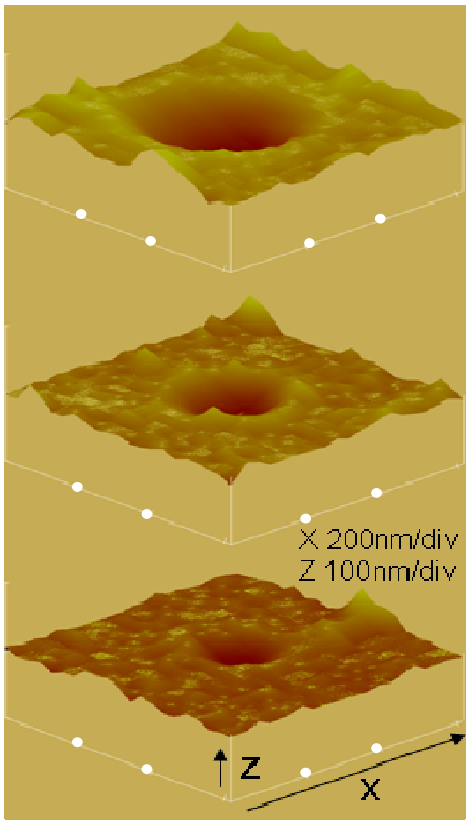

(b)

Figure 7. 8 (a) The AFM cross section profile of a typical nano-ablated nanostructure. $2r_a$ (diameter) is defined at the surface (z = 0 plane). (g) The AFM topographical imaging of the nano-ablated structure with incident fluence of 5.31mJ/cm^2, 5.05mJ/cm^2 and 4.76mJ/cm^2 from the top figure to the bottom.

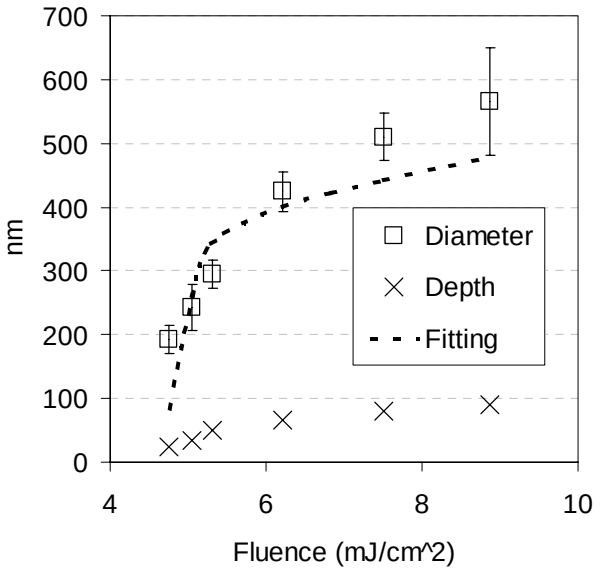

(a)

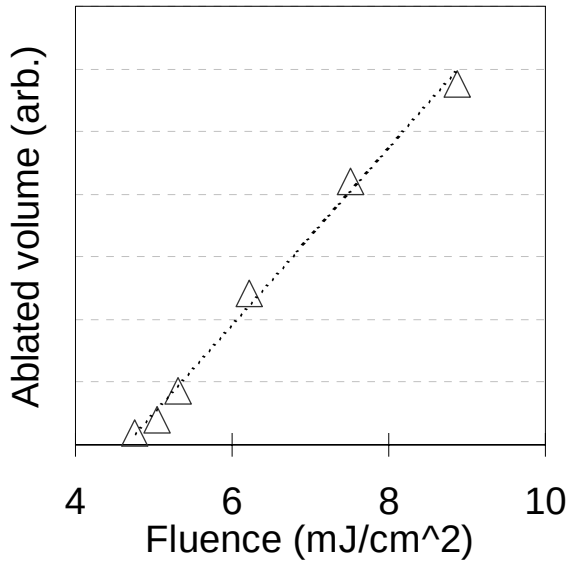

(b)

Figure 7. 9 (a) The plots of ablated feature diameter and depth vs. fluence, (b) The plot of ablated volume vs. incident laser fluence.

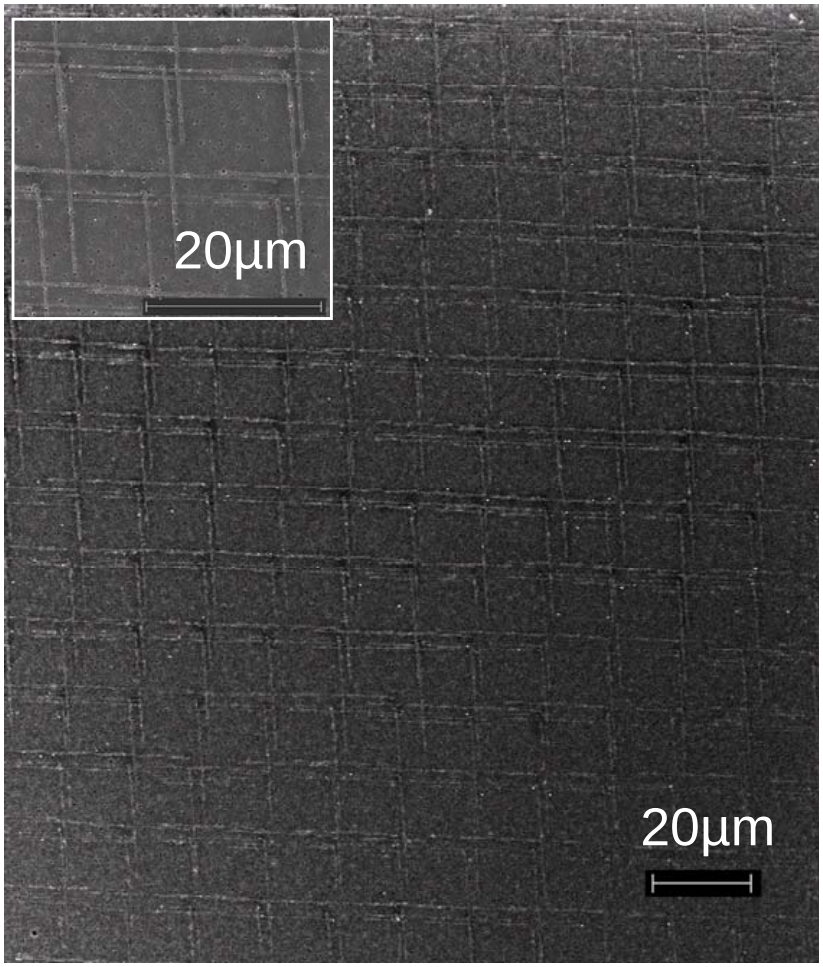

Figure 7. 10 The fabrication of nanolines (trenches) in large scale.

7.5 Results on nanosintering.

Furthermore, the nano-sintering was conducted with microspheres placed closer to the substrate (100-200nm underneath the microspheres, corresponding to capacitance of 6.3-6.5pF). The incident intensity is ~1.9e7W/m^2. The SEM images of sintered dots are shown in Fig.7.11a. It can be observed that due to the Gaussian type of laser intensity distribution, the sintering initiates at the center and propagates outwards (Fig.7.11a(i-iii)). The sintering leads to a dense solid metal structure at the center and less dense structure at the periphery of the sintered dot. The sintering involves desorption of thiol layers from gold nanoparticles and the subsequent sintering of exposed nanoparticles. The sintered dot size keeps increasing as time proceeds. Approximately ~200nm (~150nm with lower energy, Fig.7.11a(iv)) in diameter gold dots can be obtained after 5s sintering. After sintering, the sample can be submersed in toluene to wash away un-sintered nanoparticles. To further reduce the size, the sample can be annealed in furnace at 400ºC. Densification and beading help reduce the dot size down to about 50nm in diameter (Fig.7.11a(vi)). Conductive nanowires can be fabricated by translating the substrate while maintaining the gap. To measure the resistivity of the sintered nanowire, micropads were sintered by focused laser to bridge the nanowire and provide electrical contacts, in Fig7.12a. The measured resistivity is ~10-15 times higher than bulk gold. The high resistivity most likely is due to porosity and grain boundaries in the laser sintering nanostructures as well as nanostructure confinement effects.

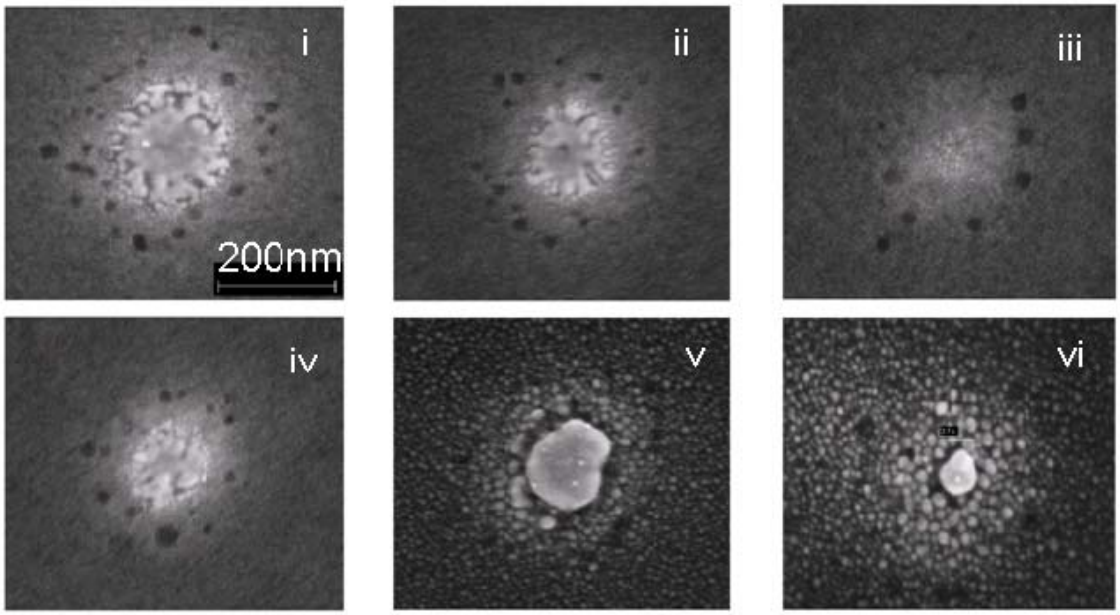

(a)

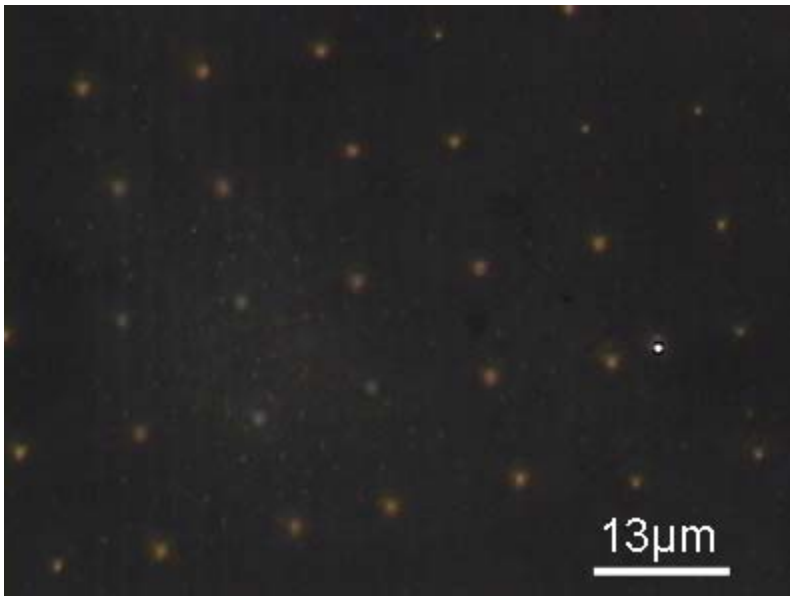

(b)

Figure 7. 11 (a) SEM imaging of sintered nanodots. **i**, **ii**, and **iii** show the sintering with incident laser intensity at 1.9e7W/m^2 for 5s, 4s, 3s respectively. **iv**. shows the sintering with 1.6e7W/m^2 for 5s. **v**. is the result of sample **i** after washing in toluene and annealed in furnace at 400^o C and **vi** is the result of **iii** after same furnace annealing. (b) The laser sintered dot array.

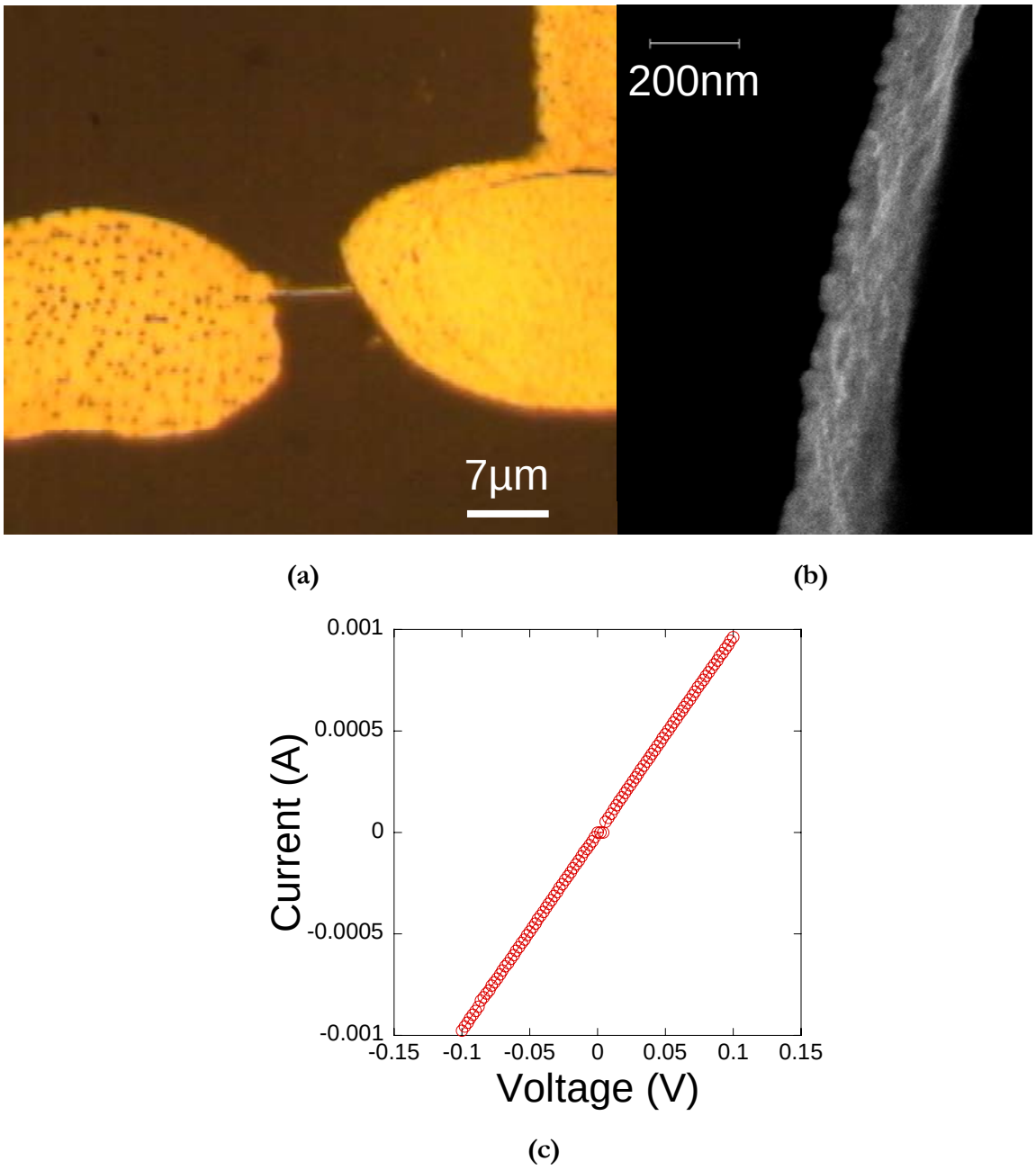

Figure 7. 12 (a) The nanowire with laser direct written contact pads. The nanowire dimension is 600nm in width, 7μm in length and 30-40nm in thickness. (b) The thickness is derived from a cross section SEM image of the sintered nanowire. (c) The I-V curve of sintered nanowire.

To better understand the nano-sintering process, thermal modeling was also conducted to predict temperature and characteristic sintering time. Thermal properties (conductivity) of thiol-capped gold nanoparticle films are required for heat transfer analysis. However, there are very few existing literature reports on thermal conductivity of such films. Consequently, we have performed molecular dynamic simulation to extract thermal conductivity of hexanethiol coated NP film using a non-equilibrium approach [Jund *et al.* (1999)]. The conductivity can be extracted from the induced temperature gradient. The MD result suggests a value of ~0.2W/mK at 300K for hexanethiol capped gold nanoparticle with gold core diameter of 2.4nm, Fig.7.13a. The assumption is made herein to neglect the electron contribution to heat transfer due to the saturated bonds within alkyl chains [Wang *et al.* (2006)]. The electron transport in the gold core and the coupling between gold and sulfur atoms are assumed to have minor effect on the effective thermal conductivity. This assumption is supported by considering that the interfacial contact resistance between gold and alkyl-thiol is ~200 MW/m^2K [Wang *et al.* (2007)], implying that the alkyl-thiol conductivity is more important [Prasher *et al.* (2003)]. Bruggman effective (BE) medium theory is chosen to compare with the prediction of effective thermal conductivity [Prasher *et al.* (2003)]. The choice of Bruggman theory is because it covers the entire range of gold fractions and could possibly lead to a complete modeling of the sintering process. In BE modeling, the nanoparticle film is modeled as an effective medium having two compositions – gold and liquid Hexane. The thermal conductivity of Hexane is ~0.124W/mK [Matheson Gas Data Book]. MD results agree reasonably well with BE and both imply low effective conductivity that is dominated by alkyl-chains (Fig. 7.13a). MD simulation predicts slightly higher conductivity. The detailed comparison and analysis are topics of separate studies and will be reported elsewhere. Briefly, complicated thermal transport is expected in the nanoscale as the mean free path and the detailed molecule orientation are neglected in the BE theory. The value of 0.25W/mK is chosen for thermal modeling in the present work to consider the actual particle size distribution. Furthermore, the desorption of thiol capping layer from gold NPs is modeled as a chemical reaction process [Garg *et al.* (2002), Shadnam *et al.* (2005)]. The temperature dependent desorption rate is described by

$$k = \frac{k_B T}{h} \exp(-\frac{\Delta G}{RT}) \tag{7-4}$$

where T is temperature, k_B is the Boltzmann constant, h is the Planck's constant, ΔG is the Gibbs free energy of activation for the desorption reaction, and R the universal gas constant. The equation $dC/dt = -k(T)C$, where C denotes the thiol concentration, is integrated over time to quantify the remaining coverage

$$\frac{C}{C_0} = \exp(-\frac{k_B T t}{h} \exp(-\frac{\Delta G}{RT})) \tag{7-5}$$

wherein t is time and C_0 is the initial concentration [Shadnam *et al.* (2005)]. The temperature is modeled as a conduction problem with laser energy as the only heat source term. The laser absorption in the nanoparticle film is simulated by DDA with the optical properties (refractive index n and k) measured from ellipsometry as input. The local absorption is evaluated by the products of polarization and electrical field (~P·E). The spatial distribution of the energy deposition is plotted in Fig.7.13c&d for two microsphere-substrate gaps. Both configurations

result in very similar total energy absorption while the configuration with substrate placed at the best focused plane (~240nm) have a smaller spreading of energy in radial direction and will be used for temperature modeling. The steady state temperature field in the multiple layer structure (containing nanoparticle film, PVP, ITO and glass) is solved by COMSOL. Considering the fast time to reach steady state vs. the thiol desorption time, the steady state temperature field is used to estimate the desorption rate. The remaining thiol coverage and temperature are plotted in radial direction at different time in Fig. 7.13b. The thiol coverage provides direct indication of the level of sintering since it is suggested that sintering starts when thiol coverage falls below 85% [Schapotschnikow *et al.* (2008)]. Modeling shows desorption takes 0.1-2s to complete and further heating does not significantly change the thiol coverage. The sintering period is observed to be up to 5s in experiment indicating that a lower temperature is obtained in experiment compared to the predicted temperature (Fig.7.13b). Recalling laser intensity employed in previously reported micro-sintering studies [Ko *et al.* (2007), Chung *et al.* (2004)], one may observe that the microsphere requires input intensity only 1.5-5 times lower to impart nano-sintering. Considering that an averaged enhancement of (microsphere diameter / focal spot diameter)^2=(3/0.6)^2 = 25 would be expected, we may attribute the reduced enhancement observed in experiment to the enhanced and more three-dimentional heat transfer loss in nanoscale sintering compared with the microscale processing.

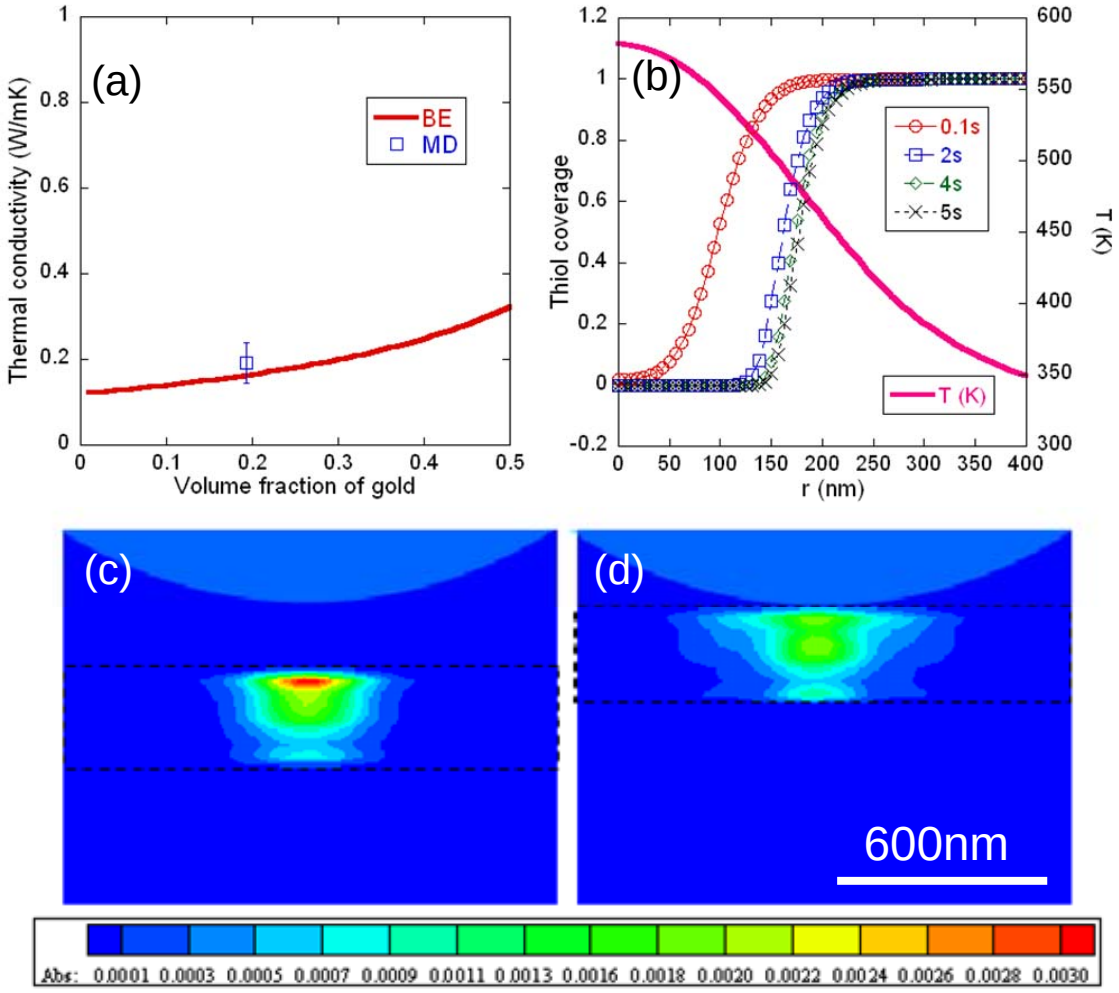

Figure 7. 13 The Thermal modeling of the nano-sintering process. (a) The comparison of thermal conductivity between MD simulation and Bruggman effective medium theory. (b) Calculated temperature distribution and thiol coverage indicating the level of sintering. (c) and (d) the laser absorption in a 300nm thick nanoparticle film with microsphere placed at 200nm above the film and 0nm above. The value of energy absorption is in the unit of *W*, to converted to volumetric energy source, the value needed to be divided by dipole volume (40nm×40nm×40nm).

7.6 Results on nanodevice fabrication.

By precisely controlling the piezo-stage movement, direct writing (sintering) of pairs of closely spaced nanowires was demonstrated. Figures 7.14a&b show nanowiress having width of ~250nm and spaced ~800nm apart. Ideally, the gap could be further reduced upon more elaborate tuning of the system. A pair of nanowires was used as electrodes for organic field effect transistors. The ITO substrate is used as the gate electrode, whereas the spin coated PVP is used as the dielectric layer (Fig.7.14c). After generating the nanowire electrodes, Au contact pads were directly written by focused micron size laser beam irradiation. The device structure is shown in Fig.7.15a, gap is bridged by a spin coated air stable semiconductor polymer [Murphy *et al.* (2005)] at 3000rpm. The air-stable semiconducting polymer is a novel material of a modified polythiophene containing electron-wthdrawing alkyl carboxylate substituents [Murphy *et al.* (2005)]. The Carboxylate-functionalized polythiophene was dissolved in warm (>45ºC) 1,2-dichlorobenzene solvent (3mg/mL) before spin coating. As comparison, a pair of contact pads without nanowire electrodes was also fabricated by focused laser writing (inset of Fig.15a). The device was annealed for 10 mins before electrical testing. Under different gate voltages, we observed a clear field effect wherein the drain-source current (I_{ds}) increased with increasing gate voltage (V_g). The field effect was most likely due to the submicron gap between nanowire electrodes. To confirm that, *I-V* measurement was performed on the laser sintered micropads without nanowires. The current is substantially lower (Fig.15b). The *I-V* curve did not shown saturation due to the short channel effects, while saturation was observed in contact pads without nanowires.

7.7 Conclusions.

To summarize, a new approach was proposed for fabricating positive and negative nanostructures with high-throughput by using near-field focusing of fluidically assembled microsphere arrays with predetermined pitch. By implementing a digital micro mirror array for the laser beam modulation, each microsphere could controlled individually resulting in pixel addressable tools. Arbitrary patterns of functional nanostructures were generated by direct nanoprocessing of solution deposited gold nanoparticles using the lens array. This method is potentially useful for fabricating extensive arrays of nanowires of other materials, e.g. semiconductors. An attractive advantage of this method is that the entire process is performed in ambient environment, involving only solution processed materials. Extension to large area processing is feasible, enabling a totally new high-yield nanomanufacturing with remarkably low cost.

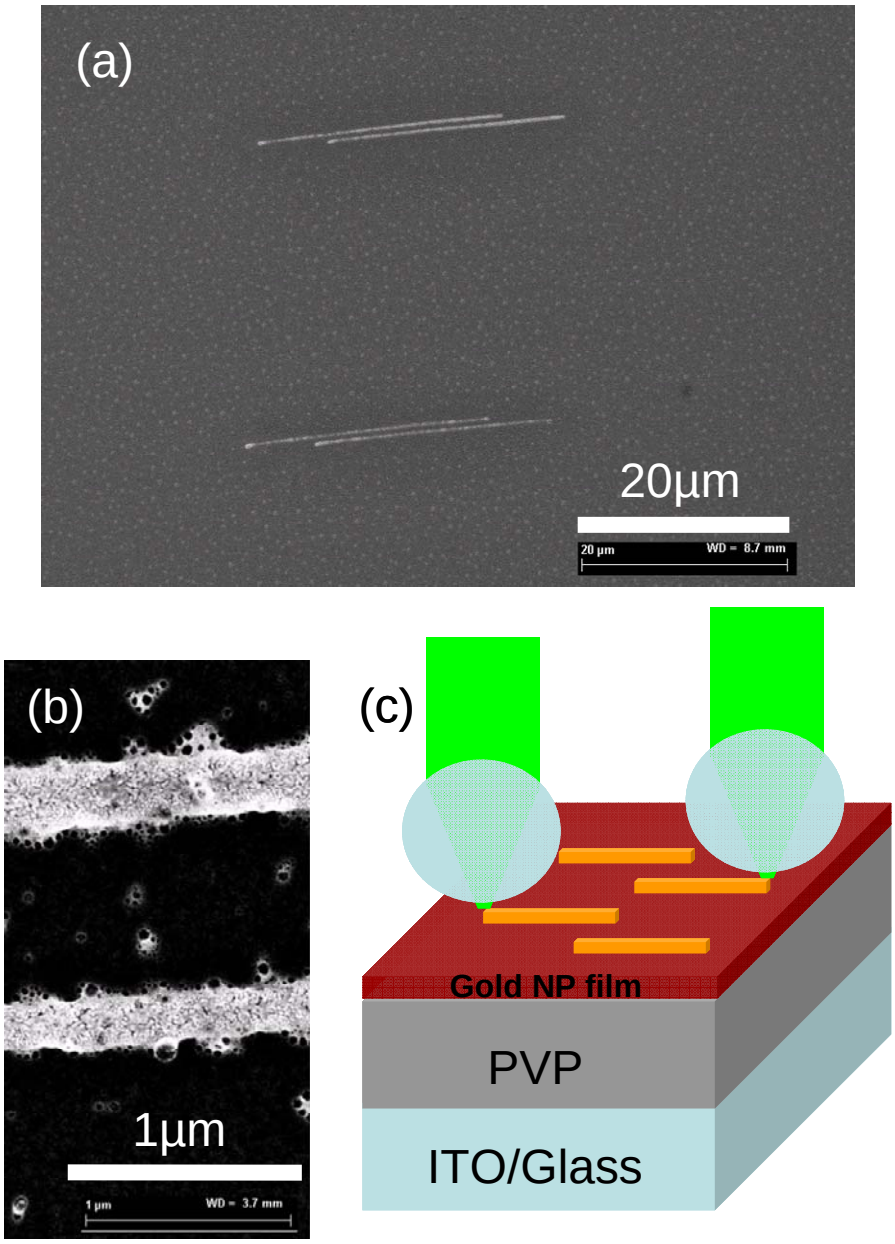

Figure 7. 14 The Nano-sintered OFET with airstable semiconducting polymer. (a)(b) Closely spaced nanowires. (c) Illustration of the device structure.

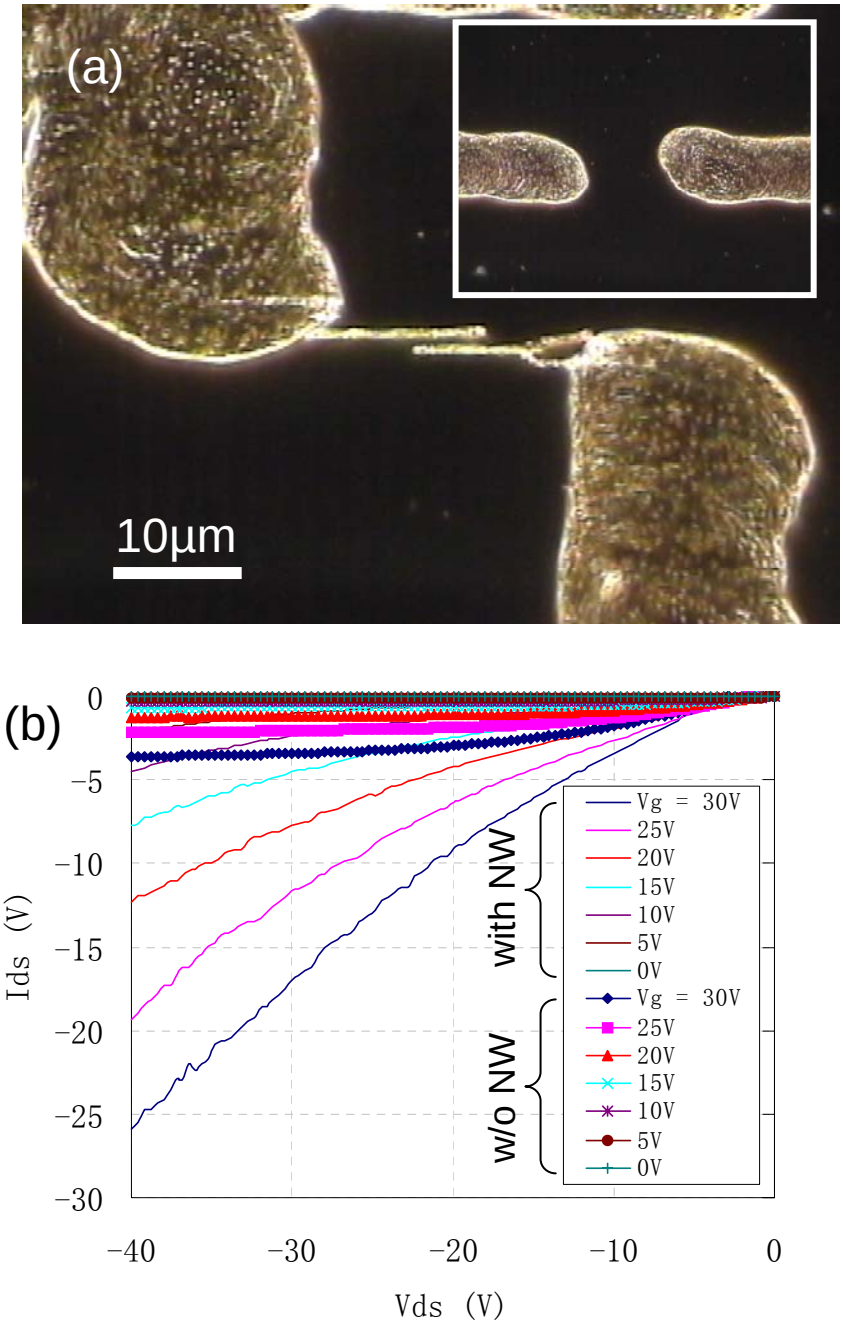

Figure 7. 15 (a) Optical dark field images nano-electrodes, the channel length in this device is ~900nm. Inset shows the device without nano-electrodes. (b) Characteristic I-V curves of the OFET with and without nanowire electrodes. The drain voltage (V_d) was scanned from 0 to –40 V and the drain current (I_d) was measured while gate voltage (V_g) was fixed at -30,-25,-20,-15,-10, 0V during each V_d scanning.

REFERENCE

A

Arcidiacono, S., Bieri, N.R., Poulikakos, D., and Grigoropoulos, C.P., 2004, "On the Coalescence of Gold Nanoparticles", Int. J. Multiphase Flow, **30**, pp. 979-994.

Atay, T., Song, J., Nurmikko, A., Nano Lett. **4**,1627 (2004**)**

A Short Course in Ellipsometry, J. A. Woollam Co., Inc

B

Bäuerle, D., Laser Processing and Chemistry (Springer, New York, 2000).

C

Chung, J., Ko, S., Bieri, N.R., Grigoropoulos, C., and Poulikakos, D., 2004, "Conductor Microstructures by Laser Curing of Printed Gold Nanoparticles Ink", Appl. Phys. Lett., **84**(5), pp. 801-803.

Combe, N., Jensen, P., and Pimpinelli, A., 2000, "Changing Shapes in the Nanoworld", Phys. Rev. Lett., **85**(1), pp. 110-113.

Chen, J. J., Zeng, F., Li, D. M., Niu, J. B., Pan, F., Thin Solid Films **485**, 257 (2005)

Carcia, R. F., McLean, R. S., Reilly, M. H., and Nunes, G., Jr., Appl. Phys. Lett., **82**, 1117 (2003)

Chiba, Y., Islam, A., Komiya, R., Koide, N., and Han, L., Appl. Phys. Lett. **88**, 223505 (2006)

Cui, Y., Lieber, C. M., *Science* **2001**, 291, 851

Chimmalgi, A., Grigoropoulos, C. P., Komvopoulos, K., J. Appl. Phys. **2005**, 97, 104319

Chou, S.Y., Krauss, P.R., Renstrom, P.J., Science ***1996****, 272 (5258), 85–87*

Chung, J., Ko, S., Bieri, N.R., Grigoropoulos, C., and Poulikakos, D., *Appl. Phys. Lett.* **2004**, *84*(5), 801-803

D

Draine, B. T., P.J.J. Flatau, Opt. Soc. Am. A **11**, 1491(1994)

Durr, M., Schmid, A., Obermaier, M., Rosselli, S., Yasuda, A., and Nelles, G., Nature Mateirals **4**, 607 (2005)

Doeswijk, L.M., Rijnders, G., Blank, D.H.A., Appl. Phys. A, **78**, 263 (**2004**)

E

Ercolessi, F., Parrinello, M., and Tosatti, E., 1998, Philos. Mag. A, **58**(1), pp. 213-226.

Exner, H., 1979, "Principles of Single Phase Sintering", Rev. Powder Metall. and Phys. Ceram. **1**, pp.7-251.

F

Frenkel, J., 1945, "Viscous Flow of Crystalline Bodies Under the Action of Surface Tension". J. Physics U.S.S.R., **4**(5), pp. 385-391.

Friendlander, S. K., and Wu, M.K., 1994, "Linear Rate Law for the Decay of the Excess Surface Area of a Coalescing Solid Particle", Phys. Rev. B, **49**(5), pp. 3622-3624.

Fann, W. S., Storz, R., Tom, H. W. K., Bokor, J., Phys. Rev. B **46**, 13592 (1992**)**

Fortunato, E. M. C., Barquinha, P. M. C., Pimentel, A. C. M. G. G., Goncalves, A. M. F., Marques, A. J. S., Martines, R. F. P., and Pereira, L. M. N., Appl. Phys. Lett., **85**, 2541 (2004)

Fortunato，E., Barquinha, P., Pimentel, A., Goncalves, A., Marques, A., Pereira, L., Martins, R., Thin Solid Films, **487**, 205 (2005)

Fan, X., Demaree, D. P., John, J. M. St., Tripathi, A., and Oliver, S. R. J., Appl. Phys. Lett. **92**, 193108 (2008)

Ferber, J. and Luther, J., Sol. Energy Mater. Sol. Cells **54**, 265 (1998)

G

Gunnarsson, L., Rindzevicius, T., Prikulis, J., Kasemo, B., Kall, M., Zou, S., Schatz, G., J. Phys. Chem. B. **109**, 1079 (**2005**)

Genov, D. A., Sarychev, A. K. and Shalaev, V. M., Physical Review E, **67**, 056611 (2003)

Gratzel, M., Nature **414**, 338 (2001)

Gregg, B.A, Chen, S., and Ferrere, S., *J. Phys. Chem. B*, **107**, 3019 (**2003**)

Garg, N., Carrasquillo-Molina, E., Lee, T.R., *Langmuir* **2002**, *18*, 2717-2726

H

Hodak, J. H., Martini, I., Hartland, G. V., J. Phys. Chem. B **102**, 6958 (1998)

Hu, M.;. Petrova, H., Hartland, G. V., Chem. Phys. Lett. **391**, 220 (2004**)**

Haynes, C., McFarland, A. D., Zhao, L., Van Duyne, R.P., Schatz, G.C., Gunnarsson, L., Prikulis, J., Kasemo, B., Kall, M., J. Phys. Chem. B **107**, 7337 (2003**)**

Hawa, T., Zachariah, M.R., Physical Review B **71**, 165434 (**2005**)

Habenicht et al., Science **309**, 2043 (2005)

Hoffman, R.L., Norris, B. J., and Wager, J. F., Appl. Phys. Lett., **82**, 733 (2003)

Hart, J. N., Menzies, D., Cheng, Y., Simon, G. P., and Spiccia, L., Sol. Energy Mater. Sol. Cells **91**, 6 (2007)

Huang, S. Y., Schlichthöl, G., Nozik, A. J., Grätzel, M., and Frank, A. J., J. Phys. Chem. B **101**, 2576 (1997)

Hwang, D. J., Chimmalgi, A. & Grigoropoulos, C. P., *J. Appl. Phys.* **2006**, 99, 044905.

Hautman, J., Klein, M., *J. Phys. Chem.* **1989**, *91* (8), 4994-5001

I

Inasawa, S., Sugiyama, M., Noda, S., Yamaguchi, Y., J. Phys. Chem. B **110**, 3114 (2006**)**

J

Johnson, D.L., 1968, "New Method of Obtaining Volume, Grain-boundary, and Surface Diffusion Coefficients from Sintering Data", J. Appl. Phys., **40**(1), pp. 192-200.

Jund, P., Jullien, R., *Physical Review B* **1999**, *59*(21), 13707-13711

K

Ko, S., Pan, H., Grigoropoulos, C., Luscombe, C., Frechet, J., and Poulikakos, D., 2007, "Air Stable High Resolution Organic Transistors by Selective Laser Sintering of Ink-jet Printed Metal Nanoparticles", Appl. Phys. Lett. **90,** 141103.

Ko, S. H., Chung, J., Pan, H., Grigoropoulos, C., and Poulikakos, D., 2007, "Fabrication

of Multiplayer Passive and Active Electric Components on Polymer Using Inkjet Printing and Low Temperature Laser Processing", Sensor and Actuators, **134** (1), pp. 161-168.

Ko, S. H., Choi, Y., Hwang, D., Grigoropoulos, C., Appl. Phys. Lett. **89**, 141126 (2006)

Ko, S.H., Pan, H., Grigoropoulos, C. P., Luscombe, C.K., Fréchet, J.M.J., Poulikakos, D., Nanotechnology, **18**,345202 (2007)

Ko, S.H., I. Park, H. Pan, C.P. Grigoropoulos, A.P. Pisano, C.K. Luscombe, and J.M.J. Fréchet, Nanoletters, **7**(7), 1869 (2007)

Kim, S.J., and Jang, D., 2005, "Laser-induced Nanowelding of Gold Nanoparticles", Appl. Phys. Lett., **86**, 033112.

Kuczinski, G.C., 1949, "Self-diffusion in Sintering of Metallic Particles", Trans. Amer. Inst. Min. (Metall.) Engr., **185**, pp. 169-178.

Koch, W., and Friedlander, S.K., 1990, "The Effect of Particle Coalescence of the Surface Area of a Coagulating Aerosol". J. Colloid and Interface Science, **140**(2), pp. 419-427.

Kado, T., Yamaguchi, M., Yamada, Y., and Hayase, S., Chemistry Letters **32**, 1056 (2003)

Kim, H., Auyeung, R.C.Y, Ollinger, M., Kushto, G.P., Kafafi, Z.H., Pique, A., Appl. Phys. A **83**, 73 (2006)

Kim, H., Kushto, G.P., Arnold, C.B., Kafafi, Z.H., Pique, A., Appl. Phys. Lett. **85**, 464 (2004)

Kraus, T., Malaquin, L., Schmid, H., Riess, W., Spencer, N. D., Wolf, H., Nature Nanotechnology **2007**, 2, 570-576

L

Lehtinen, K. E., and Zachariah, M., 2002, "Energy Accumulation in Nanoparticle Collision and Coalescence Processes", Aerosol Science, **33**, pp. 357-368

Link, S., Burda, C., Nikoobakht, B., El-Sayed, M. A., Chemical Physics Letters **315**, 12 (1999**)**

Law, M., Greene1, L. E., Johnson, J. C., Saykally, R. and Yang, P., Nature Maters. **4**, 455 (2005)

Lindstrom, H., Holmberg, A., Magnusson, E., Lindquist, S., Malmqvist, L., and. Hagfeldt, A., Nano Lett. **1**, 97 (2001)

Lindstrom, H., Holmberg, A.,Magnusson, E.,Malmquist, L. Hagfeldt, A. J. Photochem. Photobiol. A **145**, 107 (2001)

Lee, C. J., Lee, T. J., Lyu, S. C., Zhang, Y. Ruh, H., Lee, H. J., *Appl. Phys. Lett.* **2002**, *81*, 3468.

Li, M., Bhiladvala, R. B., Morrow T. J., Sioss, J. A., Lew, K., Redwing, J.M., Keating, C. D., Mayer, T.S., Nature Nanotechnology **2008**, 3, 88-92

Luedtke, W.D., Landman, U., *J. Phys. Chem.* **1996**, *100* (32), 13324-13329

M

Murr, L.E., 1975, "Interfacial Phenomena in Metals and Alloys", Addison-Wesley Publishing Company, Inc.

Medasani, B., Park, Y. H., and Vasiliev, I., 2007, "Theoretical Study of The Surface Energy, Stress, and Lattice Contributing of Silver Nanoparticles", Phys. Rev. B, **75,** 235436.

McMahon, M. D., Lopez, R., Haglund, R. F., Ray, E. A., Bunton, P. H., Physical Review B **73**, 041401 (2006)

Minami, T., Semicond. Sci. Technol. **20**, S35 (2005)

Misra，N., Xu, L., Pan, Y., Cheung, N., and Grigoropoulos, C. P., Appl. Phys. Lett. **90**, 11111 (2007)

Murakami, T. N., Kijitori, Y., Kawashima, N., and Miyasaka, T., Chemistry Letter **32**, 1076 (2003)

McLeod, E., Arnold, C., *Nature Nanotechnology,* **2008**, 3, 413-417

Murphy, A. R.; Liu, J.; Luscombe, C.; Kavulak, D.; Frechet, J. M. J.; Kline, R. J.; McGehee, M. D. *Chem. Mater.* **2005**, *17*, 4892-4899.

Matheson Gas Data Book, McGraw-Hill Professional; 7 edition (June 25, 2001)

N

Nichols, F.A., and Mullins, W.W., 1965, "Morphological Changes of a Surface of Revolution due to Capillarity-induced Surface Diffusion", J. Appl. Phys., **36**(6), pp. 1826-1835

Nishii, J., et al., Jpn. J. Appl. Phys., **42**, L347 (2003)

Norris，B. J., Anderson, J., Wager, J. F., and Keszler, D. A., J. Phys. D: Appl. Phys., **36**, L105 (2003)

Nakade, S., Matsuda, M., Kambe, S., Saito, Y., Kitamura, T., Sakata, T., Wada, Y., Mori, H.and Yanagida, S., J. Phys. Chem. B **106**, 10004 (2002)

O

Otter, M., Z. Phys. **161**, 539 (1961**)**

Ohya, Y., Niwa, T., Ban, T., and Takahashi, Y., Jpn. J. Appl. Phys., **40**, 297 (2001)

Ozerov，I., Arab, M., Safarov, V.I., Marine, W., Giorgio, S., Sentis, M., L. Nanai, Appl. Surf. Sci., **226**, 242 (2004)

Ozerov, I., Nelson, D., Bulgakov, A.V., Marine, W., Sentis, M., Appl. Surf. Sci., **212**, 349 (2003)

Oates, T. W. H. and Mucklich, A., Nanotechnology, **16**, 2606(2005)

Oates, T. W. H., McKenzie, D. R., and Bilek, M. M. M., Physical Review B, **70**, 195406 (2004)

O'Regan, B., Gratzel, M., Nature **353**, 737 (1991)

Okuya, M., Nakade, K., Osa, D., Nakano, T., Kumara, G.R.A., and Kaneko, S., J. Photochemistry and Photobiology A: Chemistry, **164**, 167 (2004)

P

Pan, J., 2004, "Solid-state Diffusion Under a Large Driving Force and the Sintering of Nanosized Particles", Philos. Mag. Lett., **84**(5), pp. 303-310.

Pan, H., Ko, S. H., Grigoropoulos, C.P., Miller, N., Haller, E. E., and Dubon, O., Appl. Phys. A **94**, 111 (2009)

Plech, A., Kotaidis, V., Lorenc, M., Wulff, M., Chem. Phys. Lett. **401** 565 (2005)

Plech, A., Kotaidis, V., Gresillon, S., Dahmen, C., Plessen, G., Physical Reivew B, 70, 195423 (2004)

Pan, H., Ko, S. H., Grigoropoulos, C.P., Appl. Phys. A, **90**, 247 (2008)

Pan, H.; Ko, S. H., Grigoropoulos, C. P., *Appl. Phys. Lett.* **2008**, *93*, 234104

Pichot, F., Roland Pitts, J., and Gregg, B. A., Langmuir **16**, 5626 (2000)

Park, N. G., Lagemaat, J. van de, and Frank, A. J., J. Phys. Chem. B **104**, 8989 (2000)

Park, S., Lee, D. H., Xu, J., Kim, B., Hong, S. W., Jeong, U., Xu, T., Russel, T. P., *Science* **2009**, 323, 1030-1033

Park, J., Hardy, M., Kang, S. J., Barton, K., Adair K., Mukhopadhyay, D. K., Lee, C. Y., Strano, M. S., Alleyne, A. G. Georgiadis, J.G., Ferreira, P. M., Rogers, J.A., Nature Materials **2007**, 6, 782-789

Piner, R.D, Zhu, J., Xu, F., Hong, S., Mirkin, C., Science **1999**, 283 (5402), 661-663

Pauzauskie, P. J., Radenovic, A., Trepagnier, E., Shroff, H., Yang, P., Liphardt, J., Nature Materials **2006**, 5, 97-101

Prasher, R.S., Shipley, J., Prstic, S., Koning, P., Wang, J-L., *Journal of Heat Transfer* **2003**, *125*(6), 1170–1177

Q

R

S

Steinhardt, P. J., Nelson, D. R., and Ronchetti, M., 1993, "Bond-orientational Order in Liquids and Glasses", Phys. Rev. B, **28**(2), pp. 784-805.

Saitoh, K., Kitagawa, H., 1999, "Molecular Dynamics Study of Surface Effects on Atomic Migration near Aluminum Grain Boundary", Comp. Mater. Sci. **14**, pp. 13-18.

Schiotz, J., Tolla, F.D.D., and Jacobsen, K.W., 1998, "Softening of Nanocrystalline Metals at Very Small Grain Sizes", Nature, **391**(5), pp. 561-563.

Su, K. H., Wei, Q., Zhang, X., Mock, J., Smith, D., Schultz, S., Nano Letters **3**, 1087 (2003)

Stietz, F., Appl. Phys. A **72**, 381 (2001)

Sun, X. W., Yu, S. F., Xu, C. X., Yuen, C., Chen, B. J., Li, S., Jpn. J. Appl. Phys., Part 2 **42**, L1229 (2003)

Smith, P.M., Carey, P.G., and Sigmon, T.W., Appl. Phys. Lett. **70**, 342 (1997)

Smith, G. B., Maaroof, A. I., Allan, R. S., Schelm, S., Anstis, G. R. and Cortie, M. B., Proc. Of SPIE, **5508**, 192 (2004)

Sivaramakrishnan, S., Chia, P., Yeo, Y., Chua, L. and Ho, P. K. H., Nature Materials, **7**, 149 (2007)

Seal, K., Nelson, M. A., Ying, Z. C., Genov, D. A, Sarychev, A. K. and Shalaev, V. M., Physical Review B, **67**, 035318 (2003)

Stathatos, E. and Lianos, P., Adv. Mater. Weinheim, Ger. **19**, 3338 (2007)

Sun, S., Montague, M., Critchley, K., Chen, M., Dressick, W. J., Evans, S.D., Leggett, G.J., *Nano Letter* **2006**, *6(1)*,29-33

Srituravanich, W., Pan, L., Wang, Y., Sun, C., Bogy, D. B., Zhang, X., *Nature Nanotechnology,* **2008**, 3, 733-737

Schapotschnikow, P., Pool, R., Vlugt, T.J.H., *Nano Letter* **2008**, *8*(9), 2930-2934

Shadnam, M. R., Amirfazli, A., *Chem. Commun*. **2005**, 4869-4871

T

Thompson, S.M., Gubbins, K.E., Walton, J.P.R.B, Chantry, R.A.R., and Rowlinson, J.S., 1984, "A Molecular Dynamics Study of Liquid Drops". J. Chem. Phys., **81**(1), pp. 530-542.

Tseng, R.J., Huang, J., Ouyang, J., Kaner, R. B., and Yang, Y., *Nano Letter* **2005**, *5(6)*,1077-1080

U

V

Volkman, S. K., Mattis, B. A., Molesa, S. E., Lee, J. B., A. de la Fuente V., T. Bakhishev, and V. Subramanian, IEEE International Electron Device meeting Technical Digest, 769 (2004)

Vanheusden, K., Warren, W.L., Seager, C.H., Tallant, D.R., Voigt, J.A., Gnade, B.E., J. Appl. Phys., **79**, 7983 (1996)

Vries, A. J., Kooij, E. S., Wormeester, H., Mewe, A. A. and Poelsema, B., J. of Appl.Phys., **101**, 053703 (2007)

W

Wang, Y., and Dellago, C., 2003, J. Phys. Chem. B, **107**, pp. 9214-9219.

Washington, P.L., Ong, H.C., Dai, J. Y., and Chang, R. P. H., Appl. Phys. Lett. **72**, 3261 (1998)

Weidmann, J., Dittrich, Th., Konstantinova, E., Lauermann, I., Uhlendorf, I., Koch, F., Solar Energy Materials and Solar Cells, **56,** pp.153 (1999)

Wang, R., Segalman, R.A., Majumdar, A., *Appl. Phys. Lett.* **2006**, *89*, 173113

Wang, Z., Carter, J.A., Lagutchev, A., Koh, Y.K., Seong, N., Cahill, D.G., Dlott, D.D., *Science* **2007**, *317*, 787

X

Xing, Y., and Rosner, D., 1999, "Prediction of Spherule Size in Gas Phase Nanoparticle Synthesis", J. Nanoparticle Research, **1**, pp. 277-291.

Y

Yu, X., and Duxbury, P.M., 1995, "Kinetics of Nonequilibrium Shape Change in Gold Clusters", Phys. Rev. B, **52**(3), pp. 2102-2106.

Z

Zhu, H., and Averback, R.S., 1996, "Sintering Processes of Two Nanoparticles: a Study of Molecular-Dynamics Simulations", Philoso. Mag. Lett., **73**(1), pp. 27-33.

Zeng, P., Zajac, S., Clapp, P.C., and Rifkin, J.A., 1998, "Nanoparticle Sintering Simulation", Materials Science and Engineering, A252, pp. 301-306.

Zhang, W., Gladwell, I., 1998,Comp. Mater. Sci., **12**, pp. 84-104.

Zachariah, M., and Carrier, M., 1999, J. Aerosol Sci. **30**(9), pp. 1139-1151.

Zhao, L., Kelly, K.L., Schatz, G. C., J. Phys. Chem. B **107**, 7343 (2003**)**

Zhang, X. and Stroud, D., Physical Review B, **52**(3), 2131 (1995)

Zhang, D, Yoshida, T. and Minoura, H., Adv. Mater. **15**, 814 (2003)

Zhigilei, L.V., Kodali, P.B.S., Garrison, B.J., *J. Phys. Chem. B* **1997**, *101*, 2028-2037.

Zhao, X., Leng, Y., Cummings, P.T., *Langmuir* **2006**, *22*, 4116-4124